

# Demonstration and Characterization of Ladder-Type Conjugated Polymer Photoanode for Direct Light-Driven Water Oxidation

THÈSE N° 7975 (2017)

PRÉSENTÉE LE 27 OCTOBRE 2017

À LA FACULTÉ DES SCIENCES DE BASE

LABORATOIRE D'INGÉNIERIE MOLÉCULAIRE DES NANOMATÉRIAUX OPTOÉLECTRONIQUES

PROGRAMME DOCTORAL EN CHIMIE ET GÉNIE CHIMIQUE

ÉCOLE POLYTECHNIQUE FÉDÉRALE DE LAUSANNE

POUR L'OBTENTION DU GRADE DE DOCTEUR ÈS SCIENCES

PAR

Pauline BORNOZ

acceptée sur proposition du jury:

Prof. S. Gerber, présidente du jury

Prof. K. Sivula, directeur de thèse

Prof. V. Artero, rapporteur

Prof. J. Strunk, rapporteuse

Prof. S. Haussener, rapporteuse



ÉCOLE POLYTECHNIQUE  
FÉDÉRALE DE LAUSANNE

Suisse  
2017



# Acknowledgements

I used to think that a PhD is a unique occasion to conduct a four years full project on your own. Throughout these years I realized that it can only be successful and enjoyable if you are surrounded by the right people and for that I express my gratitude to a few people.

I would like first to thank Prof. Kevin Sivula for offering me this unique opportunity to work under his supervision. Thank you for your support and for building this nice dynamic and friendly laboratory. I appreciated the autonomy and liberty you have given us and your door always open to provide your help.

Thank you to the jury members: Prof. Vincent Artero, Prof. Jennifer Strunk, Prof. Sophia Haussener and Prof. Sandrine Gerber for their time and evaluation of my work.

I would like to thank Prof. Christos Comninellis for his mentorship before and during this work. You taught me to always think outside the box and to look for actual meaning of things. To see your passion for your work and for the transmission of knowledge was a real motivation for me.

I would like to do a general acknowledgments to all the LIMNO team. To all the post docs: Dr. Sébastien Bivaud, Dr. Emilie Ripaud, Dr. Néstor Guijarro Carratalá, Dr. Florian Le Formal, Dr. Liang Yao, Dr. Melissa Johnson, Dr. Jun-Ho Yum, Dr. Florent Boudoire and Dr. Charles Lhermitte and to all the PhD students: Andrea Gasperini, Xiaoyun Yu, Mathieu Prévot, Xavier Jeanbourquin, Aiman Rahmanudin, Wiktor Bourée, Yongpeng Liu, Arvinhd Sekar, Xiaodi Zhu and Xavier Pereira Da Costa. It has been a great pleasure to be part of this group by your side and to profit from your varied scientific and technical knowledge as well as to share multiple life experiences; from barbecue, parties on the roof, laser games to watching tennis and other sports... Special thanks to Andrea and Mathieu for the building of the friendly and mutual aid spirit of the laboratory and Néstor for guidance and support in and outside the laboratory.

Thanks also to all people in the shadows who make everything work: our secretaries: Nadia Macor, Sophie Oblette and Irina Lopez, the chemical shop with Jacky and Marie, everybody in the mechanical and electronic shop. Thanks to LPI laboratory, Christophe Roussel and Stéphane Thonney for letting me use their equipment and thanks to Kevin, Mathieu and Nadia for proof-reading the manuscript.

## Acknowledgements

---

Finally I think that these four years were a real pleasure only because of a good work-life balance. Merci à ma famille, sans vous j'aurais abandonné les études il y a bien longtemps. Merci à Grand-Papa pour ta motivation et pensées à Grand-Maman qui aurait voulu être là. Merci à Eric et Christine pour tout ce qu'ils m'ont apporté pendant mon séjour à Paris et après. Merci à Nadia qui m'a supportée pendant ces longues années. Crois-moi, tu m'as largement rendu ce que j'ai fait pour toi pendant ton doctorat. Enfin merci à mes amis pour leur soutien, Aline, Helena, Flavien et au groupe de claquettes.

*Lausanne, July 2017*

P. B.



# Contents

<b>Acknowledgements</b>	<b>iii</b>
<b>List of figures</b>	<b>ix</b>
<b>List of tables</b>	<b>xi</b>
<b>List of Symbols</b>	<b>xv</b>
<b>I Introduction</b>	<b>1</b>
<b>1 Motivations and Background</b>	<b>3</b>
1.1 Photovoltaic (PV) Technology . . . . .	6
1.2 Solar-to-Hydrogen (STH) Technology . . . . .	9
1.3 Photoelectrochemical (PEC) Technology . . . . .	11
1.3.1 Challenges for Photoelectrochemical (PEC) Technology . . . . .	14
1.3.2 Organic Semiconductors . . . . .	14
1.4 Summary . . . . .	16
References . . . . .	16
<b>II Experimental</b>	<b>21</b>
<b>2 Optical and Physical Characterization</b>	<b>23</b>
2.1 Absorption of Light . . . . .	24
2.2 Film Morphology . . . . .	26
2.3 Raman Spectroscopy . . . . .	27
2.4 Contact Angle . . . . .	27
2.5 Gas Chromatography . . . . .	28
2.6 Photoluminescence Spectroscopy . . . . .	28
2.7 Experimental instruments . . . . .	28
2.7.1 Materials . . . . .	28
2.7.2 Instruments . . . . .	29
2.7.3 Calibration of Solar Simulator . . . . .	30
References . . . . .	31

## Contents

---

<b>3</b>	<b>Electrochemical Characterization</b>	<b>33</b>
3.1	Electrochemical Reactions . . . . .	34
3.2	Potentiostatic Methods . . . . .	37
3.3	Frequency Based method . . . . .	40
3.4	Quartz Crystal Microbalance (QCM) . . . . .	44
3.5	Incident Photon-to-current Efficiency (IPCE) . . . . .	45
3.6	Experimental instruments . . . . .	45
3.6.1	Materials . . . . .	45
3.6.2	Instruments . . . . .	47
	References . . . . .	48
<b>III</b>	<b>Results</b>	<b>49</b>
<b>4</b>	<b>Tandem Cell for Overall Solar Water Splitting</b>	<b>51</b>
4.1	Motivation . . . . .	52
4.2	Energetic and Optical Characterization . . . . .	52
4.3	Separate Current density-Voltage (J-V) Characterization . . . . .	56
4.4	Tandem Cell Characterization . . . . .	59
4.5	Conclusions . . . . .	62
	References . . . . .	62
<b>5</b>	<b>BBL Thin Films Preparation</b>	<b>67</b>
5.1	Poly(benzimidazobenzophenanthroline) (BBL) Ladder Polymer . . . . .	68
5.2	Photoelectrode Fabrication . . . . .	69
5.2.1	Dip Coating Procedure . . . . .	70
5.2.2	Spray Coating Procedure . . . . .	71
5.2.3	Overlayers Deposition . . . . .	74
5.3	Optical Characterization . . . . .	74
5.4	Conclusions . . . . .	77
	References . . . . .	77
<b>6</b>	<b>Water Oxidation by a BBL Photoanode</b>	<b>79</b>
6.1	Morphology . . . . .	80
6.2	Linear Sweep Voltammetry (LSV) in Sacrificial Electrolyte . . . . .	80
6.3	Mott-Schottky (M-S) Analysis . . . . .	82
6.4	Linear Sweep Voltammetry (LSV) in Non-Sacrificial Electrolyte . . . . .	83
6.5	Determination of the Photooxidation Reaction . . . . .	84
6.6	Oxygen Production . . . . .	88
6.7	Conclusion . . . . .	89
6.8	Additional figures . . . . .	90
	References . . . . .	92

<b>7</b>	<b>Characterization of Charge Transport Processes in BBL Photoanodes</b>	<b>95</b>
7.1	Motivation . . . . .	96
7.2	Cyclic Voltammetry (CV) . . . . .	96
7.3	Electrochemical Quartz Crystal Microbalance (EQCM) . . . . .	98
7.4	Electrochemical Impedance Spectroscopy (EIS) . . . . .	102
7.5	Conductivity . . . . .	107
7.6	Linear Sweep Voltammetry (LSV) . . . . .	108
7.7	Conclusions . . . . .	109
7.8	Additional Figures . . . . .	110
	References . . . . .	112
<b>IV</b>	<b>Conclusions</b>	<b>115</b>
<b>8</b>	<b>Final Comment and Outlook</b>	<b>117</b>
	<b>Acronyms</b>	<b>121</b>
	<b>Curriculum Vitae</b>	<b>123</b>



# List of Figures

1.1	Swiss energy production in 2014 . . . . .	4
1.2	Swiss energy consumption in 2014 . . . . .	4
1.3	Swiss electricity production by photovoltaic panels per year . . . . .	5
1.4	Swiss and world energy consumption per year . . . . .	5
1.5	Semiconductor energetics at 0 K . . . . .	7
1.6	Formation of a n-p junction by contacting an n-type and a p-type semiconductor . . . . .	8
1.7	Representation of the SCLJ for an n-type and p-type semiconductors . . . . .	11
1.8	The PV-electrolyser, S2 and D4 PEC configuration . . . . .	13
2.1	AM1.5G spectrum. . . . .	24
2.2	Schematic description of light-mater interaction. . . . .	25
2.3	Contact angle between a solid and water . . . . .	27
2.4	AM 1.5 spectrum and Xenon arc lamp spectrum . . . . .	30
2.5	IPCE and current density of diode with calibrated lamp spectrum . . . . .	31
3.1	Schematic representation of an electrochemical cell . . . . .	34
3.2	Schematic representation of a two and a three-electrodes cell configuration . . . . .	35
3.3	n-type semiconductor at equilibrium . . . . .	37
3.4	n-type semiconductor under flat-band condition . . . . .	38
3.5	n-type semiconductor under negative bias . . . . .	38
3.6	n-type semiconductor under positive bias . . . . .	38
3.7	Chronoamperometry (CA) experiment . . . . .	39
3.8	Linear Sweep Voltammetry (LSV) experiment . . . . .	40
3.9	Cyclic Voltammetry (CV) experiment . . . . .	40
3.10	Phasor diagram of potential and current waves during an EIS measurement . . . . .	41
3.11	Example of an equivalent circuit and its corresponding EIS results . . . . .	43
3.12	Schematic description of QCM technique . . . . .	44
4.1	Simplified electron energy diagram of a BiVO <sub>4</sub> -Cu <sub>2</sub> O tandem cell . . . . .	53
4.2	Absorbance, transmittance and Tauc plot of spray-deposited BiVO <sub>4</sub> . . . . .	54
4.3	IPCE of Cu <sub>2</sub> O photocathode at 0 V <sub>RHE</sub> and the standard AM1.5G photon flux . . . . .	55
4.4	J-V curves for BiVO <sub>4</sub> with and without Co-Pi and for Cu <sub>2</sub> O in the tandem cell . . . . .	57
4.5	Tandem cell transient J-t curve with and without Co-Pi under illumination . . . . .	60
4.6	J-V curve of the BiVO <sub>4</sub> with, without Co-Pi and after the stability measurement . . . . .	61

## List of Figures

---

5.1	Synthesis of Poly(benzimidazobenzophenanthroline) (BBL) polymer . . . . .	68
5.2	Thermal stability of BBL . . . . .	68
5.3	Summary of different methods to prepare thin film of BBL . . . . .	70
5.4	Schematic description of the dip coating procedure . . . . .	71
5.5	Schematic description of the dispersion preparation . . . . .	71
5.6	Morphology of the wet-spun BBL fiber and BBL dispersion . . . . .	72
5.7	Schematic description of the spray deposition procedure . . . . .	72
5.8	MALDI-TOF MS analysis of a control solution of Igepal® in nitric acid . . . . .	73
5.9	MALDI-TOF MS analysis of washing solution . . . . .	73
5.10	Calibration of the film thickness as a function of amount of dispersion sprayed . . . . .	74
5.11	Absorptance of BBL films as a function of amount of dispersion sprayed . . . . .	75
5.12	Absorption coefficient of BBL films as a function of amount of dispersion sprayed . . . . .	75
5.13	Tauc plot for a sprayed BBL film with 10 $\mu\text{L}$ dispersion . . . . .	76
5.14	Theoretical photocurrent density of BBL film as a function of thickness . . . . .	76
6.1	SEM and optical top view of a dip-coated and a sprayed films . . . . .	80
6.2	J-V curve of a thin sprayed film and a dip-coated film sacrificial electrolyte . . . . .	81
6.3	Comparison of back side and front side illumination photocurrent . . . . .	82
6.4	Mott-Schottky plot and energy band diagram of a BBL photoanode . . . . .	82
6.5	J-V curve of a spray coated BBL film in non-sacrificial electrolyte . . . . .	83
6.6	BBL $J_{\text{ph}}$ stability at 1.23 $V_{\text{RHE}}$ . . . . .	84
6.7	IPCE of a spray coated BBL film . . . . .	85
6.8	Fluorescence probe reaction used to detect hydroxyl radicals . . . . .	86
6.9	CV of a spray coated BBL film in aqueous electrolyte containing 4 mM of coumarin . . . . .	86
6.10	Fluorescence spectra of non-sacrificial electrolyte containing 0.1 mM coumarin . . . . .	87
6.11	Average contact angle of a water drop on a bare BBL film and coated with $\text{TiO}_2$ . . . . .	88
6.12	J-V curves of a BBL film before, after $\text{TiO}_2$ deposition, and with Ni-Co catalyst . . . . .	89
6.13	Absorptance spectra of a dip coated and spray-coated film with similar thickness . . . . .	90
6.14	Nyquist plots of a spray-coated BBL electrode . . . . .	90
6.15	$J_{\text{ph}}$ transient measurements of the spray coated BBL electrode . . . . .	91
6.16	Raman spectra of a bare BBL spray coated film before and after PEC testing . . . . .	91
6.17	Calibration of umbelliferone fluorescence as a function of its concentration . . . . .	92
7.1	CV of a BBL spray coated photoanode in 1 M $\text{NaClO}_4$ and 1 M $\text{Na}_2\text{SO}_4$ /buffer . . . . .	97
7.2	Pourbaix diagram representing BBL reactions and measured half-wave potential . . . . .	97
7.3	EQCM data of BBL spray coated photoanode in $\text{NaClO}_4$ 0.1 M pH 7.4 . . . . .	99
7.4	EQCM data of BBL spray coated photoanode in NaTPB and TBACl . . . . .	100
7.5	EQCM data of BBL spray coated photoanode in $\text{HClO}_4$ 0.1 M pH 0 . . . . .	100
7.6	Results of QCM data representing BBL film swelling with electrolyte . . . . .	101
7.7	Equivalent circuits used to fit data . . . . .	102
7.8	Results from the fitting of EIS data in $\text{NaClO}_4$ 1 M pH 7.4. Thickness comparison . . . . .	103
7.9	Results from the fitting of EIS data in $\text{NaClO}_4$ 1 M pH 7.4. pH comparison . . . . .	105
7.10	Results from the fitting of EIS data in 0.5 M $\text{Na}_2\text{SO}_4$ /buffer. pH comparison . . . . .	106

7.11 Results from the fitting of EIS data in $\text{NaClO}_4$ 1 M pH 7.4. Illumination comparison	107
7.12 Conductivity of a BBL spray coated photoanode in $\text{NaClO}_4$ and $\text{NaSO}_4$ /buffer	108
7.13 LSV of a BBL spray coated photoanode in 1 M $\text{NaClO}_4$ and 1 M $\text{NaSO}_4$ /buffer .	109
7.14 CV of a BBL spray coated photoanode in 1 M $\text{Na}_2\text{SO}_4$ . . . . .	110
7.15 EQCM data of BBL spray coated photoanode in $\text{NaClO}_4$ 1 M pH 7.4 and pH 2.9	110
7.16 EQCM data of BBL spray coated photoanode in $\text{NaClO}_4$ 0.1 M in acetonitrile .	111
7.17 Bode plot of EIS data of a spray coated BBL photoanode in $\text{NaClO}_4$ 1 M pH 7.4	111
7.18 CV for the determination of surface contact area . . . . .	112





## List of Tables

C.1	Electrolyte used for typical PEC measurement . . . . .	46
C.2	Electrolyte used for cobalt catalyst deposition . . . . .	46
C.3	Electrolyte used for EQCM and EIS analysis . . . . .	46
G.1	Results of the linear regression for the determination of S/d ratio . . . . .	112



# List of Symbols

A	Absorbance, in a.u.
$A_{\%}$	Absorptance, in %
$\alpha$	absorption coefficient, in $\text{cm}^{-1}$
$a_{\text{H}_2\text{O}}$	Activity of water
c	Speed of light in vacuum: $3 \times 10^8 \text{ m} \cdot \text{s}^{-1}$
C	Capacitance, in F
$C_{\text{SC}}$	Space charge capacitance, in F
e	Elementary charge: $1.6 \times 10^{-19} \text{ C}$
E	Potential, in V
E	Amplitude of potential, in V
$E_{\text{CB}}$	Conduction band energy, in eV or V
$E_{\text{F}}$	Fermi level, in eV or V
$E_{\text{fb}}$	Flat-band potential, in V
$E_{\text{F,redox}}$	Fermi level in the electrolyte, in eV or V
$E_{\text{F,p}}$	Quasi Fermi level of holes, in V
$E_{\text{F,n}}$	Quasi Fermi level of electrons, in V
$E_{\text{g}}$	Band gap energy, in eV or V
$E_{\text{G}}$	Potential drop in the Gouy layer, in V
$E_{\text{g}}^{\text{opt}}$	Optical band gap, in eV
$E_{\text{H}}$	Potential drop in the Helmholtz layer, in V
$E_{\text{NHE}}$	Potential reported versus the NHE electrode, in V
$E_{\text{OER}}^0$	Potential for oxygen evolution reaction, in V
$E_{\text{ref}}$	Potential reported versus a reference electrode, in V
$E_{\text{RHE}}$	Potential reported versus the RHE electrode, in V
$E_{\text{SC}}$	Potential drop in the space charge layer, in V
$\epsilon_0$	Vacuum permittivity: $8.85 \times 10^{-12} \text{ A} \cdot \text{s} \cdot \text{V}^{-1} \text{ m}^{-1}$
$\epsilon_r$	Dielectric constant of a material
$E_{\text{th}}$	Potential for isothermal reaction, in V
$E_{\text{tot}}$	Total potential, in V
$ E_{\text{vac}} $	Absolute value of energy reported versus the vacuum energy, in eV

## List of Symbols

---

$E_{VB}$	Valance band energy, in eV or V
$\eta_{cell}$	Overpotential from the cell, in V
$\eta_{ox}$	Overpotential for OER, in V
$\eta_{red}$	Overpotential for HER, in V
$F$	Faradaic constant: $96500 \text{ C} \cdot \text{mol}^{-1}$
$f_0$	Resonant frequency: 4.95 Hz for At-cut quartz
$\Delta f$	Frequency change, in Hz
$\Delta G^0(T)$	Standard free Gibbs energy, in $\text{kJ} \cdot \text{mol}^{-1}$
$\gamma_{GL}$	Gas-solid interfacial energy, in $\text{N} \cdot \text{m}^{-1}$
$\gamma_{LS}$	Liquid-solid interfacial energy, in $\text{N} \cdot \text{m}^{-1}$
$\gamma_{SG}$	Solid-gas interfacial energy, in $\text{N} \cdot \text{m}^{-1}$
$h$	Plank constant: $6.63 \times 10^{-34} \text{ J} \cdot \text{s}$
$h\nu$	Photon energy, in eV
$I$	Current, in A
$ I $	Amplitude of current, in A
$I_0$	Incident light, in %
$I_0(\lambda)$	Incident light flux, in $\text{W} \cdot \text{m}^{-2}$
$I_A$	Absorbed light, in %
$I_{Rd}$	Diffuse reflection, in %
$I_{RS}$	Specular reflection, in %
$I_S$	Refracted light, in %
$I_T$	Transmitted light, in %
$IPCE(\lambda)$	number of electrons extracted per photon of $\lambda$
$J$	Current density, in $\text{A} \cdot \text{cm}^{-2}$
$J_{BBL \text{ th}}$	BBL theoretical photocurrent density, in $\text{A} \cdot \text{m}^{-2}$
$J_{ph}$	Photocurrent, in $\text{A} \cdot \text{m}^{-2}$
$J_{ph}(\lambda)$	Photocurrent, in $\text{A} \cdot \text{m}^{-2}$
$\lambda$	Wavelength, in nm
$l$	Film thickness, in m
$\Delta m$	Mass change, in g
$\mu_q$	Shear modulus of quartz: $2.947 \times 10^{11} \text{ g} \cdot \text{cm}^{-1} \cdot \text{s}^{-2}$
$n$	number of exchanged electron
$n$	Transition parameter
$N_a$	Majority carrier density, in $\text{m}^{-3}$

$n_{\text{CPE}}$	CPE exponent
$N_e(\lambda)$	Number of extracted electrons
$N_{ph}(\lambda)$	Number of incident photons
$o$	Overtone
$\phi$	Phase shift, in s
$\Phi_{\text{AM 1.5}}$	Photon density of the AM 1.5 spectrum, in $\text{s}^{-1} \cdot \text{cm}^{-2}$
$\Phi_{\text{Xe lamp}}$	Photon density of Xenon arc lamp, in $\text{s}^{-1} \cdot \text{cm}^{-2}$
$\Phi_{\text{Xe lamp cal}}$	Photon density of Xenon arc lamp calibrated, in $\text{s}^{-1} \cdot \text{cm}^{-2}$
$p_{\text{H}_2}$	Partial pressure of $\text{H}_2$ , in Pa
$p_{\text{O}_2}$	Partial pressure of $\text{O}_2$ , in Pa
$q$	Electrical charge, in C
$Q$	Total charge, in $\text{mA} \cdot \text{V}$
$Q$	CPE capacitance, in C
$R$	Gas constant: $8.314 \text{ J} \cdot \text{mol}^{-1} \text{K}^{-1}$
$R$	Resistance, in $\Omega$
$R$	Reflectance, in %
$\rho_q$	Density of quartz: $2.648 \text{ g} \cdot \text{cm}^{-3}$
$R_s$	Serie resistance, in $\Omega$
$S$	Surface contact, in $\text{m}^{-2}$
$S_g$	Geometrical surface, in $\text{cm}^{-2}$
$\sigma$	Conductivity, in $\text{S} \cdot \text{m}^{-1}$
$T$	Transmittance, in %
$T$	Temperature, in K or $^{\circ}\text{C}$
$\vartheta$	Contact angle, in $^{\circ}$
$t$	Time, in s
$\delta w$	Raman shift, in $\text{cm}^{-1}$
$\omega$	Frequency, in $\text{s}^{-1}$



# Introduction **Part I**





# 1 Motivations and Background

On the 21<sup>st</sup> of may 2017, Swiss citizens have accepted the new energy law which schedule to close all nuclear power plants in Switzerland before 2050.<sup>1</sup> The preparation of this new law was started after the Fukushima disaster in 2011 which rose questions about security of nuclear energy. This technology has some advantages: as it is produced by the nuclear fission of a fuel nucleus,  $^{235}\text{U}$ , it is considered  $\text{CO}_2$  free. Moreover it is able to produce energy in large scale providing enough energy to satisfy energy demand. However during the fission of a nucleus, two daughter nuclei fragments are produced,  $^{141}\text{Ba}$  and  $^{92}\text{Kr}$  for the fission of  $^{235}\text{U}$ , that are unstable and hence radioactive. Dealing with theses radioactive wastes as well as a high amount of energy is challenging to ensure people safety.

In order to shut down the nuclear facilities and hence to replace this energy production, the Swiss Federal Council proposed, among others proposals, to support economically hydraulic power stations suffering today of their poor profitability due to the low electricity price. This proposal is unfortunately only possible in the short term. Indeed, according to the Swiss Federal Office of Energy (SFOE),<sup>2</sup> whose data are summarized in figure 1.1, the contribution of hydraulic power stations in 2014 amounts already to 56 % (39 300 GWh) of the total electricity produced already exceeding previsions of 38 980 GWh/y electricity production for 2050.<sup>3</sup> The part of electricity produced by nuclear power plant, corresponding to 38 % of electricity in 2014 (26 370 GWh), is too high to be totally replaced by hydraulic power.

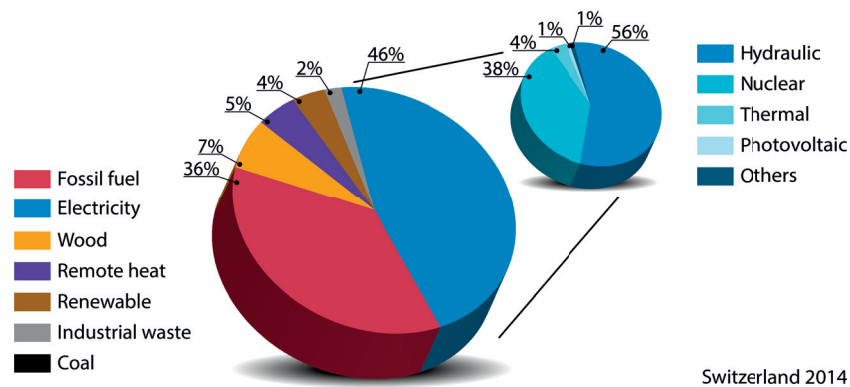


**Figure 1.1** – Swiss energy production in 2014 according to SFOE.<sup>2</sup>

The second proposal from the Swiss Federal Council is to promote the use of renewable energy. Not only this option favors environmental protection included in the new energy law goals<sup>4</sup> by limiting production of CO<sub>2</sub> responsible of global warming, but its impact on the energy market could be very influential.

There is still a lot of work to do for environmental preservation. Switzerland has signed the Paris agreement<sup>5</sup> to limit the temperature increase due to greenhouse gas emission, and implemented since 2012 a CO<sub>2</sub> emission regulation but fuel market is still powerful in Switzerland. As shown by data of SFOE in figure 1.2, 52 % of energy consumed in 2014 was by burning of fossil fuel. It is still a crucial energy input due to its use in the transportation and home heating field. To reduce our footprint on environment, fossil fuel then needs to also be replaced.

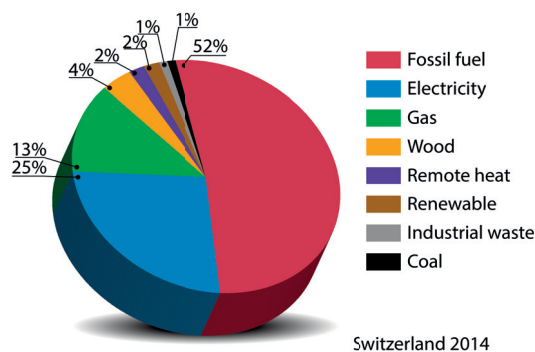


**Figure 1.2** – Swiss energy consumption in 2014 according to SFOE.<sup>2</sup>

Switzerland produces, in many different ways, 66 % of its consumed energy. As seen in figure 1.1 Switzerland uses different types of opportunity to produce energy either by hydraulic energy, thermal energy, burning of wood and industrial waste. On the other hand, part of energy produced from renewable technologies amounts to only 6 % \*. Although this market

\* taking into account electricity and heat production

is expanding, for example the energy produced by photovoltaic technology shows a drastic increase since 2007 as seen in figure 1.3, its contribution is for the moment very negligible. If promoted, this technology has a greater improvement margin and could have a big influence.

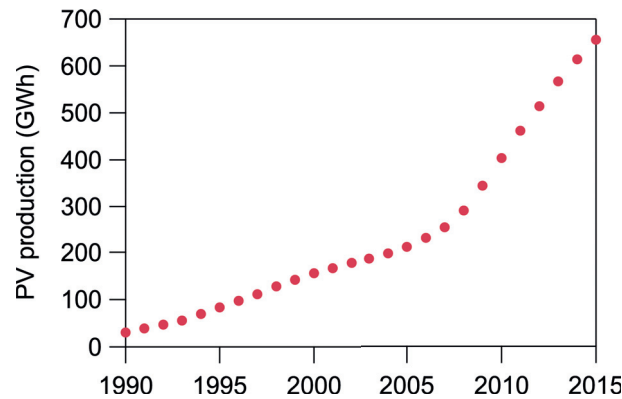


**Figure 1.3** – Swiss electricity production by photovoltaic panels per year according to SFOE.<sup>2</sup>

As said, energy already needs to be bought to satisfy energy consumption. Switzerland buys fossil fuel to convert it to fuel oil, nuclear combustible, electricity or gas from France which produces mainly from nuclear energy, and Germany, producing from coal. To follow new energy law which aims at protecting humans, animals and natural resources, Switzerland needs to be energetically independent. This way, nuclear and coal technology are hindered even outside of Swiss territory and therefore limit their effects. Indeed natural disaster, nuclear accident or global warming are not confined by borders.

Overall, Switzerland will need to find an environmentally benign and safe technology to produce locally its total energy consumption.

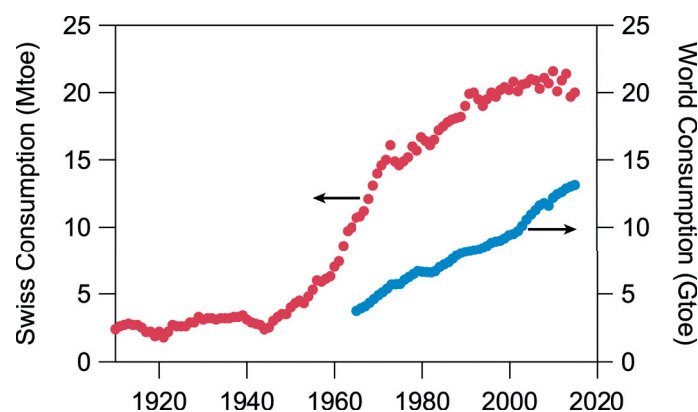


**Figure 1.4** – Swiss and world energy consumption per year according to SFOE<sup>2</sup> and BP.<sup>6</sup>

The rise of ecological awareness and the political support for the preservation of the en-

environment and energetic efficiency<sup>4</sup> in Switzerland results in a stabilization of energetic consumption since the 2000s, see red data in figure 1.4.

On the contrary, the total quantity of energy used in the world per year, blue data in figure 1.4 in a different scale, is still expanding and is expected to rise from 13 900 Mtoe<sup>†</sup> in 2012 to 20 500 Mtoe in 2040.<sup>7</sup> This prevision, done by the U.S. Energy Information Administration, took into account different effects such as demographic increase and industrialization of developing countries. Compared to Switzerland, the main concern of these countries will be to find a technology that could supply their large demand rather than ecological concern.

In a publication called “A fundamental look at energy reserves for the planet” Perez and Perez<sup>8</sup> evaluate that only solar and wind energy could produce enough energy to satisfy world energy demand, representing 16 TWh, with a total of 23 000 TWh per year provided by sun and 25 – 70 TWh per year provided by wind. Coal, uranium, petroleum and natural gas could potentially supply enough energy but only on short term as they are not renewable. Hence the technology which has the greatest potential to provide large amount of energy either to replace existing ones or to produce more energy is the conversion of solar energy.

### 1.1 Photovoltaic (PV) Technology

Many ways exist to convert solar energy into usable energy like electricity, heat or fuel. Among them Photovoltaic (PV) technology is well-known, commercially well developed. In this section, basics of PV mechanism will be described. Notions explained here will be used in the following work.

A semiconducting material is used to absorb light and convert it to electricity.<sup>9,10</sup> A semiconductor is defined a band structure in which possible energies of an electron within the solid are described by a range (bands) of energy in electronvolt scale (eV). Depending on the solid atomic composition, some of these bands are filled, i.e. an electron has this energy, and some of them are empty, i.e. there is no electrons with this energy. For comparison, these energies can also be related to an electrochemical potential, see chapter 3 page 33 with equation where  $E_{NHE}$  is the potential versus the Normal Hydrogen Electrode (NHE) in (V),  $|E_{vac}|$  is the absolute value of the energy versus the vacuum energy in (eV).

$$E_{NHE} = |E_{vac}| - 4.5 \quad (a.1)$$

A semiconductor has a valence band energy,  $E_{VB}$ : the energy of the last filled band, and a conduction band energy,  $E_{CB}$ : the energy of the first vacant band. Both are separated by a defined energy called the band gap,  $E_g$ , in which no electrons of this energy can exist. The Fermi level of the semiconductor  $E_F$ , or electrochemical potential for electrons, is the energy at which there is 50 % of chance to find an electron.

---

<sup>†</sup> Mtoe beeing Million Tonnes of Oil Equivalent corresponding to  $1.16 \times 10^{-2}$  GWh.

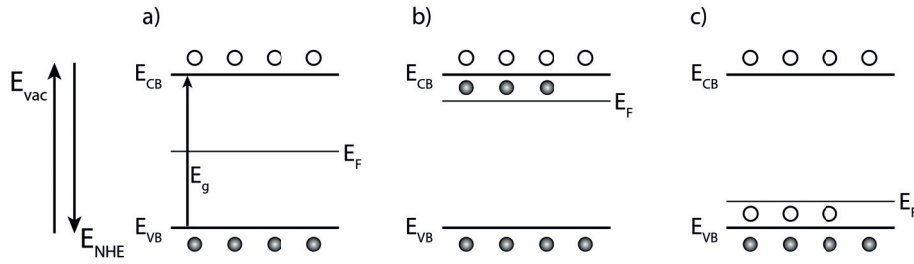


**Figure 1.5** – Semiconductor energetics at 0 K for a) an intrinsic, b) an n-type and c) a p-type semiconductor.

Semiconductors can carry two types of charges: electrons (n carriers) or holes (p carriers). The presence of an electron in the conduction band, or with  $E_{CB}$  energy, or a hole in the valence band, or with  $E_{VB}$  energy, are necessary to conduct electricity. As seen in figure 1.5 a) for an intrinsic semiconductor at 0 K, electrons represented by a full circle are all located in the valence band and holes, represented by empty circle are in the conduction band. At room temperature, an electron can be thermally excited to the conduction band. Hence the probability to find an electron,  $E_F$ , is located in the middle of the valence and conduction band.

A semiconductor will be extrinsic if doped with an electron rich (n-type doping, called an n-type semiconductor) or an electron deficient (p-type doping, called a p-type semiconductor) materials.

In an n-type semiconductor,  $E_F$  is moved close to  $E_{CB}$  because extra electrons can only go in the conduction band, figure 1.5 b). The probability to find an electron (its majority carriers) in the conduction band is high and it will be able to conduct electricity by electron movement. In a p-type semiconductor,  $E_F$  is moved close to  $E_{VB}$  because extra holes can only go in the valence band, figure 1.5 c). The probability to find a hole (its majority carriers) in the valence band is high and it will conduct electricity by hole movement. Therefore doping of semiconductor results then in an enhanced conductivity.

A PV cell is made by contacting an n-type and a p-type semiconductors together, see figure 1.6 a). At their interface, a non rectifying junction will be formed due to the rearrangement of charges in the semiconductors. Indeed, as the n-type semiconductor is full of electrons and the p-type semiconductor is full of holes, their Fermi level will equilibrate by charge movement. The n-type semiconductor will move its electrons from its surface to the p-type semiconductor, resulting in an overall decrease of  $E_F$  (and shift of  $E_{VB}$  and  $E_{CB}$  as well) and the p-type will fill its holes with electrons from the n-type semiconductor, resulting in an increase of  $E_F$  (and shift of  $E_{VB}$  and  $E_{CB}$  as well). This will form a positively charged interface in the n-type side and a negatively charged interface in the p-type side, forming an electric field, as seen in figure 1.6 b).

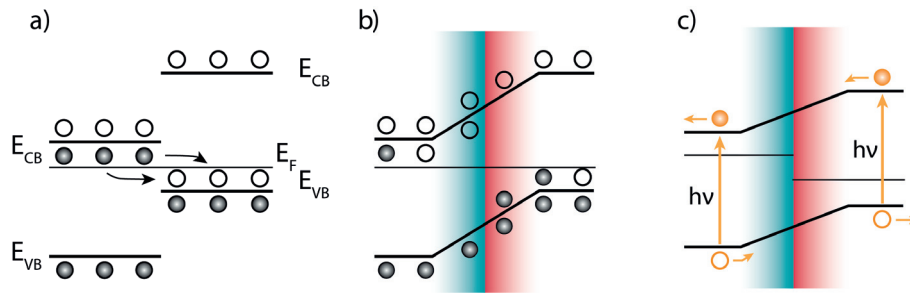


**Figure 1.6** – Formation of a n-p junction by contacting an n-type and a p-type semiconductor. a) before equilibrium, b) after equilibrium with the formation of a positively charge region (blue) and negatively charge region (red) and c) photoexcitation process under illumination.

As electrons can be thermally excited, they can also be photoexcited. In this case, light (or photon) with equal or higher energy than  $E_g$  is absorbed resulting in an electron excitation in  $E_{CB}$  leaving a hole in  $E_{VB}$ . Once excited, electrons tends to lose their energy, this can be done by recombination where an electron will recombine with a hole and losses its energy by light emission. In this case no current will flow. However as an electric field is formed at the n-p junction, excited electrons and holes are directly separated. For example, a photon absorbed in the n-type semiconductor will create an electron in its conduction band which will move away from its positive region, see figure 1.6 c). At the same time, a hole will be formed in the valence band and will move across the positive region. By forcing the electrons through an external circuit, creating an electric current, both will recombine in the other side of the interface.

Commercial PV panel can be found with a solar-to-electricity efficiency around 20 %. This efficiency is already sufficient to produce energy for a house, depending on geographical location and surface of PV coverage. However the main drawback of this technology is its intermittent behavior since electricity is produced only once the solar panel is under illumination. This becomes problematic during night or winter when electricity is needed for light or heat while illumination is low or absent.

In order to face this problem, PV installation are now coupled with a battery. The extra electricity produced during the day is used to charge a battery which is used once the PV cells do not produce anymore. This is the case for example for the only self-sufficient house in Switzerland<sup>11</sup> where a total photovoltaic installation of 15 kW is used to produce electricity for the house and to charge a Lithium battery of 48 V. This installation provide enough energy for the house during all seasons with the use of energy efficient devices.

Up-to-now, batteries (and water heating) are the only commercial installations for the solar energy storage. Even if they are able to reduce intermittence of electricity production of PV technology, their storage is still limited in time. Batteries are limited by their charge capacities and charging/discharging time which reduces usable time. It is then very appropriate for a

small house which has to face daily variations but it comes more difficult to face seasonal variations.

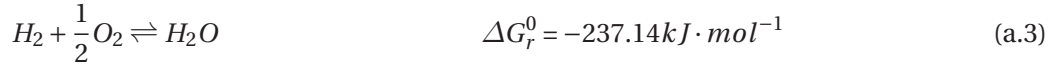
## 1.2 Solar-to-Hydrogen (STH) Technology

Inspired by nature where solar energy is stored as sugar, the storage of solar energy could also be done through the formation of a chemical bond. During the photosynthesis for example, a plant create a sugar by the absorption of light with equation a.2. It then uses this sugar as energy input in the cell. This is called the solar-to-fuel technology were energy is stored as a chemical bond. This energy can then be recovered by decomposition of the chemical bond. The fuel, as oil, can be stored, distributed and used upon demand.

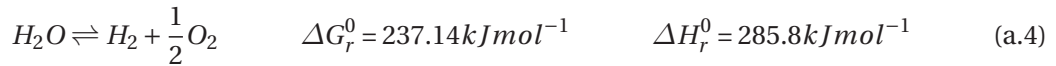


One of the best storage chemical candidate is hydrogen as it is a carbon free compound and hence will not release  $CO_2$  during decomposition. Moreover the technology to use it is already available since 1838 with the invention of the fuel cell.

In this technology,  $H_2$  reacts with  $O_2$  to form  $H_2O$  with equation a.3. As the free Gibbs energy is negative, this reaction is spontaneous. To happen,  $H_2$  needs to transfer electrons to  $O_2$ . By forcing the electrons through an external circuit, an electric current is formed.



To produce hydrogen,<sup>12</sup> the reverse reaction a.4 can be used. This reaction is called water splitting because water is split into molecular hydrogen and oxygen.



The reaction is not spontaneous, an energy equivalent to  $237.14 kJ \cdot mol^{-1}$  is needed to drive it at 1 bar and  $25^\circ C$  corresponding an electrical work given by equation a.5 where  $R$  is the gas constant:  $8.314 J \cdot mol^{-1} K^{-1}$ ,  $T$  the temperature in (K),  $p_{H_2}$  the partial pressure of hydrogen in (Pa),  $p_{O_2}$  the partial pressure of oxygen in (Pa) and  $a_{H_2O}$  the activity of water.

$$w_{el} = \Delta G = \Delta G^0(T) + RT \ln \left( \frac{p_{H_2} \cdot p_{O_2}^{1/2}}{a_{H_2O}} \right) \quad (a.5)$$

In the theoretical case where pur  $H_2O$  is used and  $H_2$  and  $O_2$  are produced at 1 bar this work turns out to be  $\Delta G^0(T)$ . By using electrical current, the potential needed to split water is given by equation a.6 where  $n$  is the number of exchanged electron during the reaction (2)

## Chapter 1. Motivations and Background

and  $F$  the Faradaic constant  $96\,500\text{ C} \cdot \text{mol}^{-1}$ .

$$E(T) = \frac{\Delta G}{nF} = \frac{\Delta G^0}{nF} = 1.229\text{ V} \quad (\text{a.6})$$

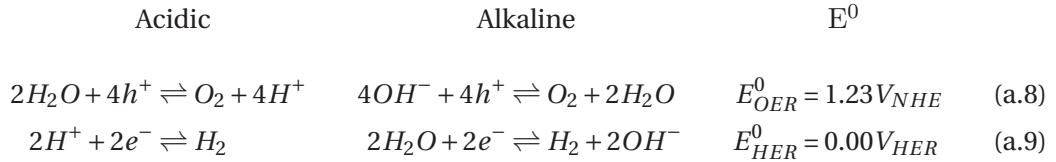
The enthalpy of reaction is  $285.8\text{ kJ} \cdot \text{mol}^{-1}$  at 1 bar and  $25^\circ\text{C}$  describing an endothermic reaction. This means that the potential needed to conduct the reaction isothermally,  $E_{th}$ , is given by equation a.7 (again for pure water and  $\text{H}_2$  and  $\text{O}_2$  at 1 bar,  $n = 2$  and  $F = 96\,500\text{ C} \cdot \text{mol}^{-1}$ ):

$$E_{th}(T) = \frac{\Delta H}{nF} = \frac{\Delta H^0}{nF} = 1.481\text{ V} \quad (\text{a.7})$$

Any potential higher than  $E_{th}$  will lead to heat release which could lead to other decomposition reactions.

In real conditions, water is not pure ( $a_{\text{H}_2\text{O}} < 1$ ) and  $\text{H}_2$  and  $\text{O}_2$  are water saturated which reduces their partial pressure. In this case the potential that must be applied to drive the reaction will be reduced  $\left( \frac{p_{\text{H}_2} \cdot p_{\text{O}_2}^{1/2}}{a_{\text{H}_2\text{O}}} < 1 \right)$ .

In an electrolyzer, a device to produce  $\text{H}_2$  with electrical energy, the reaction is performed with an electrochemical cell, see chapter 3 page 33. The anode drives the Oxygen Evolution Reaction (OER) by injection of holes in the electrolyte at potential  $E_{\text{OER}}^0$ , (equation a.8) and the cathode drives the Hydrogen Evolution Reaction (HER) by injection of electrons in the electrolyte at potential Hydrogen Evolution Reaction (HER) (equation a.9).



As mentioned before the overall process needs a potential of  $1.23\text{ V}$  to overcome the thermodynamics barriers.

However due to kinetic barriers,<sup>13</sup> an overpotential, i.e. extra energy, is necessary. Indeed, depending on material used in the electrodes, mechanisms of reactions or charge extraction efficiency can be different. This extra energy also depends on number of charge needed, therefore the overpotential for oxidation reaction is higher than the overpotential for reduction reaction as the first one needs four holes to form  $\text{O}_2$  and the second one two electrons to form  $\text{H}_2$ . An overall potential, around  $1.8\text{ V}$ , is the given by equation a.10 where  $E_{\text{tot}}$  is the total potential to apply in (V),  $E$  is the theoretical potential ( $1.23\text{ V}$ ) in (V),  $\eta_{ox}$  is the overpotential for the oxidation reaction in (V),  $\eta_{red}$  is the overpotential for the reduction reaction in (V) and  $\eta_{cell}$  in the overpotential needed to overcome the cell configuration resistance.

$$E_{\text{tot}} = E + \eta_{ox} + \eta_{red} + \eta_{cell} \quad (\text{a.10})$$



### 1.3 Photoelectrochemical (PEC) Technology

Electrolyzers require electrical energy. In our case we want to use solar energy to drive the water splitting reaction. Two main alternatives are possible:<sup>14</sup> the first one with photocatalytic cell where a suspension of semiconductor material is used to produce hydrogen and oxygen in situ and the second one with Photoelectrochemical (PEC) cells where light absorber are in the form of electrodes. In this work, we will focus on PEC configuration. The following section will explain their mechanisms.

In PEC technology,<sup>10,13,15</sup> a semiconductor absorbs light and directly converts its energy in a chemical energy. In this case, the semiconductor is immersed in an electrolyte solution defined by  $E_{F,redox}$  the energy of electrons in the electrolyte, figure 1.7 a) and d). Once immersed,  $E_F$  of the semiconductor will equilibrate with  $E_{F,redox}$  of the electrolyte by charge rearrangement. On the semiconductor side, electrons or holes will move to the electrolyte resulting in  $E_{VB}$  and  $E_{CB}$  movement. The interface will either be positively charged, for an n-type semiconductor figure 1.7 b), or negatively charged, for a p-type semiconductor figure 1.7 e), therefore the  $E_{VB}$  and  $E_{CB}$  across this part of the semiconductor are not constant. This region, where  $E_{VB}$  and  $E_{CB}$  depends on the distance in the semiconductor, is called the space charge layer.

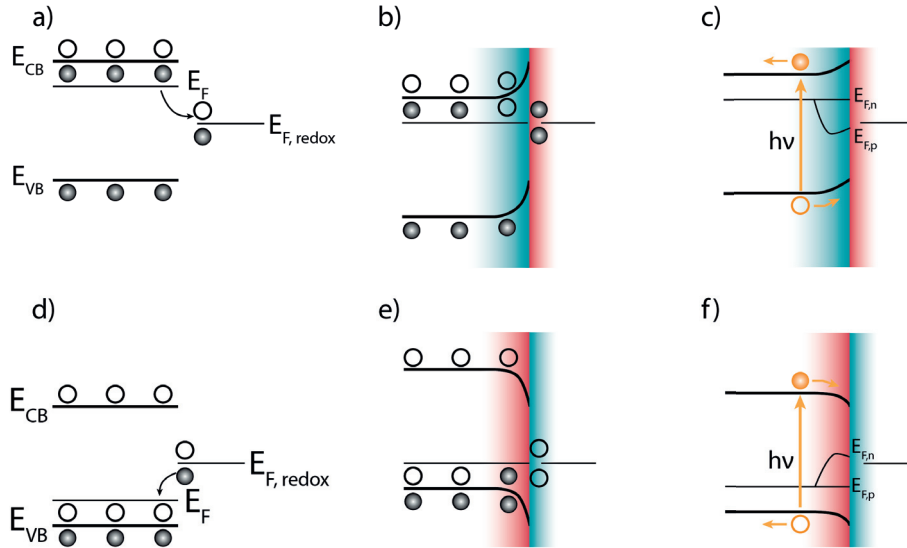


**Figure 1.7** – Representation of the Semiconductor-liquid Junction (SCLJ) for a), b) and c) an n-type and d), e) and f) p-type semiconductors. a) and d) before equilibrium, b) and e) at equilibrium and c) and f) under illumination.

On the electrolyte side,  $E_{F,redox}$  will also move to equilibrate with  $E_F$  of the semiconductor.<sup>9</sup> This will be realized by moving ions close to the semiconductor forming the so-called double layer. A first layer of ionic species will adsorb on the semiconductor by electron exchange with the semiconductor. Then to compensate the charge of the first layer a second layer made of solvated ions with opposite charge will approach the first layer. The total of both

## Chapter 1. Motivations and Background

---

layers is called the Helmholtz layer. Finally, charges will continue to be compensated in the solution until the bulk electrolyte where charges are in equilibrium. This second part is called the diffuse layer, or Gouy layer, and its thickness will depend on ionic concentration in the electrolyte.

A potential drop is formed across the total interface.  $E_{SC}$  in the semiconductor side (the difference between the energy where bands are flat  $E_{fb}$ , i.e. before equilibrium, and the energy of band at equilibrium),  $E_H$  and  $E_G$  in the electrolyte, the potential drop across the Helmholtz and the diffuse layer respectively. This potential drop ( $E_{SC} + E_H + E_G$ ) forms an electric field in the Semiconductor-liquid Junction (SCLJ) similar to the n-p junction. This is classically known as a Schottky junction.

Under illumination, figure 1.7 c) and f), the semiconductor will absorb light with the same or higher energy than  $E_g$  resulting in an excited electron in the conduction band and a hole in the valence band. A second steady state condition is therefore reached where the equilibrium is achieved between the electrolyte and the quasi Fermi level of electrons ( $E_{F,n}$ ) and holes ( $E_{F,p}$ ). These two new energy levels are formed due to the new population of electrons and holes in the semiconductor. These charges will then be separated by the electric field at the SCLJ where they can react with redox species in the electrolyte. For an n-type semiconductor, holes will be transported to the SCLJ to be transferred to oxidize species in the electrolyte. For a p-type semiconductor, electrons will be transported to the SCLJ to be transferred to achieve a reduction reaction.

This transformation of solar energy into a chemical bond can be realized through several configurations. The simpler one is the photovoltaic-electrolyzer configuration, figure 1.8 a), which uses a Photovoltaic (PV) cell to provide sufficient voltage to use an electrolyzer. Electrolyzer can be separated or integrated in the PV cell as in figure 1.8 a). Such devices have some advantages: only three PV cells, of 0.5 – 0.6  $V_{OC}$ , are needed to provide 1.8 V and as PV cells are not directly in contact with the electrolyte where the reaction takes place, stability issues will only be related to each device stability. One could also note that since light absorption/charge generation and electrolysis are separated, each of them can be optimized separately. However it will increase electron transfer steps which implies multiple losses. The price of the overall system is then limited by the price of each component which gives a production price of hydrogen around 10 US\$  $kg^{-1}$ . In laboratory scale,<sup>16</sup> state-of-the-art PV-electrolyzer device was made by Licht et al.<sup>17</sup> where a monolithic PV made of  $Al_{0.15}Ga_{0.85}As(pn)Si(pn)$  and integrated Pt and  $RuO_2$  catalyst produces hydrogen and oxygen with a 18.5 % STH efficiency and a stability over 14 hours.

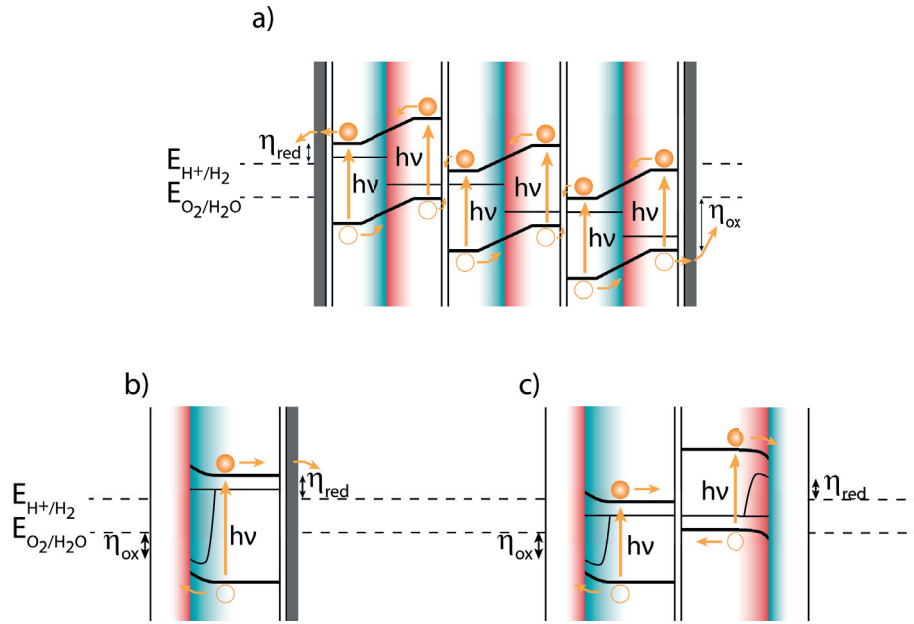


**Figure 1.8** – a) the PV-electrolyser, b) the S2 and c) the D4 PEC configuration.

In order to minimize the configuration complexity, and hence the cost, other configurations use the SCLJ to separate charges as in the S2, figure 1.8 b), or D4, figure 1.8 c) devices proposed by Bolton, Strickler, and Connolly.<sup>18</sup> In the S2 case, a single absorber is used to produce photogenerated charges with enough energies to drive both reactions. For this, the  $E_{VB}$  should be positive enough to drive the OER and the  $E_{CB}$  negative enough to drive the HER. Up to now only  $TiO_2$  was found to be able to work in this configuration. However this material has a large band gap of 3.2 eV corresponding to absorption of light in the Ultraviolet (UV) region (with energy under 387 nm). Light provided by the sun at this energy is less abundant than visible light which leads to low current density, maximum of  $1 \text{ mA} \cdot \text{cm}^{-2}$ , produced with  $TiO_2$  semiconductor.<sup>18</sup>

Instead the D4 or tandem cell approach, in figure 1.8 c), in which both reactions are separated at a photoanode and photocathode as in an electrolyzer.<sup>19</sup> Hence each component for each reactions can be optimized with adequate band position management, positive  $E_{VB}$  for photoanode and negative  $E_{CB}$  for photocathode. Moreover light harvesting can be enhanced by placing each electrodes on top of each other. In this case, light not absorbed by the top semiconductor will be transmitted and absorbed by the second one. Such device could potentially work at 21.6 % Solar-to-Hydrogen (STH) efficiency<sup>‡</sup> compared to 12.7 % STH<sup>§</sup> for S2 configuration<sup>15</sup> (41 % STH for the D4 and 30 % STH for the S2 without loss considerations). Best device in this configuration<sup>16</sup> was made in 1987 by Kainthla, Zelenay, and Bockris<sup>20</sup> where a p-InP(Pt) photocathode and a  $Mn_{ox}/Pt/n\text{-GaAs}$  photoanode were used in a side-by-side configuration. This device produces hydrogen and oxygen with 8.2 % STH efficiency and as

<sup>‡</sup> considering an energy loss of 2 eV and materials with band gap of 1.89 eV and 1.34 eV.

<sup>§</sup> considering the same energy loss of 2 eV and a material with a band gap of 2.23 eV.

shown a stability over 10 hours with 10 % drop in current.

### 1.3.1 Challenges for Photoelectrochemical (PEC) Technology

Despite these successful demonstrations, it is important to point out that any PEC technology must compete with the PV-electrolyser. Challenges are now to minimize device cost by using inexpensive and abundant material as well as cheap/affordable preparation. For that the "10:10:10" goal was suggested<sup>21</sup> to be sufficient with a 10 % STH efficiency, a lifetime of 10 years with a price of 10 \$ · kg<sup>-1</sup> of H<sub>2</sub>. Therefore, any PEC system for converting solar energy into fuel must find a balance between minimizing system complexity, i.e. device cost, and maximizing device performance, i.e. energy conversion efficiency and device longevity.

Metals oxides are believed to drastically reduce prices of D4 cells. Indeed, they are cheap, stable materials and solution-based processes like sol-gel, spray pyrolysis, or hydrothermal routes can be easily used, followed by thermal annealing to obtain oxide thin-film electrodes without expensive processing techniques. Among them we can cite TiO<sub>2</sub>,<sup>22,23</sup> p-types Cu<sub>2</sub>O<sup>24</sup> and CuFe<sub>2</sub>O<sub>4</sub>,<sup>25</sup> and n-types BiVO<sub>4</sub>,<sup>26</sup> WO<sub>3</sub>,<sup>27,28</sup> and Fe<sub>2</sub>O<sub>3</sub>.<sup>29</sup> While they usually are efficient absorber, they suffer from poor catalytic efficiency leading to high overpotential. For that low loading of catalyst can be deposited on top of the semiconductor to enhance reaction efficiency. However only a few of them were proved effective in a full device configuration.<sup>16</sup>

In this work, we demonstrate the feasibility of such tandem cell by using a BiVO<sub>4</sub> photoanode prepared by van de Krol's group<sup>26</sup> and a Cu<sub>2</sub>O photocathode prepared by Grätzel's group.<sup>24</sup> Results can be found in chapter 4 page 51 where we showed that a full oxide tandem cell is possible using low cost production techniques. With a catalyst on photoanode surface, a protecting layer and a catalyst at photocathode surface, we obtained a 0.5 % STH efficiency and a stability over the course of minutes.<sup>30</sup>

Despite the use of state-of-the-art oxides photoelectrodes, efficiency and stability of the whole cell are still far from being competitive. New materials are needed to reach our constraints and we noticed that a tunable material, i.e. a material in which the energetics can be optimized, would help to adjust one electrode with the characteristics of the other.

### 1.3.2 Organic Semiconductors

Another type of material that could be interesting are organic semiconducting materials.<sup>31</sup> These carbon based (sp<sup>2</sup>) materials combine advantages of metal oxides and organic material. As hybridization state of  $\pi$ -bonds results in different energy levels called Highest Occupied Molecular Orbital (HOMO) and Lowest Unoccupied Molecular Orbital (LUMO), similar to valence band and conduction band, they can also act as a semiconductor. Therefore they can absorb light (or emit light) in the visible region leading to electrical conductivity but they are also made by chemical synthesis which offer a broad choice of chemical component to match desired light interaction, energetics and so on.

Furthermore solution processing can be used where thin films are formed with the use of an ink containing the material in solution. These solution processing techniques as spin coating, dip coating or spray coating, described in chapter 5.2 page 69, are less energy demanding and easier to prepare large area of films. In summary, compared to inorganic materials, organic materials offer easier tunability, synthesis and processing leading to competitive prices and scalable device fabrication.

Energetics theory of semiconductor, as explained before, can also be applied to organic semiconductors. As said, their HOMO and LUMO energy level correspond to the valence band and conduction band in inorganic material. They can be doped by injection of charges either by changing their chemical structure, by insertion of an other compound or by electrochemistry. For organic materials, an n-type is defined as an electron transporting material and a p-type as a hole transporting material.

Compare to inorganic semiconductor they have a much lower dielectric constant<sup>¶</sup> therefore their charge extraction process is different. The dielectric constant of an inorganic material is high ( $\epsilon_r = 11.9$  for silicon) which means that there is no Coulombic effect between electrons and holes in the material. Upon photoexcitation, free charges can then be generated. Due to the low dielectric constant in organic material (around  $\epsilon_r = 4.4$  for P3HT) upon photoexcitation, electrons and holes are still bound by a Coulombic attraction. This electron-hole pair is called an exciton. To create an electrical current, excitons needs to be dissociated by an electric field at interfaces like a n-p junction or a SCLJ, which will drive both charges in different directions.

While their promising aspects have motivated intense investigation for economical roll-to-roll Organic Photovoltaic (OPV) devices, due to their poor stability in aqueous conditions, they have not been generally pursued as photoelectrodes for direct solar water splitting, except for HER.<sup>32</sup> Encapsulated OPVs have recently been demonstrated in PV-biased photoelectrosynthetic cells for solar water splitting,<sup>33–35</sup> but the lack of intrinsic material stability limits their application in this configuration. Polymeric carbon nitride based materials<sup>36</sup> and conjugated microporous network polymers<sup>37</sup> have recently shown promising performance for the direct solar water reduction, suggesting that conjugated carbon-based materials can be suitable as photocathodes.

However, the task of identifying suitable  $\pi$ -conjugated materials for the photoanode is more difficult due to the harsh conditions of PEC water oxidation.<sup>38</sup> Organic dyes based on porphyrins or Perylene Diimides (PDI) can possess HOMO levels suitable for water oxidation in certain conditions.<sup>39–42</sup> However, solution-processing these materials can be problematic given their strong tendency to aggregate.<sup>43</sup> As certain conjugated polymers can possess similar energy levels to porphyrin and PDI dyes while also exhibiting superior film forming characteristics and improved intrinsic stability, in this work we hypothesized that they could be viable candidates for inexpensive solution-processed photoanodes.

---

<sup>¶</sup>ability to store electrical energy in an electric field.  $\epsilon_r$  is the ratio between the absolute permittivity of the material and the vacuum permittivity  $\epsilon_0 = 8.85 \times 10^{-12} \text{ A} \cdot \text{s} \cdot \text{V}^{-1} \text{ m}^{-1}$ .

### 1.4 Summary

In this work, after a presentation of the experimental techniques used for the optical and physical characterization of our sample, in chapter 2 page 23, and electrochemical characterization, 3 page 33, we will first demonstrate the feasibility of an all oxide PEC tandem cell in chapter 4 page 51. Drawing conclusions for this device will lead us to the presentation of an organic material, in chapter 5 page 67, which can potentially be used as a photoanode in a tandem cell. We will then demonstrate, in chapter 6 page 79, its successful use for OER under illumination. Finally, extended characterization of this material in chapter 7 page 95 will help to understand the mechanism governing charge transport in our films.

### References

- [1] Confédération suisse. *Votation populaire du 21 mai 2017 Explications du Conseil fédéral - Loi sur l'énergie (LEne)*. Feb. 2017. URL: <https://www.admin.ch/gov/fr/accueil/documentation/votations/20170521/Loi-sur-l-energie.html>.
- [2] Confédération suisse. *Statistique globale suisse de l'énergie 2015*. Tech. rep. Office fédéral de l'énergie (ORFEN), 2015. URL: [http://www.bfe.admin.ch/themen/00526/00541/00542/00631/?lang=fr%5C&dossier\\_id=00763](http://www.bfe.admin.ch/themen/00526/00541/00542/00631/?lang=fr%5C&dossier_id=00763).
- [3] Confédération suisse. *Le potentiel hydroélectrique de la Suisse - Potentiel de développement de la force hydraulique au titre de la stratégie énergétique 2050*. Office fédéral de l'énergie OFEN. June 2012. URL: [http://www.bfe.admin.ch/themen/00490/00491/index.html?lang=fr&dossier\\_id=00803](http://www.bfe.admin.ch/themen/00490/00491/index.html?lang=fr&dossier_id=00803).
- [4] Confédération suisse. *Loi fédérale sur la protection de l'environnement (LPE)*. Jan. 2017. URL: <https://www.admin.ch/opc/fr/classified-compilation/19830267/index.html>.
- [5] United Nations Framework Convention on Climate Change. *The Paris Agreement - main page*. May 2017. URL: [http://unfccc.int/paris\\_agreement/items/9485.php](http://unfccc.int/paris_agreement/items/9485.php).
- [6] BP. *Statistical Review of World Energy*. 2016. URL: <http://www.bp.com/en/global/corporate/energy-economics/statistical-review-of-world-energy.html>.
- [7] *International Energy Outlook 2016*. Tech. rep. U.S. Energy Information Administration (EIA), 2016. URL: <https://www.eia.gov/outlooks/ieo/>.
- [8] R. Perez and M. Perez. "A fundamental look at energy reserves for the planet". *The International Energy Agency SHCP Solar Update 50* (2009), pp. 2–3. URL: <http://www.iea-shc.org/data/sites/1/publications/2009-04-SolarUpdate.pdf>.
- [9] Allen J. Bard and Larry R. Faulkner. *Electrochemical Methods: Fundamentals and Applications, 2nd Edition*. Wiley, 2001. URL: <http://eu.wiley.com/WileyCDA/WileyTitle/productCd-04711043729.html>.
- [10] A. J. Bard, M. Stratmann, and S. Licht. "Semiconductor Electrodes and Photoelectrochemistry". *Encyclopedia of Electrochemistry*. Vol. 6. Wiley-CH, 2002.



- 
- [11] *En Autarcie - main page*. May 2017. URL: [www.en-autarcie.ch](http://www.en-autarcie.ch).
- [12] Claude Béguin, ed. *Une Chronique de l'Hydrogène. Histoire des méthodes de production et des applications*. Presses Polytechniques et Universitaires Romandes, 2016.
- [13] Michael G. Walter, Emily L. Warren, James R. McKone, Shannon W. Boettcher, Qixi Mi, Elizabeth A. Santori, and Nathan S. Lewis. "Solar Water Splitting Cells". *Chemical Reviews* 110 (2010), pp. 6446–6473. DOI: 10.1021/cr1002326.
- [14] Adam C. Nielander, Matthew R. Shaner, Kimberly M. Papadantonakis, Sonja A. Francis, and Nathan S. Lewis. "A Taxonomy for Solar Fuels Generators". *Energy & Environmental Science* 8 (1 2015), pp. 16–25. DOI: 10.1039/C4EE02251C.
- [15] Mathieu S. Prévot and Kevin Sivula. "Photoelectrochemical Tandem Cells for Solar Water Splitting". *The Journal of Physical Chemistry C* 117 (2013), pp. 17879–17893. DOI: 10.1021/jp405291g.
- [16] Joel W. Ager, Matthew R. Shaner, Karl A. Walczak, Ian D. Sharp, and Shane Ardo. "Experimental Demonstrations of Spontaneous, Solar-Driven Photoelectrochemical Water Splitting". *Energy & Environmental Science* 8 (10 2015), pp. 2811–2824. DOI: 10.1039/C5EE00457H.
- [17] S. Licht, B. Wang, S. Mukerji, T. Soga, M. Umeno, and H. Tributsch. "Efficient Solar Water Splitting, Exemplified by RuO<sub>2</sub>-Catalyzed AlGaAs/Si Photoelectrolysis". *The Journal of Physical Chemistry B* 104.38 (2000), pp. 8920–8924. DOI: 10.1021/jp002083b.
- [18] James R. Bolton, Stewart J. Strickler, and John S. Connolly. "Limiting and Realizable Efficiencies of Solar Photolysis of Water". *Nature* 316 (1985), pp. 495–500. DOI: 10.1038/316495a0.
- [19] K. Ohashi, J. McCann, and J. O'M. Bockris. "Stable Photoelectrochemical Cells for the Splitting of Water". *Nature* 266 (1977), pp. 610–611. DOI: 10.1038/266610a0.
- [20] R. C. Kainthla, B. Zelenay, and J. O'M. Bockris. "Significant Efficiency Increase in Self-Driven Photoelectrochemical Cell for Water Photoelectrolysis". *Journal of The Electrochemical Society* 134.4 (1987), pp. 841–845. DOI: 10.1149/1.2100583.
- [21] Blaise A. Pinaud, Jesse D. Benck, Linsey C. Seitz, Arnold J. Forman, Zhebo Chen, Todd G. Deutsch, Brian D. James, Kevin N. Baum, George N. Baum, Shane Ardo, Heli Wang, Eric Miller, and Thomas F. Jaramillo. "Technical and Economic Feasibility of Centralized Facilities for Solar Hydrogen Production Via Photocatalysis and Photoelectrochemistry". *Energy & Environmental Science* 6 (7 2013), pp. 1983–2002. DOI: 10.1039/C3EE40831K.
- [22] Akira Fujishima and K. Honda. "Electrochemical Photolysis of Water at a Semiconductor Electrode". *Nature* 238 (1972), pp. 37–38. DOI: 10.1038/238037a0.
- [23] Akira Fujishima, Xintong Zhang, and Donald A. Tryk. "TiO<sub>2</sub> Photocatalysis and Related Surface Phenomena". *Surface Science Reports* 63 (2008), pp. 515–582. DOI: 10.1038/238037a0.

- [24] S. David Tilley, Marcel Schreier, João Azevedo, Morgan Stefik, and Michael Grätzel. “Ruthenium Oxide Hydrogen Evolution Catalysis on Composite Cuprous Oxide Water-Splitting Photocathodes”. *Advanced Functional Materials* 24 (2014), pp. 303–311. DOI: 10.1002/adfm.201301106.
- [25] Mathieu S. Prévot, Néstor Guijarro, and Kevin Sivula. “Enhancing the Performance of a Robust Sol-Gel-Processed p-Type Delafossite  $\text{CuFeO}_2$  Photocathode for Solar Water Reduction”. *ChemSusChem* 8 (2015), pp. 1359–1367. DOI: 10.1002/cssc.201403146.
- [26] Fatwa F. Abdi, Lihao Han, Arno H. M. Smets, Miro Zeman, Bernard Dam, and Roel van de Krol. “Efficient Solar Water Splitting by Enhanced Charge Separation in a Bismuth Vanadate-Silicon Tandem Photoelectrode”. *Nature Communications* 4 (2013), p. 2195. DOI: 10.1038/ncomms3195.
- [27] Clara Santato, Martine Ulmann, and Jan Augustynski. “Photoelectrochemical Properties of Nanostructured Tungsten Trioxide Films”. *The Journal of Physical Chemistry B* 105 (2001), pp. 936–940. DOI: 10.1021/jp002232q.
- [28] Gary Hodes, David Cahen, and Joost Manassen. “Tungsten Trioxide As a Photoanode for a Photoelectrochemical Cell (PEC)”. *Nature* 260 (1976), pp. 312–313. DOI: 10.1038/260312a0.
- [29] Kevin Sivula, Florian Le Formal, and Michael Grätzel. “Solar Water Splitting: Progress Using Hematite ( $\alpha\text{-Fe}_2\text{O}_3$ ) Photoelectrodes”. *ChemSusChem* 4 (2011), pp. 432–449. DOI: 10.1002/cssc.201000416.
- [30] Pauline Borno, Fatwa F. Abdi, S. David Tilley, Bernard Dam, Roel van de Krol, Michael Grätzel, and Kevin Sivula. “A Bismuth Vanadate-Cuprous Oxide Tandem Cell for Overall Solar Water Splitting”. *The Journal of Physical Chemistry C* 118 (2014), pp. 16959–16966. DOI: 10.1021/jp500441h.
- [31] Wallace C.H. Choy, ed. *Organic Solar Cells – Materials and Device Physics*. Springer London, 2013. DOI: 10.1007/978-1-4471-4823-4.
- [32] Shozo Yanagida, Akira Kabumoto, Kunihiro Mizumoto, Chyongjin Pac, and Katsumi Yoshino. “Poly(p-phenylene)-Catalysed Photoreduction of Water to Hydrogen”. *Journal of the Chemical Society, Chemical Communications* 8 (8 1985), pp. 474–475. DOI: 10.1039/C39850000474.
- [33] Toshiyuki Abe, Shunsuke Tobinai, Naohiro Taira, Junpei Chiba, Takashi Itoh, and Keiji Nagai. “Molecular Hydrogen Evolution by Organic p/n Bilayer Film of Phthalocyanine/-Fullerene in the Entire Visible-Light Energy Region”. *The Journal of Physical Chemistry C* 115 (2011), pp. 7701–7705. DOI: 10.1021/jp1094992.
- [34] Tiphaine Bourgeteau, Denis Tondelier, Bernard Geffroy, Romain Brisse, Christel Laberty-Robert, Stephane Campidelli, Remi de Bettignies, Vincent Artero, Serge Palacin, and Bruno Jusselme. “A  $\text{H}_2$ -evolving Photocathode Based on Direct Sensitization of  $\text{MoS}_3$  with an Organic Photovoltaic Cell”. *Energy & Environmental Science* 6 (9 2013), pp. 2706–2713. DOI: 10.1039/C3EE41321G.



- [35] Antonio Guerrero, Marta Haro, Sebastiano Bellani, Maria Rosa Antognazza, Laura Meda, Sixto Gimenez, and Juan Bisquert. "Organic Photoelectrochemical Cells with Quantitative Photocarrier Conversion". *Energy & Environmental Science* 7 (11 2014), pp. 3666–3673. DOI: 10.1039/C4EE01775G.
- [36] Xinchun Wang, Kazuhiko Maeda, Arne Thomas, Kazuhiro Takanabe, Gang Xin, Johan M Carlsson, Kazunari Domen, and Markus Antonietti. "A Metal-Free Polymeric Photocatalyst for Hydrogen Production from Water under Visible Light". *Nature Materials* 8 (2009), pp. 76–80. DOI: 10.1038/nmat2317.
- [37] Reiner Sebastian Sprick, Jia-Xing Jiang, Baltasar Bonillo, Shijie Ren, Thanchanok Ratvijitvech, Pierre Guiglion, Martijn A. Zwijnenburg, Dave J. Adams, and Andrew I. Cooper. "Tunable Organic Photocatalysts for Visible-Light-Driven Hydrogen Evolution". *Journal of the American Chemical Society* 137 (2015), pp. 3265–3270. DOI: 10.1021/ja511552k.
- [38] Toshiyuki Abe, Keiji Nagai, Satoko Kabutomori, Masao Kaneko, Akio Tajiri, and Takayoshi Norimatsu. "An Organic Photoelectrode Working in the Water Phase: Visible-Light-Induced Dioxygen Evolution by a Perylene Derivative/Cobalt Phthalocyanine Bilayer". *Angewandte Chemie International Edition* 45 (2006), pp. 2778–2781. DOI: 10.1002/anie.200504454.
- [39] John R. Swierk, D. Méndez-Hernández Dalvin, Nicholas S. McCool, Paul Liddell, Yuichi Terazono, Ian Pakk, John J. Tomlin, Nolan V. Oster, Thomas A. Moore, Ana L. Moore, Devens Gust, and Thomas E. Mallouk. "Metal-free Organic Sensitizers for Use in Water-splitting Dye-sensitized Photoelectrochemical Cells". *Proceedings of the National Academy of Sciences of the United States of America* 112(6) (2015), pp. 1681–1686. DOI: 10.1073/pnas.1414901112.
- [40] Ze Yu, Fei Li, and Licheng Sun. "Recent Advances in Dye-sensitized Photoelectrochemical Cells for Solar Hydrogen Production Based on Molecular Components". *Energy & Environmental Science* 8 (3 2015), pp. 760–775. DOI: 10.1039/C4EE03565H.
- [41] W. Justin Youngblood, Seung-Hyun Anna Lee, Yoji Kobayashi, Emil A. Hernandez-Pagan, Paul G. Hoertz, Thomas A. Moore, Ana L. Moore, Devens Gust, and Thomas E. Mallouk. "Photoassisted Overall Water Splitting in a Visible Light-Absorbing Dye-Sensitized Photoelectrochemical Cell". *Journal of the American Chemical Society* 131 (2009), pp. 926–927. DOI: 10.1021/ja809108y.
- [42] Joel T. Kirner, Jordan J. Stracke, Brian A. Gregg, and Richard G. Finke. "Visible-Light-Assisted Photoelectrochemical Water Oxidation by Thin Films of a Phosphonate-Functionalized Perylene Diimide Plus CoOx Cocatalyst". *ACS Applied Materials & Interfaces* 6 (2014), pp. 13367–13377. DOI: 10.1021/am405598w.
- [43] Ranbir Singh, Ester Giussani, Marta M. Mróz, Fabio Di Fonzo, Daniele Fazzi, Juan Cabanillas-González, Luke Oldridge, Naoum Vaenas, Athanassios G. Kontos, Polycarpus Falaras, Andrew C. Grimsdale, Josemon Jacob, Klaus Müllen, and Panagiotis E. Keivani-dis. "On the Role of Aggregation Effects in the Performance of Perylene-diimide Based Solar Cells". *Organic Electronics* 15 (2014), pp. 1347–1361. DOI: 10.1016/j.orgel.2014.03.044.



## **Experimental Part II**



## 2 Optical and Physical Characterization

Experimental methods used to characterize the optical and physical properties of photoelectrodes produced during this work are explained in this chapter. Material and experimental instruments information are gathered at the end of this chapter, section 2.7 page 28. Experimental conditions will be found directly in their respective chapter.

Part of this chapter have been adapted from:

Pauline Borno, Fatwa F. Abdi, S. David Tilley, Bernard Dam, Roel van de Krol, Michael Grätzel, and Kevin Sivula. “A Bismuth Vanadate-Cuprous Oxide Tandem Cell for Overall Solar Water Splitting”. *The Journal of Physical Chemistry C* 118 (2014), pp. 16959–16966. DOI: 10.1021/jp500441h

Pauline Borno, Mathieu S. Prévot, Xiaoyun Yu, Néstor Guijarro, and Kevin Sivula. “Direct Light-Driven Water Oxidation by a Ladder-Type Conjugated Polymer Photoanode”. *Journal of the American Chemical Society* 137 (2015), pp. 15338–15341. DOI: 10.1021/jacs.5b05724

## 2.1 Absorption of Light

Information about light interaction with a material can be obtained with a Ultraviolet-visible Light (UV-vis) spectroscopic measurement. Light is formed by photons with different energies defined by photon energy,  $h\nu$  in electronvolt (eV), or with wavelength,  $\lambda$  in nanometer (nm). Both are related with equation b.1 where  $c$  is the speed of light in vacuum:  $3 \times 10^8 \text{ m} \cdot \text{s}^{-1}$ ,  $h$  the Plank constant:  $6.63 \times 10^{-34} \text{ J} \cdot \text{s}$  and  $e$  the elementary charge:  $1.60 \times 10^{-19} \text{ C}$ .

$$\lambda = \frac{c \cdot h}{h\nu \cdot e} \quad (\text{b.1})$$

For instance, the light produced by the sun and transmitted to the Earth (filtered by earth atmosphere) corresponds to the AM1.5G spectrum given in figure 2.1. It shows that the Earth receives mostly photons with energy between 250 nm and 1500 nm.

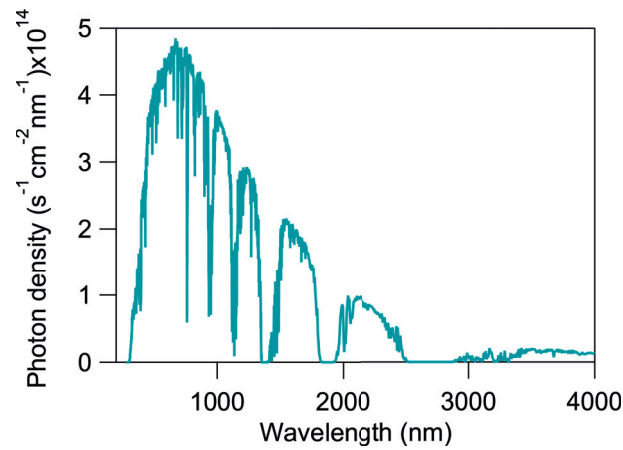


Figure 2.1 – AM1.5G spectrum.

Depending on the energetics of the material, it will interact differently with photons with a defined energy. After interaction light can be:

**absorbed:** transformed inside the material to another type of energy;

**reflected:** returned before entering the material (interaction at the surface of the material);

**transmitted:** returned after interaction with the material.

The latter two effects can be accompanied by diffusion. All interactions are summarized in figure 2.2 where:  $I_0$  is the incident light,  $I_{Rd}$  is the diffuse reflection,  $I_{RS}$  is the specular reflection,  $I_A$  is the absorbed light,  $I_S$  is the refracted light and  $I_T$  is the transmitted light.

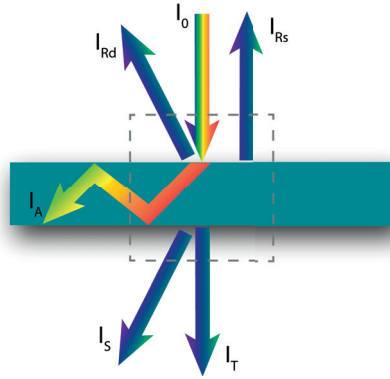


**Figure 2.2** – Schematic description of light-matter interaction.

A balance on the dotted element gives the general following equation:

$$I_0 = I_A + I_T + I_{Rs} + I_{Rd} + I_S \quad (\text{b.2})$$

During a UV-vis measurement, the intensity of a probing light (defined as 100 %) and is compared to the measured light. Depending on the position of the sample and the measured light, it is possible to obtain either the transmittance,  $T$ , in transmission mode :

$$T = \frac{I_T}{I_0} + \frac{I_S}{I_0} \quad (\text{b.3})$$

or the reflectance,  $R$ , in diffuse reflectance mode:

$$R = \frac{I_{Rd}}{I_0} + \frac{I_{Rs}}{I_0} \quad (\text{b.4})$$

With these two measurements, absorptance,  $A_{\%}$ , which is the efficiency of a material to absorb light at a given wavelength (in %) can be calculated by equation b.5\*:

$$A_{\%} = I_0 - T - R \quad (\text{b.5})$$

Sometimes, absorptance is converted to absorbance ( $A$ ) with equation b.6 which is a dimensionless number.

$$A = -\log_{10} (1 - A_{\%}) \quad (\text{b.6})$$

Finally, this absorbance can be normalized to the path length of light giving the absorption coefficient ( $\alpha$ , in  $\text{cm}^{-1}$ ). This value represents how far the light can penetrate the material before being absorbed.  $\alpha$  can be calculated with equation b.7 where  $A$  is the absorbance and  $l$

---

\*with  $I_0 = 100\%$

the material thickness in centimeter (in cm).

$$\alpha = \frac{\ln(10) \cdot A}{l} \quad (\text{b.7})$$

Light interaction with a material can give essential information in the case of semiconductors. In an ideal case, a semiconductor under illumination should absorb light only with energy higher than its band gap. The absorption coefficient then should obey the Tauc relation, see equation b.8 where  $\alpha$  is the absorption coefficient,  $h\nu$  is the incident photon energy in (eV),  $E_g^{\text{opt}}$  is the optical band gap in (eV) and  $n$  is a parameter which takes a value depending on the nature of the transition<sup>†</sup>.

$$(\alpha h\nu)^n \propto (h\nu - E_g^{\text{opt}}) \quad (\text{b.8})$$

Therefore it is possible to determine energetics of a semiconductor from its absorption properties. A semiconductor with an optical band gap of 1.8 eV will absorb photons with energies higher than 1.8 eV, or lower than 689 nm.

## 2.2 Film Morphology

The morphology, i.e. the film structure, is defined by the preparation method, the material itself and the substrate (or underlayer) morphology. For instance, solubilized polymer tends to produce very smooth film, while small particles in suspension will create films of high roughness.

The easiest way to analyze morphology is by microscopy techniques. Depending on length scale of morphological features, different types of microscopy are used such as: optical microscopy (from centimeter scale to micrometer scale) or electron microscopy (from micrometer scale to nanometer scale).

Both rely on interaction of a probe, visible light for an optical microscope or an electron beam for an electron microscope, on a sample. In the case of optical microscopy, the visible light will either be transmitted through the sample or blocked. The remaining light is magnified by lenses and can be detected visually. In the case of an electron microscope, the electron beam will excite the sample which will reemit some electrons which can be collected to form the picture.

The Scanning Electron Microscopy (SEM) will scan the sample with an electron beam and detects the secondary electrons produced at each position to form the picture. In a Transmission Electron Microscopy (TEM) transmitted electrons are collected to form the picture.

---

<sup>†</sup>  $n = 2$  for a direct transition, or  $n = 1/2$  for an indirect transition



## 2.3 Raman Spectroscopy

Raman spectroscopy is a technique which determines vibrational and rotational modes of a sample. As said, once absorbed, light transmits its energy to the material. It can be used to excite an electron from the valence band to the conduction band but also excite an electron from a vibrational or rotational state to another. The difference between the energy of an incident laser, used to probe the material, and the diffused light from the sample, i.e. after interaction, will correspond to the unique vibrational and rotational modes of the material.

During a Raman spectroscopy measurement, a monochromatic laser is used to probe the material. If it can excite the material, part of its energy will be transmitted resulting in a laser with shifted energy. This shift,  $\delta w$  in ( $\text{cm}^{-1}$ ), can be measured by comparison between the energy of the probe,  $\lambda_0$  in nanometer (nm), and energy of the resulting light,  $\lambda_1$  in nanometer (nm), with equation b.9.

$$\delta w = \frac{1}{\lambda_0} - \frac{1}{\lambda_1} \quad (\text{b.9})$$

## 2.4 Contact Angle

Information about liquid interaction with a material can be obtained with a contact angle measurement. Depending on chemical entities present at the surface of the material, it can be hydrophilic, i.e. with high affinity with water, or hydrophobic, i.e. with low affinity with water.

To quantify this affinity, which can interfere on crucial events occurring at the SCLJ, the wettability of the semiconductor by water is measured.



**Figure 2.3** – Contact angle between a) a hydrophobic surface and water and b) a hydrophilic surface and water.

During a contact angle measurement, a drop of liquid, water in our case, is deposited at the sample surface. A thermodynamic equilibrium is reached between the gas-liquid, liquid-solid and solid-gas interface. Each of them are controlled by an interfacial energy, in the form of a force parallel to the surface. The shape of the drop will be defined by the position of the solid-liquid-gas interface on which the total force is given by equation b.10 where  $\gamma_{SG}$ ,  $\gamma_{LS}$ ,  $\gamma_{GL}$  are the interfacial energy at the solid-gas, liquid-solid and gas-liquid interface respectively

and  $\vartheta$  the contact angle between the  $\gamma_{LS}$  and  $\gamma_{GL}$  forces.

$$\gamma_{SG} - \gamma_{LS} - \gamma_{GL} \cos \vartheta = 0 \quad (\text{b.10})$$

A contact angle between  $45^\circ$  and  $90^\circ$  will represent an hydrophobic surface (figure 2.3 a)) while a contact angle between  $0^\circ$  and  $45^\circ$  will represent an hydrophilic surface (figure 2.3 b)).

Contact angle can simply be determined from a picture of the drop. By mathematical fitting of the drop shape, the angle can be determined.

### 2.5 Gas Chromatography

Gas chromatography was used to detect the presence and quantify the amount of evolved gas during the PEC measurement. In a gas chromatograph, a mobile phase is used to carry the gaseous compound to analyze through a stationary phase contained in a column. The retention time, the time for the component to go through the column, depends on the interactions between the compound and the stationary phase. A compound that has a high interaction with the stationary phase will have a long retention time. Hence it is possible to separate chemical from a mixture. At the end of the column, a detector will detect the presence or absence of a compound. As  $\text{H}_2$  and  $\text{O}_2$  are our main compounds to detect, a plasma emission detector is used.

### 2.6 Photoluminescence Spectroscopy

During a photoluminescence spectroscopy experiment, the photoluminescence of a chemical compound, or a material, is detected. Absorption of a photon results in excitation of an electron. This one can lose its energy during recombination by emission of another photon. Energy of the absorbed and emitted photons are dependent on the compound energetic and are therefore unique.

This technique can be used to quantify recombination in a material or in our case to detect a chemical compound.

### 2.7 Experimental instruments

#### 2.7.1 Materials

For the preparations of thin films as explained in chapter 5 page 67, the following materials were used as received:

- Poly(benzimidazobenzophenanthroline) (BBL) used for this work was supplied by Sigma-Aldrich, and was reported to have an intrinsic viscosity,  $[\eta] = 0.58 \pm 0.04 \text{ dL} \cdot \text{g}^{-1}$

(using Huggins relation), in concentrated sulfuric acid at 25 °C;

- Methanesulfonic Acid (MSA) (Sigma-Aldrich,  $\geq 99.5\%$ );
- Igepal® co-520 (Sigma-Aldrich, 99 +%, ACS reagent);
- $\text{HNO}_3$  (VWR, Normapur, AnalaR, 65 %);
- $\text{NH}_3$  (VWR, Normapur, AnalaR, 25 %);
- $\text{H}_2\text{O}_2$  (Reactolab SA, Pharma, 30 %);
- $\text{NiSO}_4 \cdot 6\text{H}_2\text{O}$  (Sigma-Aldrich, 99.99 +%);
- $\text{Co}(\text{NO}_3)_2 \cdot 6\text{H}_2\text{O}$  (Strem Chemicals INC, 99 %).

Employed substrate were either:

- Fluorine-doped tin oxide coated float glass substrates (FTO, Solaronix), washed by acetone, ethanol and treated with a nitrogen plasma in a Harrick plasma cleaner before use;
- 4.95 MHz At-cut Au-plated crystal ( $0.785\text{ cm}^2$  contact area, Q-sense, QSX 301), cleaned in a solution containing 5:1:1  $\text{H}_2\text{O}/\text{NH}_3/\text{H}_2\text{O}_2$  at 75 °C during 5 minutes, washed with Milli-Q water, dried under Argon flow and finally cleaned by Ozone plasma.

For their optical and physical characterization, the following materials were used as received:

- Coumarin (Merck, for synthesis,  $\geq 99\%$ );
- Umbelliferone (Acros organics, 99 %);

### 2.7.2 Instruments

To prepare the films, a WS-650MZ-23NPP (Laurell) spin-coater and a ZR-4200 (Qualtech Products Industry) dip coater were used.

Total reflectance and transmittance spectrum of BBL sprayed films were measured under illumination from the substrate side with a Shimadzu UV-3600 UV-vis-NIR spectrophotometer (Shimadzu Co.) using an integrating sphere.

Optical microscopic images were obtained with a Nikon H550L.

SEM pictures were taken with a high resolution Zeiss Merlin XLF-30 microscope.

Raman spectra were recorded using a LabRam Hr Raman spectrometer (Jobin Yvon Horiba) with 532 nm laser.

## Chapter 2. Optical and Physical Characterization

Photoluminescence spectra were measured with a Perkin Elmer LS50B Luminescence spectrometer.

Contact angle measurement were measured with a Krüss DSA 100 Drop shape analyser.

A gas chromatograph Clarus 480 (Perkin Elmer) equipped with a molecular sieve (of 5 Å) column at 50 °C was used for oxygen detection with a plasma emission detector (PlasmaDeteck).

Illumination was performed under simulated solar illumination (1 sun,  $100 \text{ mW} \cdot \text{cm}^{-2}$ ) produced by a 450 W Muller Elektronik Xenon-arc lamp (Müller-Electronik) using appropriate filters and calibrated using a Si photodiode. Lamp spectrum was recorded with an OceanOptics USB2000+XR1 ES spectrometer with a Spectralon cosine corrector. The illuminated area was  $0.283 \text{ cm}^2$  for back window.

### 2.7.3 Calibration of Solar Simulator

Light was calibrated using the following procedure.

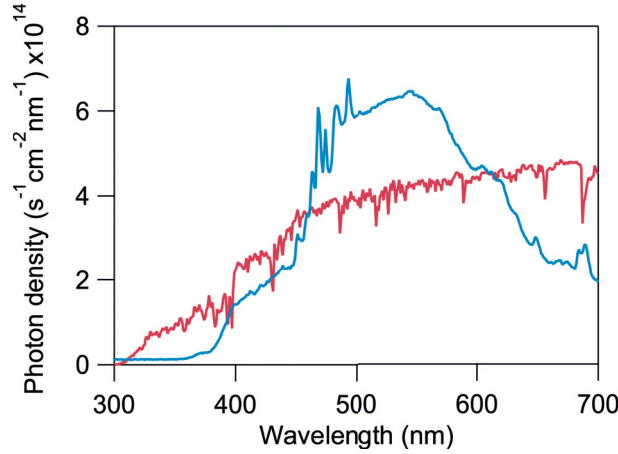


Figure 2.4 – AM 1.5 spectrum (red) and Xenon arc lamp spectrum (blue).

The AM1.5 spectrum was first integrated between 300 nm and 700 nm<sup>‡</sup> to obtain the photon density:  $\Phi_{AM1.5}$  in  $(\text{s}^{-1} \cdot \text{cm}^{-2})$  which is the total amount of photon that should be provided by the lamp to have a 1 sun illumination ( $100 \text{ mW} \cdot \text{cm}^{-2}$ ). Then the lamp spectrum was also integrated between the same boundaries to obtain the photon density of the lamp:  $\Phi_{Xe \text{ lamp}}$  in  $(\text{s}^{-1} \cdot \text{cm}^{-2})$ . These two calculated values should be equal therefore the factor between them,  $m$ , is calculated using equation b.11 and finally the calibrated lamp spectrum,  $\Phi_{Xe \text{ lamp cal}}$  in  $(\text{s}^{-1} \cdot \text{cm}^{-2})$  is determined with equation b.12.

$$m = \frac{\Phi_{AM1.5}}{\Phi_{Xe \text{ lamp}}} \quad (\text{b.11})$$

<sup>‡</sup>700 nm being the band gap of our material

$$\Phi_{Xe\ lamp\ cal} = m \cdot \Phi_{Xe\ lamp} \quad (b.12)$$

These two spectrums are compared in figure 2.4. Each of them gives the same photon density (same integrated value).

In order to measure the photon density of the lamp, a Silicon photodiode was used. The electron density, or current density, measured by the diode is given by equation b.13 where  $IPCE(\lambda)$  is the the number of electrons extracted by the diode per photon of a given wavelength, see figure 2.5,  $\Phi_{Xe\ lamp\ cal}$  is the calibrated Xe lamp spectrum calculated previously and  $e$  the elementary charge. The cell was finally positioned where the diode measure the calculated current.

$$J = \int_{300}^{700} (IPCE(\lambda) \cdot \Phi_{Xe\ lamp\ cal}(\lambda) \cdot e) d\lambda \quad (b.13)$$

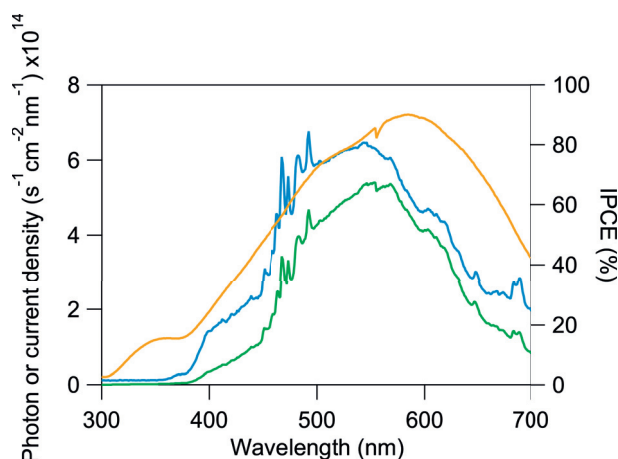


**Figure 2.5** – IPCE (yellow) and current density (green) of diode with calibrated lamp spectrum (blue).

## References

- [1] Pauline Bornoz, Fatwa F. Abdi, S. David Tilley, Bernard Dam, Roel van de Krol, Michael Grätzel, and Kevin Sivula. “A Bismuth Vanadate-Cuprous Oxide Tandem Cell for Overall Solar Water Splitting”. *The Journal of Physical Chemistry C* 118 (2014), pp. 16959–16966. DOI: 10.1021/jp500441h.
- [2] Pauline Bornoz, Mathieu S. Prévot, Xiaoyun Yu, Néstor Guijarro, and Kevin Sivula. “Direct Light-Driven Water Oxidation by a Ladder-Type Conjugated Polymer Photoanode”. *Journal of the American Chemical Society* 137 (2015), pp. 15338–15341. DOI: 10.1021/jacs.5b05724.



## 3 Electrochemical Characterization

Experimental methods applied to characterize the electrochemical properties of photoelectrodes produced during this work are detailed in this chapter. Material and experimental instruments information are gathered at the end of this chapter, section 3.6 page 45. Experimental conditions of measurements will be found directly in their respective chapter.

Parts of this chapter have been adapted from:

Pauline Bornoz, Fatwa F. Abdi, S. David Tilley, Bernard Dam, Roel van de Krol, Michael Grätzel, and Kevin Sivula. “A Bismuth Vanadate-Cuprous Oxide Tandem Cell for Overall Solar Water Splitting”. *The Journal of Physical Chemistry C* 118 (2014), pp. 16959–16966. DOI: 10.1021/jp500441h

Pauline Bornoz, Mathieu S. Prévot, Xiaoyun Yu, Néstor Guijarro, and Kevin Sivula. “Direct Light-Driven Water Oxidation by a Ladder-Type Conjugated Polymer Photoanode”. *Journal of the American Chemical Society* 137 (2015), pp. 15338–15341. DOI: 10.1021/jacs.5b05724

### 3.1 Electrochemical Reactions

During an electrochemical experiment,<sup>3,4</sup> the following reaction occurs:



where Ox and Red are chemical compounds\* and  $e^-$  is a free electron.

Therefore, through the exchange of electrons, a compound can either be reduced by a gain of electron(s) or oxidized by a release of electron(s). This exchange reaction of electrons happens at an interface where an electrode (a solid phase) and an electrolyte (a liquid phase) are in contact.

In the case of non-spontaneous reaction, it can only happen if energy is provided to the system, either to drive an electron into the electrolyte for the reduction reaction to occur or to drive an electron into the electrode for the oxidation reaction to occur. This amount of energy is defined as the reduction potential  $E_{Ox/Red}$  or oxidation potential  $E_{Red/Ox}$ , it is unique for each Ox/Red couple and is given in Volt (V). It is then possible to force a reaction by providing this energy and measure its occurrence by the detection of electrons movement or the detection of concentration change of chemical species.

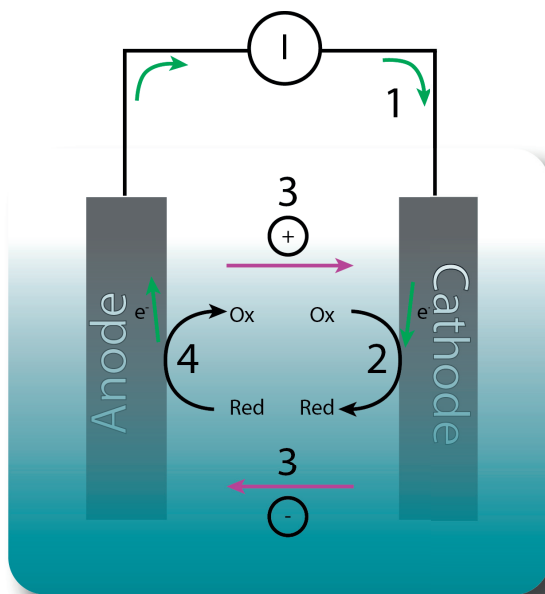


**Figure 3.1** – Schematic representation of an electrochemical cell.

The goal is then to move these charges through a closed electrical circuit composed of a minimum of two electrodes and an electrolyte. This configuration is called an electrochemical

\* Ox is an oxidized species and Red a reduced one



cell, see figure 3.1, where the flow of charges, i.e. electrical current, is directed by:

1. charge transport: movement of electrons through the circuit and electrode until the interface;
2. charge extraction (or charge transfer) following equation c.1;
3. charge transport inside the electrolyte with movement of chemical species;
4. charge extraction (insertion) at the second interface.

In order to have a closed circuit, they are necessarily two reactions happening, called the two half-reactions. One will be the reduction at the cathode and the other one will be the oxidation at the anode. However, we usually want to study only one reaction. The trick is then to fix one half reaction by using a specific electrode where a known and stable reaction is happening. In this case, this electrode is called the counter electrode and the one under study is the working electrode. As charges are moving, the reaction at the counter electrode (CE) should not change and all variations can be attributed to the working electrode (WE).

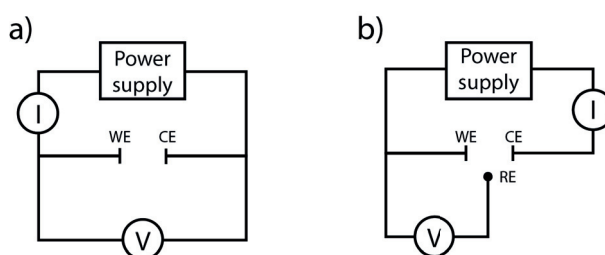


**Figure 3.2** – Schematic representation of a) a two-electrodes cell configuration and b) a three-electrodes cell configuration where WE is the working electrode, RE the reference electrode and CE the counter electrode.

This simple two-electrode configuration as described above is usually not used because, as current flows at the counter electrode, its material will vary which will affect its potential. Therefore the system is no longer stable. Instead, a three-electrode configuration is used where the current flows between the working and the counter electrode (CE) and their potential is measured with respect to a reference electrode (RE), see figure 3.2. In this case the counter electrode is chosen so that the current won't be limited by this side of the cell. We usually use platinum where the HER (when testing an oxidation reaction at the working electrode) can happen easily. For the same reason, care should be taken that its contact area with the electrolyte should be bigger than the contact area of the working electrode, by using a twisted wire or a mesh.

The flow of electrons is defined as the current  $I$ , i.e. the number of electrons per unit of time given in Ampere (A). Sometimes to normalize the value, the flux of electrons is given as the current density,  $J$  i.e. the number of electron per unit of time and surface in  $(A \cdot cm^{-2})$ . The

### Chapter 3. Electrochemical Characterization

---

potential  $E$  is defined as the energy needed to drive charges between the two electrodes given in Volt (V). It is only possible to apply a potential with respect to an other bound (between two electrodes) therefore potential is a lighter way to refer to "difference of potential" ( $\Delta E$ ).

The potential is therefore reported versus a standardized reference electrode. The more common ones, and used in this work, are the Normal Hydrogen Electrode (NHE), where potential of the hydrogen evolution reaction in a 1 N acid solution is fixed at 0 V (equivalent to the theoretical Standard Hydrogen Electrode (SHE)<sup>†</sup>) and the Reversible Hydrogen Electrode (RHE), where the potential of hydrogen evolution is also fixed at 0 V but the scale changes with the pH of electrolyte, see equation c.2 where  $E_{Re,RHE}$  is the potential of the RHE reference.

$$E_{Re,RHE} = 0.000 - 0.059 \cdot pH \quad (c.2)$$

These are theoretical references electrodes, in practice we use an Ag/AgCl (KCl sat.) reference electrode which potential is calibrated with  $E_{Ag/AgCl(KCl\ sat.)}^0$  (or  $E_{ref}^0$  in the general case). The potential is then reported with respect to the RHE or NHE potential, and can be calculated with the equations c.3 and c.4 where  $E_{RHE}$  is the potential with respect to (versus) the RHE reference,  $E_{ref}$  is the potential measured versus the used reference electrode and  $E_{NHE}$  is the potential with respect to (versus) the NHE reference.

$$E_{RHE} = E_{ref} + E_{ref}^0 + 0.059 \cdot pH \quad (c.3)$$

$$E_{NHE} = E_{ref} + E_{ref}^0 \quad (c.4)$$

In some cases a pseudo reference electrode can be used. Compared to a real reference electrode, this one will lack of thermodynamic equilibrium. For instance the Ag/AgCl (KCl sat.) reference electrode is made of a silver wire coated with a silver chloride layer in contact with a saturated KCl solution isolated from the electrolyte. In this case the reactions happening at the reference electrode are the following:



In the overall reaction defined by c.7, all chemical compounds are in sufficient amount so that a true equilibrium is reached, i.e. there is no change in their concentration.



However, in a pseudo reference electrode like a silver wire alone, only reaction c.5 will be possible. Silver cation will leak from the wire and diffuse into the electrolyte. This instability of cation concentration will force the reaction toward AgCl production and no equilibrium will be reached.

---

<sup>†</sup> in which  $H^+$  ions are assumed to have no interactions with each others

The last critical point in an electrochemical cell is the electrolyte. It needs to be conducting enough to not be limiting. For that we use ions in large concentrations. Depending on the reaction under study, they can be inert, not reacting in the potential range under study, or reacting. We will call a hole scavenger an ion that can be oxidized easily. Electrolyte pH can also influence the potential of reactions, it can be adjusted using acids or bases or fixed using a buffer.

## 3.2 Potentiostatic Methods

In this type of measurement, the potentiostat will control the potential between the counter and the working electrode so that the potential between the working and the reference electrodes corresponds to the desired value.

For an n-type semiconductor in the dark, four conditions may occur:

- At equilibrium, represented in figure 3.3, no potential is applied between the working electrode (the semiconductor) and the counter electrode.

An equilibrium is reached between the Fermi level of the semiconductor, the energy of electrons in the electrolyte and the Fermi level of the counter electrode. A space charge is formed in the semiconductor at its interface with the electrolyte. Due to this dynamic equilibrium, no net current is measured between the working and counter electrodes;

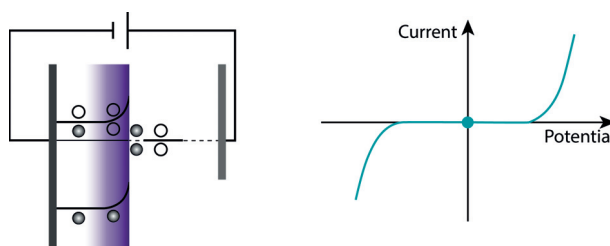


**Figure 3.3** – n-type semiconductor at equilibrium and its corresponding position (green circle) in the current-potential curve.

- if a negative bias is applied to the working electrode, the energy of electrons is raised, raising the Fermi level of the semiconductor and filling its conduction band with electrons.

Until the flat-band condition, corresponding to an applied potential of  $E_{fb}$ , represented figure 3.4, no net current is flowing as the energetic barriers of the space charge layer blocks the electrons inside the semiconductor;

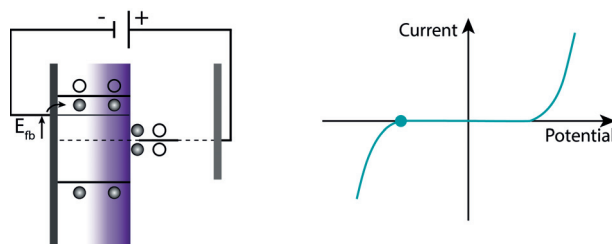


**Figure 3.4** – n-type semiconductor under flat-band condition and its corresponding position (green circle) in the current-potential curve.

- if a negative bias higher than  $E_{fb}$  is applied, then energetics in the space charge region are favorable for electrons to flow to the electrolyte. This is called the accumulation region as electrons are accumulated at the semiconductor surface.

If an electrochemical reaction can happen in the electrolyte then this will result in a net reduction current, represented in figure 3.5;

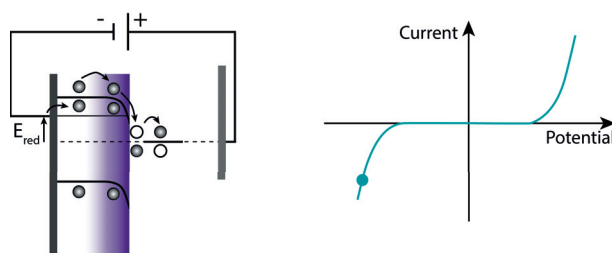


**Figure 3.5** – n-type semiconductor under negative bias and its corresponding position (green circle) in the current-potential curve.

- if a positive bias is applied to the working electrode, the energy of electrons in the semiconductor is lowered, lowering the Fermi level and emptying the valence band.

Due to the space charge region, energetics are not favorable for electrons to flow from the electrolyte to the semiconductor. However, a very high positive bias will result in a very thin space charge region and electrons from the electrolyte could move to the semiconductor through tunneling. This will result in a net oxidation current, represented figure 3.6.

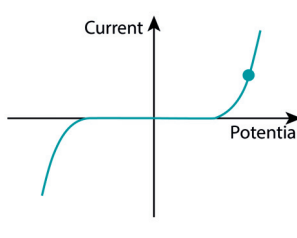


**Figure 3.6** – n-type semiconductor under positive bias and its corresponding position (green circle) in the current-potential curve.

In a non-ideal case where no electrochemical reaction is possible in the electrolyte, filling or emptying the working electrode with electrons could lead to its oxidation or reduction. This effect will also lead to an oxidation or reduction current.

Performance of a photoanode or photocathode for PEC water splitting are determined by variation of the potential and measurement of the resulting current. The results are compared for the photoelectrode in the dark, as explained above, or under illumination, process explained in part 1.3. Their characteristics are defined by:

**Dark current:** the current extracted from the working electrode without illumination and under applied potential.

**Photocurrent:** the current extracted from the working electrode while illuminated and under applied potential. For a photoanode, the difference between the photocurrent and the dark current at  $1.23 V_{\text{RHE}}$  is defined as the effective current produced under illumination for OER. Assuming a constant, non-zero, Faradaic efficiency, the higher the photocurrent is, the more oxygen will be produced.

**Onset of photocurrent:** the potential at which the working electrode starts producing a photocurrent. The onset of photocurrent depends on the energetics of the semiconductor, i.e. position of the valence band, and its catalytic performance.

**Transient current:** the response in time of the photocurrent while light is turned on or off.

Depending on information needed, different type of potentiostatic-based methods can be used. Potential can be:

- set as constant for a defined period of time. It is called the Chronoamperometry (CA) and is used to determine the stability of the dark current/photocurrent, their amplitude or transient behavior;

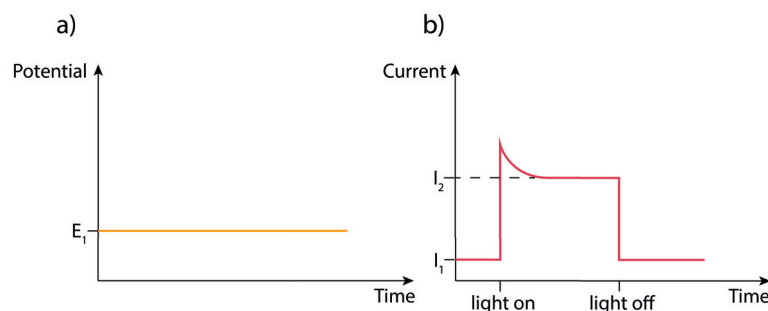


**Figure 3.7** – Chronoamperometry (CA) experiment with a) the potential input and b) the current output in dark and under illumination.

- varied as a linear function of time. It is called the Linear Sweep Voltammetry (LSV) and is used to determine rapidly the position of onset of photocurrent as well as its

amplitude as function of potential. Results of an LSV are referred in the text as a Current density-Voltage (J-V) curve;

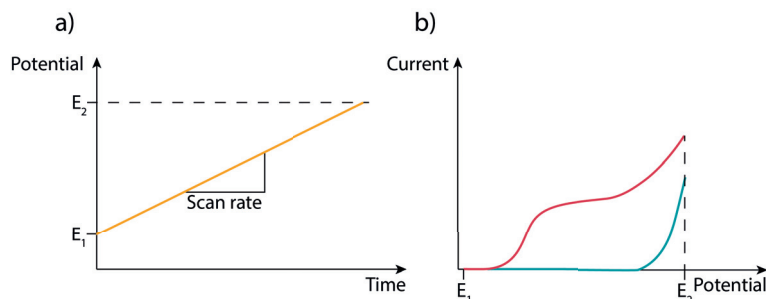


**Figure 3.8** – Linear Sweep Voltammetry (LSV) experiment with a) the potential input and b) the current output in dark (blue) and under illumination (red).

- cycled as a linear function of time between two potentials. It is called the Cyclic Voltammetry (CV) and is used to determine the potential of different reactions occurring at the electrode surface.

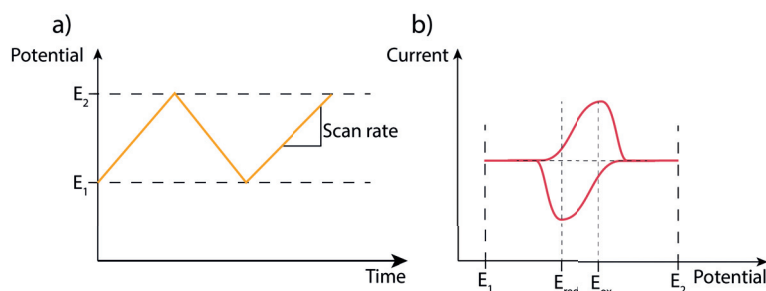


**Figure 3.9** – Cyclic Voltammetry (CV) experiment with a) the potential input and b) the current output.

To directly compare the properties of the electrode in the dark and under illumination, an intermittent illumination can be used.

### 3.3 Frequency Based method

In the case of potentiostatic methods, the measured output is given by the sum of events happening in the electrochemical cell. Even if these events are completely independent and hence can occur at different time scale, there is no possibility to decouple their effects and to study them separately.

In frequency based method, the applied input is frequency-dependent therefore it will be possible to probe different events depending on their time scale. During an Electrochemical Impedance Spectroscopy (EIS)<sup>3,5</sup> experiment, a sinusoidal potential perturbation in the form of equation c.8 is applied to the system where  $|E|$  is the amplitude of the potential in (V),  $\omega$

the frequency in (s) and  $t$  the time in (s). The response of the system will be in the form of a sinusoidal current as equation c.9 where  $|I|$  is the amplitude of current in (A) and  $\phi$  the phase shift in (s). The phase shift is defined as the delay between the input and output.

$$\Delta E = |E| \sin(\omega t) \quad (c.8)$$

$$\Delta I = |I| \sin(\omega t - \phi) \quad (c.9)$$

Figure 3.10 shows both waves in a phasor diagram where they can be considered either as a rotating vector with the same angular frequency ( $\omega$ )(left) or a sinusoidal wave (right). The wave (or measured quantity) correspond to the projection of the rotating vector on the y axis.

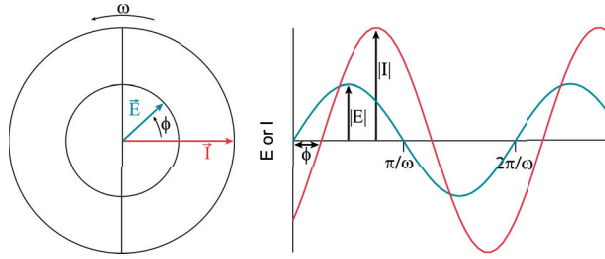


**Figure 3.10** – Phasor diagram of potential and current waves during an EIS measurement with the potential wave (blue) and the current wave (red).

Before introducing impedance, we need to define some complex number nomenclature. In a complex plan, the y axis is called the imaginary part ( $Im$ ) and the x axis the real part ( $Re$ ). In this plan a vector is defined as in equation c.10 with  $R'$  the projection on the  $Re$  axis and  $R''$  the projection on  $Im$  axis, giving equation c.11. A vector is defined by its length, the modulus  $|R|$ , and its angle, the argument  $\varphi$ .

$$\vec{R} = Re(R) + i \cdot Im(R) = R' + i \cdot R'' \quad (c.10)$$

$$\vec{R} = |R| \cos(\varphi) + i |R| \sin(\varphi) \quad (c.11)$$

Complex number, or vector, can also be written using Euler's relation:

$$\vec{R} = |R| \cos(\varphi) + i |R| \sin(\varphi) = |R| e^{i \cdot \varphi} \quad (c.12)$$

Therefore our potential and current vectors can be reformulated as the following equations:

$$\vec{E} = |E| \cos(\omega t) + i |E| \sin(\omega t) = |E| [\cos(\omega t) + i \cdot \sin(\omega t)] \quad (c.13)$$

$$\vec{I} = |I| \cos(\omega t - \phi) + i |I| \sin(\omega t - \phi) = |I| [\cos(\omega t - \phi) + i \cdot \sin(\omega t - \phi)] \quad (c.14)$$

### Chapter 3. Electrochemical Characterization

---

To simplify the notation, we will use Euler's notation:

$$\vec{E} = |E| e^{i \cdot \omega t} \quad (\text{c.15})$$

$$\vec{I} = |I| e^{i \cdot \omega t - \phi} \quad (\text{c.16})$$

The impedance is defined as the effective resistance which from Ohm's law can be written as equation c.17 with R the resistance in ( $\Omega$ ), E the potential in (V) and I the current in (A). To get the impedance we then need to express the ratio of our  $\vec{E}$  and  $\vec{I}$  vectors given by equation c.18.

$$R = \frac{E}{I} \quad (\text{c.17})$$

$$\vec{Z} = \frac{\vec{E}}{\vec{I}} = \frac{|E|}{|I|} \frac{e^{i \cdot \omega t}}{e^{i \cdot \omega t - \phi}} = \frac{|E|}{|I|} e^{i \cdot \phi} \quad (\text{c.18})$$

This impedance  $\vec{Z}$  is a new vector which has a modulus of  $\frac{|E|}{|I|}$  and an argument of  $\phi$  which are two measurable values.

This resulting vector can be plotted in the Nyquist plot where  $\text{Re}(Z)$  and  $-\text{Im}(Z)$  are the x and z axis respectively or the Bode plot where  $|Z|$  and  $\phi$  are directly plotted as a function of  $\omega$ .

In order to discuss results of EIS, it is helpful to have in mind these two simple cases:

If the system behaves like a pure resistance, where the current is only limited by a low conductivity, from Ohm's law the current will be the  $\vec{E}$  vector divided by R a resistance, see equation c.19. The current will then be proportional and in phase ( $\phi = 0$ ) with the potential.

$$\vec{I} = \frac{\vec{E}}{R} \quad (\text{c.19})$$

$$\vec{Z} = \frac{\vec{E}}{\vec{I}} = \frac{\vec{E} \cdot R}{\vec{E}} = R \quad (\text{c.20})$$

The resulting impedance will be a constant, equation c.20, only defined with a real part and independent of  $\omega$  and therefore will appear as a point in the  $\text{Re}(Z)$  axis in the Nyquist plot.

If the system behaves like a pure capacitance, where the current is stored inside the system, its charge q in Coulomb (C) is defined with equation c.21 where C is the capacitance in Farad (F). Knowing that the current is derivative of the charge with respect to time, the current can be rewritten as equation c.22.

$$q = C \cdot E \quad (\text{c.21})$$

$$\vec{I} = \frac{d(C \cdot \vec{E})}{dt} = C |E| \frac{d e^{i \cdot \omega t}}{dt} = C |E| i \cdot \omega e^{i \cdot \omega t} \quad (\text{c.22})$$

The resulting impedance, equation c.23, will be a purely imaginary number and dependent on



the frequency. In a Nyquist plot it will appear as a line on the  $-\text{Im}(Z)$  axis. We can also say that a pure capacitance has a delay of  $\pi/2$  with the potential.

$$\vec{Z} = \frac{\vec{E}}{\vec{I}} = \frac{|E| t e^{i \cdot \omega t}}{C \cdot i \cdot \omega |E| e^{i \cdot \omega t}} = \frac{1}{C \cdot i \cdot \omega} \quad (\text{c.23})$$

The goal of impedance is then assimilate the chemical system to a comparable electrical system by testing various frequencies. For each frequency, a point will be obtained in Nyquist and Bode plot and results are given by the frequency evolution of this point on the graph. The idea is then to find a combination of equivalent electrical element, like resistance and capacitance, that will describe the data. This combination is called an equivalent circuit. For example, EIS results of a system which contains a resistance in series with a capacitance, see figure 3.11 can be fitted with equivalent circuit as in inset of figure 3.11.

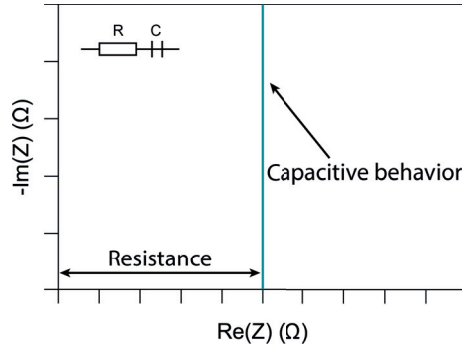


**Figure 3.11** – Example of an equivalent circuit (inset) and its corresponding EIS results.

The difficulty is then to find the appropriate equivalent circuit that will correspond physically to the system and fit the data. If it is the case then it is possible to attribute an equivalent electrical element to each event in the system.

Electrochemical Impedance Spectroscopy (EIS) is usually used to determine the flat-band potential,  $E_{fb}$ , and the majority carrier density,  $N_a$ , with a Mott-Schottky (M-S) analysis. In this case, the capacitance of the space charge layer,  $C_{SC}$ , is determined as a function of the applied potential,  $E$ . Using the Mott-Schottky (M-S) equation c.24 with  $\epsilon_0$  the vacuum permittivity,  $\epsilon_r$  the material dielectric constant,  $e$  the elementary charge and  $E_{SC}$  the potential drop across the space charge region, the flat-band potential can be calculated.

$$\frac{1}{C_{SC}^2} = \frac{2}{\epsilon_0 \epsilon_r N_a e} E_{sc} = \frac{2}{\epsilon_0 \epsilon_r N_a e} (E - E_{fb}) \quad (\text{c.24})$$

### 3.4 Quartz Crystal Microbalance (QCM)

Quartz Crystal Microbalance (QCM) is a technique to measure very small mass variation. It is based on the piezoelectric effect of a quartz sensor which can transform a mechanical stress into an electrical response and vice versa.

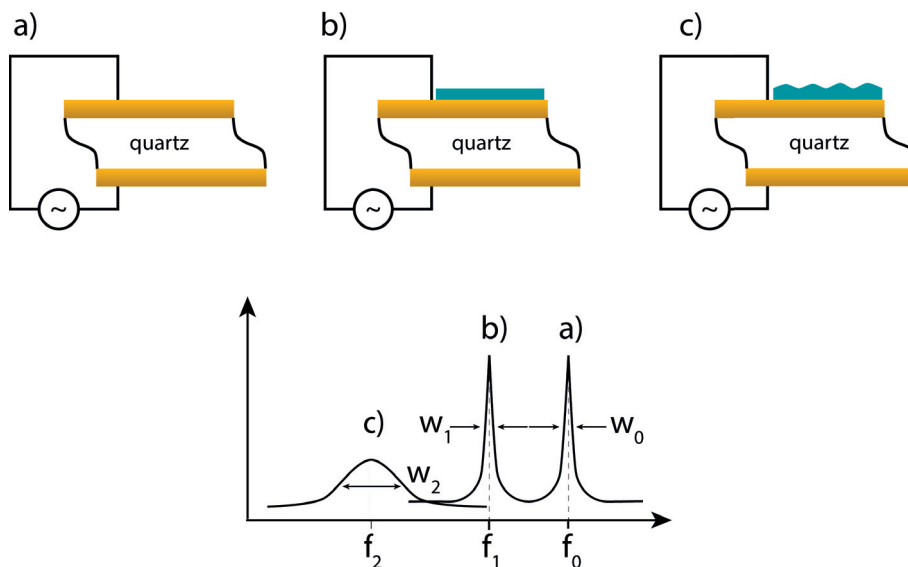


**Figure 3.12** – Schematic description of QCM technique for a) an unloaded sensor, b) a loaded sensor with a rigid layer and c) a loaded sensor with a damping layer.

In this technique, a sensor is put under resonance. Any mechanical stress, a change of mass for example, will result in a shift in the resonance frequency, see figure 3.12 a) and b). Hence it can be used to detect adsorption or desorption of a chemical compound on the sensor. By monitoring this shift in frequency, the change of mass can be calculated with the Sauerbrey equation, equation c.25, with  $\Delta m$  the mass change in (g),  $S_g$  the geometrical surface in ( $\text{cm}^2$ ),  $\Delta f$  the frequency change in (Hz),  $\rho_q$  the density of quartz  $2.648 \text{ g} \cdot \text{cm}^{-3}$ ,  $\mu_q$  the shear modulus of quartz  $2.947 \times 10^{11} \text{ g} \cdot \text{cm}^{-1} \cdot \text{s}^{-2}$ ,  $f_0$  the resonant frequency 4.95 Hz, o the overtone.

$$\frac{\Delta m}{S_g} = -\Delta f \frac{\sqrt{\rho_q \mu_q}}{2 \cdot o \cdot f_0^2} \quad (\text{c.25})$$

This equation is only valid for rigid material. In the case of an elastic material, such as a polymer film see figure 3.12 c), the frequency of the system will be slowed down resulting in a damping of the resonance frequency. Recent instruments now measure the frequency shift as well as the width of the frequency peak, i.e. its damping. A viscoelastic modeling is then necessary to correlate both change with the change of mass.

QCM can be coupled with an electrochemical experiment where the working electrode is the quartz sensor. In this case it is possible to monitor the change of mass during the electrochem-

ical reaction.

## 3.5 Incident Photon-to-current Efficiency (IPCE)

Efficiency of a photoanode/photocathode can also be defined by its Incident Photon-to-current Efficiency (IPCE). Due to recombination of charges in the semiconductor, an absorbed photon does not necessary leads to a photocurrent. The IPCE quantifies the light-to-current conversion by correlating the incident light and the extracted photocurrent. It is defined by equation c.26 where  $N_e(\lambda)$  is the number of extracted electrons,  $N_{ph}(\lambda)$  is the number of incident photon,  $J_{ph}(\lambda)$  the photocurrent in ( $\text{A} \cdot \text{m}^{-2}$ ),  $h\nu$  the photon energy in (J),  $I_0(\lambda)$  the incident light flux in ( $\text{W} \cdot \text{m}^{-2}$ ) and  $e$  the elementary charge.

$$IPCE(\lambda) = \frac{N_e(\lambda)}{N_{ph}(\lambda)} = \frac{J_{ph}(\lambda) \cdot h\nu}{I_0(\lambda) \cdot e} \quad (\text{c.26})$$

During an IPCE experiment, monochromatic light is used to illuminate the photoelectrode, with or without applied bias, and the corresponding current is measured. IPCE spectrum is obtained by variation of the light wavelength. Integration of this spectrum should correspond to the measured photocurrent under white light illumination.

## 3.6 Experimental instruments

### 3.6.1 Materials

The following materials were used as received:

- $\text{KH}_2\text{PO}_4$  (Acros Organics, monobasic, 99 +%, ACS reagent);
- $\text{K}_2\text{HPO}_4$  (Sigma-Aldrich, reagent plus TM,  $\geq 99.0\%$ );
- $\text{NaOH}$  (Reactolab SA, pur pastilles);
- $\text{Na}_2\text{SO}_4$  (Reactolab SA, 96 %, tech.);
- $\text{Co}(\text{NO}_3)_2$  (Alfa Aesar, puratronic, 99.999 %);
- $\text{Na}_2\text{SO}_3$  (Sigma-Aldrich, anhydrous,  $\geq 98\%$ );
- $\text{NaClO}_4$  (ABCR, anhydrous, 98 %);
- $\text{NaTPB}$  (Sigma-Aldrich, ACS reagent,  $\geq 99.5\%$ );
- $\text{HClO}_4$  (VWR International SA, 70 – 72 %);
- $\text{KClO}_4$  (Sigma-Aldrich, ACS reagent, +99 %);

### Chapter 3. Electrochemical Characterization

- $\text{LiClO}_4$  (ABCR, anhydrous (ACS), 95 %);
- TBACl (Acros Organics, tech., 95 %);
- TBAOH (Sigma-Aldrich, 20 wt. % in  $\text{H}_2\text{O}$ );
- $\text{TBAClO}_4$  (TCI,  $\geq 98.0\%$ ).
- Acetonitrile (Macron fine chemical, ChromPR HPLC) was dried with molecular sieves (Sigma-Aldrich, 4 Å, 8-12 mesh).

Electrolytes used are listed in the two following tables.

Name	Concentration	Compound	Solvent	pH	adjusted with
Buffered	0.5 M	$\text{Na}_2\text{SO}_4$	Milli-Q water	2-10	NaOH or $\text{H}_2\text{SO}_4$
	0.09 M	$\text{KH}_2\text{PO}_4$			
	0.01 M	$\text{K}_2\text{HPO}_4$			
Hole scavenger	0.5 M	$\text{Na}_2\text{SO}_3$	Milli-Q water	7	-

**Table C.1** – Electrolyte used for typical PEC measurement.

Name	Concentration	Compound	Solvent	pH	adjusted with
Co-Pi	0.5 mM	$\text{Co}(\text{NO}_3)_2$	Milli-Q water	7	NaOH
	0.1 M	$\text{KH}_2\text{PO}_4$			
	0.1 M	$\text{K}_2\text{HPO}_4$			

**Table C.2** – Electrolyte used for cobalt catalyst deposition.

Name	Concentration	Compound	Solvent	pH	adjusted with
Reference	0.1 M	$\text{NaClO}_4$	Milli-Q water	7.4	NaOH
Concentrated	1 M	$\text{NaClO}_4$	Milli-Q water	7.4	NaOH
Acidic	1 M	$\text{NaClO}_4$	Milli-Q water	2.9	$\text{HClO}_4$
Alkaline	1 M	$\text{NaClO}_4$	Milli-Q water	12	NaOH
Big anion	0.1 M	NaTPB	Milli-Q water	8.6	-
Different cation	0.1 M	$\text{HClO}_4$	Milli-Q water	0	-
	0.1 M	$\text{KClO}_4$	Milli-Q water	8.3	-
	0.1 M	$\text{LiClO}_4$	Milli-Q water	7.6	-
Big cation	0.1 M	TBACl	Milli-Q water	8.6	TBAOH
Acetonitrile	0.1 M	$\text{NaClO}_4$	acetonitrile	-	-
Big cation acetonitrile	0.1 M	$\text{TBAClO}_4$	acetonitrile	-	-

**Table C.3** – Electrolyte used for EQCM and EIS analysis.

### 3.6.2 Instruments

In a typical electrochemical measurement, a three electrodes configuration was used in a "cappuccino cell"<sup>6</sup> (contact area of 0.283 cm<sup>2</sup> for the back window) consisting of a BBL coated working electrode, a platinum wire as counter electrode and a reference electrode.

Different reference (or pseudo reference) electrodes were used depending on the electrolyte or setup. They were:

- an Ag/AgCl (KCl sat.) ( $E_{\text{Ag/AgCl KCl sat.}}^0 = 0.197 \text{ V}$ );
- an Ag/AgCl (KCl 3 M) ( $E_{\text{Ag/AgCl KCl 3M}}^0 = 0.200 \text{ V}$ ), for aqueous measurement in EQCM;
- a platinum wire (calibrated at  $E_{\text{Pt}}^0 = 0.4568 \text{ V}$ ), for measurement in NaTPB;
- a silver wire (calibrated at  $E_{\text{Ag}}^0 = 0.4369 \text{ V}$ ), for OECT measurement.

The platinum and silver wire were calibrated with CV of BBL working electrode as seen in section 3.2. All potentials reported in the results were converted to the RHE reference scale using equation c.3 page 36 or to the NHE reference scale using equation c.4 page 36.

A SP-200 or a SP-300 potentiostat/galvanostat (Biologic Technologies) was used for the potentiostatic and frequency based methods.

A Keithley model 2000 multimeter (Keithley) was used to record the current in a two-electrode configuration without applying any external potential bias.

EQCM was controlled by a Gamry Interface 1000 and a Q-sense Analyzer. Frequency change was converted to mass change using the 3<sup>rd</sup> overtone and the Sauerbrey equation, equation c.25 page 44. Validation of the Sauerbrey equation was done by viscoelastic modeling with QTools software showing an average difference of 15 % compared to the results calculated with the Sauerbrey equation.<sup>7</sup>

For IPCE measurements a monochromatic illumination was provided by a 75 W Xe Tunable PowerArc Illuminator (Optical Building Blocks) and the number of photons at each wavelength was measured with a photodiode power sensor (S120VC, Thorlabs). For some IPCE measurements a white light bias (a constant illumination of the sample with broad spectrum visible light) with an intensity of about 0.1 sun was applied using a 450 W Xenon-arc lamp filtered by KG-1 glass. This white light was illuminating the sample during the sweep of the monochromatic illumination to increase the number of photogenerated carrier production (as the illumination intensity of the monochromatic illumination is typically quite low) and achieve conditions closer to solar operating conditions.

## References

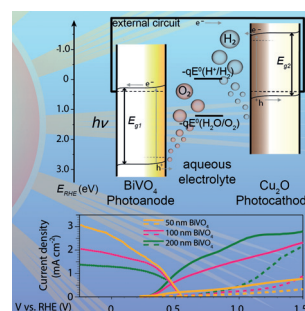
- [1] Pauline Bornoz, Fatwa F. Abdi, S. David Tilley, Bernard Dam, Roel van de Krol, Michael Grätzel, and Kevin Sivula. “A Bismuth Vanadate-Cuprous Oxide Tandem Cell for Overall Solar Water Splitting”. *The Journal of Physical Chemistry C* 118 (2014), pp. 16959–16966. DOI: 10.1021/jp500441h.
- [2] Pauline Bornoz, Mathieu S. Prévot, Xiaoyun Yu, Néstor Guijarro, and Kevin Sivula. “Direct Light-Driven Water Oxidation by a Ladder-Type Conjugated Polymer Photoanode”. *Journal of the American Chemical Society* 137 (2015), pp. 15338–15341. DOI: 10.1021/jacs.5b05724.
- [3] Allen J. Bard and Larry R. Faulkner. *Electrochemical Methods: Fundamentals and Applications, 2nd Edition*. Wiley, 2001. URL: <http://eu.wiley.com/WileyCDA/WileyTitle/productCd-04711043729.html>.
- [4] A. J. Bard, M. Stratmann, and S. Licht. “Semiconductor Electrodes and Photoelectrochemistry”. *Encyclopedia of Electrochemistry*. Vol. 6. Wiley-CH, 2002.
- [5] Andrzej Lasia. *Electrochemical Impedance Spectroscopy and its Applications*. Springer New York, 2014. DOI: 10.1007/978-1-4614-8933-7.
- [6] Tânia Lopes, Luísa Andrade, Helena Aguiar Ribeiro, and Adélio Mendes. “Characterization of Photoelectrochemical Cells for Water Splitting by Electrochemical Impedance Spectroscopy”. *International Journal of Hydrogen Energy* 35 (2010), pp. 11601–11608. DOI: 10.1016/j.ijhydene.2010.04.001.
- [7] E. F. Irwin, J. E. Ho, S. R. Kane, and K. E. Healy. “Analysis of Interpenetrating Polymer Networks via Quartz Crystal Microbalance with Dissipation Monitoring”. *Langmuir* 21 (2005), pp. 5529–5536. DOI: 10.1021/la0470737.

## **Results** **Part III**





## 4 A Bismuth Vanadate-Cuprous Oxide Tandem Cell for Overall Solar Water Splitting



In this chapter the feasibility of a BiVO<sub>4</sub>/Cu<sub>2</sub>O photoanode/photocathode tandem cell for overall unassisted solar water splitting is evaluated.

For that a BiVO<sub>4</sub> photoanode was provided by van de Krol's group[1] and a Cu<sub>2</sub>O photocathode was provided by Grätzel's group[2]. We conducted all characterization presented in this chapter, except the Cu<sub>2</sub>O.

This chapter has been adapted from:

Pauline Bornoz, Fatwa F. Abdi, S. David Tilley, Bernard Dam, Roel van de Krol, Michael Grätzel, and Kevin Sivula. "A Bismuth Vanadate-Cuprous Oxide Tandem Cell for Overall Solar Water Splitting". *The Journal of Physical Chemistry C* 118 (2014), pp. 16959–16966. DOI: 10.1021/jp500441h

### 4.1 Motivation

Despite the recent development of new materials for PEC, there are only a few examples of an all-oxide photoanode-photocathode tandem cell because of the difficulty in developing an inexpensive photocathode with high stability for the water reduction reaction and a suitable band gap for operation in a tandem cell.<sup>4,5</sup> Recently, Grätzel and co-workers have significantly enhanced the performance of electrodeposited cuprous oxide ( $\text{Cu}_2\text{O}$ ) photocathodes by improving their stability<sup>6,7</sup> and optimizing the water reduction catalysis.<sup>2</sup> This leading photocathode performance gives promise to the inexpensive, photoanode/photocathode tandem cell. However,  $\text{Cu}_2\text{O}$  with its band gap energy,  $E_g$ , of about 2.0 eV is not suitable for high STH conversion efficiency with principal photoanode materials like  $\text{Fe}_2\text{O}_3$  that have a similar  $E_g$  (2.1 eV for hematite).

The recent development of high-performance spray-deposited bismuth vanadate (monoclinic scheelite  $\text{BiVO}_4$ ,  $E_g = 2.4 - 2.5$  eV)<sup>1,8</sup> gives potential to an all-oxide photoanode/ photocathode water splitting tandem cell with an STH conversion efficiency of up to 8 % based on the band gaps and accounting for reasonable losses.<sup>4</sup> However, to the best of our knowledge, this promising combination has not yet been investigated in a tandem cell for overall water splitting.

### 4.2 Energetic and Optical Characterization

A first criteria for optimal operation as a tandem cell for overall water splitting is for the  $\text{BiVO}_4$  photoanode and the  $\text{Cu}_2\text{O}$  photocathode to be energetically matched for Z-scheme<sup>9</sup> water splitting.

For that a cuprous oxide photocathode was prepared as previously described<sup>2</sup> with atomic layer deposition protecting overlayers of aluminum-doped zinc oxide and titanium oxide. For the water reduction catalyst, a galvanostatic photodeposition of ruthenium oxide was used. The final structure of the photocathode was  $\text{FTO}/\text{Au}/\text{Cu}_2\text{O}/\text{Al:ZnO}/\text{TiO}_2/\text{RuOx}$ . Bismuth vanadate photoanodes were also prepared using a tungsten gradient doping as previously described.<sup>1</sup> These  $\text{W:BiVO}_4$  films on FTO were made at three different thickness (200 , 100 , and 50 nm).

The expected tandem cell electron energetics of an ideal  $\text{BiVO}_4/\text{Cu}_2\text{O}$ -based device are shown simplified in figure 4.1 based on the reported flat-band potentials and band gap energies. These reported values indicate that the equilibrated Fermi energy of the majority charge carriers (electrons in the n-type  $\text{BiVO}_4$  and holes in the p-type  $\text{Cu}_2\text{O}$ ) should lie between the HER and OER potentials and sufficient photopotential can be generated to overcome the required 1.23 eV plus electrochemical overpotentials.

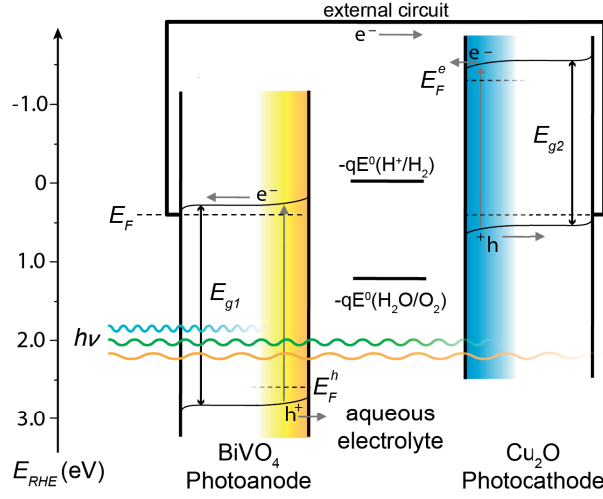


**Figure 4.1** – Simplified electron energy diagram of a bismuth vanadate photoanode-cuprous oxide photocathode tandem cell for overall water splitting. The cell is shown in the "wired" configuration under illumination with approximated positions of the Fermi energy,  $E_F$ , and the minority carrier quasi Fermi energies ( $E_F^h$  and  $E_F^e$  for holes and electrons, respectively) at the SCLJ. Band-gap energies ( $E_{g1}$  and  $E_{g2}$ ) and energy levels were adapted from Tilley et al.<sup>2</sup> and Hong et al.<sup>10</sup>

Next, it is important to verify that the two electrodes are suitably spectrally matched for solar photocurrent density. Because the two electrodes are "wired" together, the operating current density will be limited by the photoelectrode producing the least photocurrent. Because  $\text{BiVO}_4$  possesses the larger band gap energy (2.5 eV), it is the clear choice for the top cell.

Exposed directly to AM 1.5G illumination, this electrode can potentially absorb all solar photons,  $h\nu$ , with wavelength  $\lambda$  up to 500 nm. Assuming a unity Incident Photon-to-current Efficiency (IPCE), this corresponds to a maximum solar photocurrent density of  $6.3 \text{ mA} \cdot \text{cm}^{-2}$ . Assuming further that all photons not absorbed by the  $\text{BiVO}_4$  are incident on the  $\text{Cu}_2\text{O}$  (no reflection and scattering losses), the photocathode would absorb all photons with wavelength between 500 and 620 nm, given its band gap energy of 2.0 eV. This corresponds to a maximum solar photocurrent density of  $8.2 \text{ mA} \cdot \text{cm}^{-2}$  assuming unity IPCE.

While this analysis indicates only an upper-bound photocurrent density, it suggests that the  $\text{BiVO}_4/\text{Cu}_2\text{O}$  combination is reasonably well-matched for tandem cell operation. If the two electrodes used the same active areas (the most practical case for a tandem cell), the  $\text{BiVO}_4$  photoanode would just slightly limit the solar photocurrent in the ideal case with no photon losses, and a maximum water splitting photocurrent of  $6.3 \text{ mA} \cdot \text{cm}^{-2}$  would be possible corresponding to an overall STH conversion efficiency of 7.8 %.

Obviously, in a real tandem cell we expect the top electrode to exhibit considerable optical losses because of reflection and scattering, and we expect lower than maximum solar photocurrent densities because of less than unity IPCEs in both photoelectrodes. To better

understand these losses we first examine the optical properties of the  $\text{BiVO}_4$  top cell as a function of the thickness of the active layer.

Reflectance and transmittance spectra of the three different photoanodes were measured from back side illumination. Absorbance spectra were then calculated and Tauc plots, were constructed for a direct optical transition as explained in section 2.1 page 24. For measurement, electrodes were wet with a drop of water and a piece of fused quartz glass was put on top to simulate the actual device interface structure. Absorbance and transmittance curves for  $\text{BiVO}_4$  electrodes on FTO glass are shown in figure 4.2 for 50, 100, and 200 nm thick films.

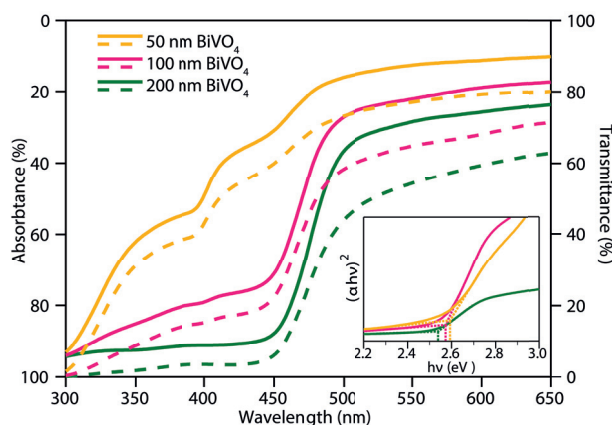


**Figure 4.2** – Absorbance (solid lines, left axis) and transmittance (dashed lines, right axis) spectra for the different thicknesses of spray-deposited  $\text{BiVO}_4$  photoanodes. Note the inversion of the absorbance axis for the better comparison to the transmittance. The inset shows the respective Tauc plot of the absorption spectra constructed for direct band gap transitions.

The curves typically show a low absorbance (high transmittance) at wavelengths longer than 500 nm and an onset of absorbance around the band gap. A direct transition Tauc plot of the absorbance data (figure 4.2, inset) gives optical band gap energies between 2.5 and 2.6 eV. While the thickest film (200 nm) showed an  $E_g^{\text{opt}}$  close to the reported literature values, thinner films showed slightly higher  $E_g^{\text{opt}}$ .

This suggests that the best spectrally matched tandem cell would be constructed with the thickest electrode. However, we note that a significant decrease in transmission of sub-band gap photons is observed with increasing sample thickness. While the origin of the sub-band gap absorbance is partly attributed to the FTO glass, it also arises from an increase in scattering. Indeed, the difference between the absorbance and transmittance, which represents light lost to specular and diffuse reflection, is around 10 – 20 % for each electrode and increases with increasing active layer thickness for wavelengths longer than  $E_g^{\text{opt}}$  because of an increased particle size.

Despite the non-ideal transmittance of the  $\text{BiVO}_4$  electrodes at sub-band gap wavelengths, altering the active layer thickness provides a method to compensate by allowing a portion of

## 4.2. Energetic and Optical Characterization

the supra-band gap photons to transmit. While the 200 nm BiVO<sub>4</sub> shows a very low transmittance at wavelengths lower than  $\lambda = 450$  nm, the 100 and 50 nm BiVO<sub>4</sub> show a 20 % and 55 % transmittance at  $\lambda = 450$  nm, respectively. These significant changes in optical properties of the BiVO<sub>4</sub> will clearly affect the photocurrent produced by the Cu<sub>2</sub>O photocathode.

We next sought to estimate the effect of the BiVO<sub>4</sub> transmittance on the expected magnitude of photocurrent produced by the Cu<sub>2</sub>O photocathode in tandem with photoanodes of various thicknesses. The IPCE of the Cu<sub>2</sub>O photocathode<sup>2</sup> was factored together with the measured BiVO<sub>4</sub> transmittance (figure 4.2) and the standard solar spectrum (AM 1.5G 100 mW · cm<sup>-2</sup>).<sup>11</sup> The resulting curves can be integrated to give the final predicted photocurrent using the method previously described.<sup>12</sup> The results of this analysis are shown in figure 4.3.

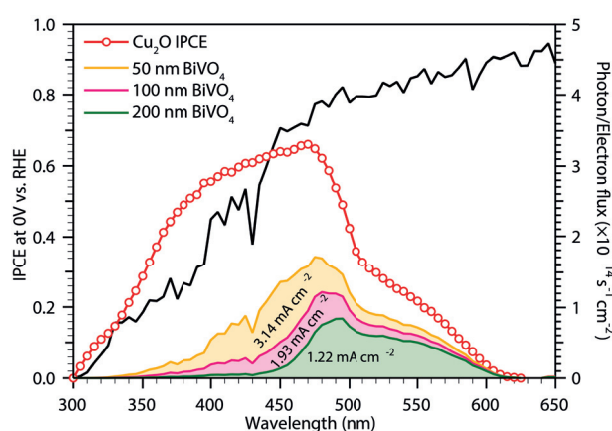


**Figure 4.3** – IPCE of Cu<sub>2</sub>O photocathode (red circles, left axis)<sup>2</sup> at 0 V<sub>RHE</sub> shown in comparison to the standard AM1.5G photon flux (black, right axis). The expected electron flux produced by the photocathode in tandem with the BiVO<sub>4</sub> photoanodes of different thicknesses is shown as the shaded areas (see main text for explanation).

The IPCE of the Cu<sub>2</sub>O electrode is consistent with a band gap of 2.0 eV given the onset at 610 nm. The shape of the Cu<sub>2</sub>O IPCE has been discussed before.<sup>2</sup> However, generally in the visible region between 420 and 470 nm, the IPCE values are in excess of 60 %. The IPCE values decrease toward the ultraviolet region because of unproductive absorption by the TiO<sub>2</sub> overlayer. The origin of the steep drop in the IPCE at 480 nm correlates well with an abrupt change in the Cu<sub>2</sub>O absorption coefficient<sup>13</sup> and suggests that optimizing light harvesting is a route for improvement.

The integration of the IPCE values with the solar AM 1.5G spectrum yields 5.0 mA · cm<sup>-2</sup> and accords with the actual photocurrent measured under simulated solar illumination.<sup>2</sup>

However, the photocurrent produced in the tandem configuration is expected to be significantly less given that even the thinnest BiVO<sub>4</sub> electrode transmits less than 75 % of the photons at the Cu<sub>2</sub>O IPCE maximum. Indeed, our estimation gives photocurrents of 3.14, 1.93, and 1.22 mA · cm<sup>-2</sup> for the Cu<sub>2</sub>O when filtered by the 50, 100, and 200 nm BiVO<sub>4</sub> pho-

toanode, respectively.

Interestingly, given the high transmittance of the 50 nm  $\text{BiVO}_4$  photoanode, our analysis predicts that about half of the  $\text{Cu}_2\text{O}$  photocurrent will arise from photons with energy greater than the  $E_g^{\text{opt}}$  of  $\text{BiVO}_4$  in this case. In contrast, photocurrent from the  $\text{Cu}_2\text{O}$  when filtered by the 200 nm  $\text{BiVO}_4$  stems only from photons with wavelength greater than 450 nm. The relatively low IPCE for the  $\text{Cu}_2\text{O}$  in this region and the poor transmission of the thick  $\text{BiVO}_4$  electrodes due to scattering and reflection results in an expected photocurrent much lower than the predicted maximum  $8.2 \text{ mA} \cdot \text{cm}^{-2}$  based on band gap alone.

However, given the maximum observed OER solar photocurrent from optimized  $\text{BiVO}_4$  photoanodes of about  $3.0 \text{ mA} \cdot \text{cm}^{-2}$  at  $1.0 V_{\text{RHE}}$ ,<sup>1</sup> the photoanode and photocathode are potentially well current-matched, despite the transmission losses through the  $\text{BiVO}_4$  and the nonideal IPCE of the  $\text{Cu}_2\text{O}$ , provided that  $3.0 \text{ mA} \cdot \text{cm}^{-2}$  can be obtained with the 50 nm  $\text{BiVO}_4$  photoanode. This upper-bound solar photocurrent density, which accounts for observed optical losses and considers actual known electrode performance, would correspond to a revised upper-bound STH conversion efficiency of ca. 4 % for the tandem cell.

### 4.3 Separate Current density-Voltage (J-V) Characterization

Next we examine the individual (3-electrode) Current density-Voltage (J-V) curves of the respective photoelectrodes in the tandem cell position to better estimate the expected tandem cell operating point.<sup>12</sup>

Tandem cells were constructed in an adapted "cappuccino cell"<sup>14</sup> with the photoanode as the first electrode in a substrate-side (or "back side") illumination and the photocathode as the second electrode (front side illumination). Separate potentiostatic J-V curves of both electrodes in this configuration were carried out in the buffered electrolyte in table C.1 page 46 at pH 6 using the three-electrode configuration described in section 3.6.2 page 47. The electrolyte solution was purged with argon. A potential scan rate of  $10 \text{ mV} \cdot \text{s}^{-1}$  was used for the potentiostatic current-potential measurements. All potentials reported in the results were converted to the RHE reference scale using equation c.3 page 36. Illumination was performed under 1 sun ( $100 \text{ mW} \cdot \text{cm}^{-2}$ ) simulated solar light. The illuminated area was  $0.283 \text{ cm}^2$ .

The J-V curves for the  $\text{BiVO}_4$  photoanodes under simulated solar (back side) illumination in pH 6 buffered electrolyte are shown in figure 4.4 as the dashed lines. Consistent with previous reports, the photocurrent onset is significantly anodic of the flat-band potential (ca.  $+0.1 - 0.2 V_{\text{RHE}}$ )<sup>15</sup> because of slow water oxidation kinetics on the bare oxide.<sup>8</sup>

### 4.3. Separate Current density-Voltage (J-V) Characterization

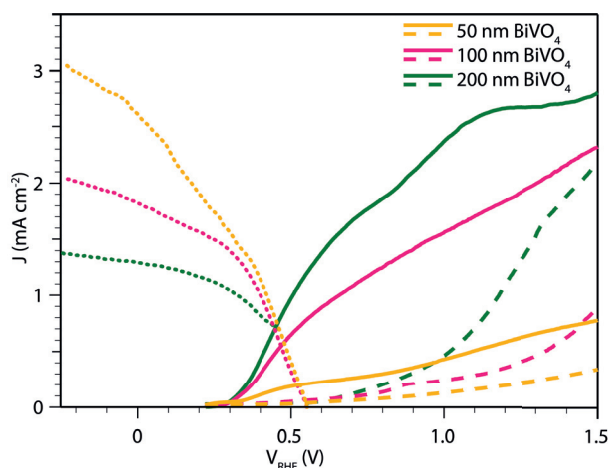


**Figure 4.4** – J-V curves for the  $\text{BiVO}_4$  photoanodes with (solid lines) and without (dashed lines) photodeposited cobalt catalyst under simulated solar illumination ( $100 \text{ mW} \cdot \text{cm}^{-2}$ ). The  $|J|$ -V curves for  $\text{Cu}_2\text{O}$  photocathode as measured in the tandem cell position (simulated solar illumination filtered by the  $\text{BiVO}_4$  photoanode) are shown as dotted lines in the corresponding color.

Reduction of the overpotential is typically achieved by the deposition of a cobalt-based catalyst (Co-Pi).<sup>8,16–18</sup> However, because the cobalt catalyst is known to absorb light without directly producing photocurrent,<sup>18</sup> it poses a problem for the tandem cell that is not present for the analysis the back-side (preferred) illumination of the  $\text{BiVO}_4/\text{Co-Pi}$  photoanode.

To avoid excess light absorption by the Co-Pi catalyst and further filtering of the light reaching the  $\text{Cu}_2\text{O}$  photocathode, we employed the photodeposition method<sup>19</sup> to optimize the amount of catalyst applied using a three-electrode cell with in electrolyte in table C.2 page 46. The catalyst was deposited potentiostatically with an applied potential of  $+0.3 \text{ V}_{\text{Ag}/\text{AgCl}(\text{KCl sat.})}$  under illumination for 4 min. The potential was controlled by an Ezstat-basic potentiostat/-galvanostat (NuVant Systems Inc.). This deposition method is preferred over the standard electrodeposition as it avoids the production of islands of catalyst that absorb light but do not enhance the water oxidation.<sup>20,21</sup> Our optimized deposition conditions gave greatly enhanced J-V performance (figure 4.4, solid lines) without any notable change in the UV-vis transmittance (data not shown). All three thicknesses of  $\text{BiVO}_4$  showed photocurrent onsets at  $+0.3 \text{ V}_{\text{RHE}}$  consistent with previous results.<sup>1,19</sup>

The magnitude of the photocurrent for the 200 nm  $\text{BiVO}_4$  photoanode was also consistent with the state of the art at around  $3 \text{ mA} \cdot \text{cm}^{-2}$  at  $+1.23 \text{ V}_{\text{RHE}}$ . However, the photocurrent of the thinner  $\text{BiVO}_4$  electrodes was significantly lower because of the decreased light absorption. Indeed, because of the known limitation of majority carrier transport even in doped  $\text{BiVO}_4$  electrodes, the thickness is typically kept to a minimum to reduce this loss. Reducing the thickness from the optimized 200 nm and reducing the number of photons absorbed naturally lowers the produced solar photocurrent.



We note that the photocurrent observed in figure 4.4 at  $+1.0 V_{\text{RHE}}$  scales well with the absorption of the  $\text{BiVO}_4$  electrodes at ca. 400 nm illumination (figure 4.2). While the 50 nm  $\text{BiVO}_4$  electrode provides sufficient optical transmission for a tandem cell operating at  $3.0 \text{ mA} \cdot \text{cm}^{-2}$ , the less than  $1 \text{ mA} \cdot \text{cm}^{-2}$  produced by this electrode will certainly limit the tandem cell operating current. In general, efforts to increase the transparency of the  $\text{BiVO}_4$  electrodes to sub-band gap photons are needed to increase the amount of light available for the  $\text{Cu}_2\text{O}$ .

Further insight into the expected operation of the (2-electrode) tandem cell can be gained by comparing the J-V curves of both the photoanode and photocathode. The operating current density is found where the absolute values of the (3-electrode) J-V curves for the photoanode and the photocathode intersect, provided that each electrode's J-V curve was acquired in the same conditions (e.g., electrolyte, illumination).<sup>12</sup> To determine this point we overlaid the absolute value (as the current densities are conventionally opposite in sign for the photocathode and photoanode) of the J-V curves for the  $\text{Cu}_2\text{O}$  photocathode taken with light filtered from the  $\text{BiVO}_4$  photoanodes of various thicknesses. These  $|J|$ -V curves are shown as dotted lines, cathodic of the  $\text{BiVO}_4$  J-V traces, in figure 4.4.

The J-V curves of the  $\text{Cu}_2\text{O}$  photocathode generally have an onset of photocurrent anodic of  $0.5 V_{\text{RHE}}$  as previously shown.<sup>2</sup> Interestingly, the onset of the water-reducing photocurrent did not significantly change with the changing illumination conditions, indicating that the photocurrent was not limited by the free energy of the photogenerated carriers at these illumination intensities.

In addition, we note that the value of photocurrents at  $0 V_{\text{RHE}}$  of  $2.61$ ,  $1.83$ , and  $1.29 \text{ mA} \cdot \text{cm}^{-2}$  when filtered by the 50, 10, and 200 nm thick  $\text{BiVO}_4$  films, respectively, closely matches the integrated photocurrent density given in figure 4.3. The larger discrepancy observed for the  $\text{Cu}_2\text{O}$  photocurrent when filtered by the 50 nm  $\text{BiVO}_4$  ( $3.14$  versus  $2.61 \text{ mA} \cdot \text{cm}^{-2}$ , 16 % difference) is most likely due to the proportionally fewer UV photons produced by the solar simulator used for this work.

Overall, comparison of the  $\text{Cu}_2\text{O}$  J-V curves to the  $\text{BiVO}_4$  indicates that the 100 nm  $\text{BiVO}_4$  film best spectrally matches the tandem cell as both electrodes produce roughly  $2 \text{ mA} \cdot \text{cm}^{-2}$  photocurrent at high anodic or cathodic applied potentials.

Examination of the intersection points of the photoanode and photocathode J-V curve gives operating point photocurrent densities of  $0.20$ ,  $0.55$ , and  $0.71 \text{ mA} \cdot \text{cm}^{-2}$  for the 50, 100, and 200 nm thick  $\text{BiVO}_4$  films, respectively (representing 0.25, 0.68, and 0.87 % STH conversion efficiency, respectively). Remarkably, we note that the operating voltages of  $+0.45 - 0.55 V_{\text{RHE}}$  are close to the equilibrium Fermi energy of  $+0.4 V_{\text{RHE}}$  predicted merely from the flatband potentials and band-edge energies shown in figure 4.1.

Given the similar onset behavior of the  $\text{Cu}_2\text{O}$  J-V curve regardless of the  $\text{BiVO}_4$  electrode used, the predicted tandem cell current density is determined more strongly by the photocurrent density of the  $\text{BiVO}_4$  close to the onset potential ( $+0.3 V_{\text{RHE}}$ ) than by that of the  $\text{Cu}_2\text{O}$ . How-



ever, we note that the operating point in each case lies much lower than the value predicted by the maximum photocurrent delivered by the  $\text{BiVO}_4$  or the  $\text{Cu}_2\text{O}$ . This is clearly due to the gradual onset of the photocurrent from both electrodes.

Further insight can be gained into the losses and potential routes for improvement by comparing the observed photocurrent onset voltages for both the  $\text{Cu}_2\text{O}$  ( $+0.55 V_{\text{RHE}}$ ) and the  $\text{BiVO}_4$  ( $+0.3 V_{\text{RHE}}$ ) to their reported flat band potentials ( $+0.8 V_{\text{RHE}}$  and  $+0.1 V_{\text{RHE}}$ , respectively).<sup>7,15</sup>

Here, it is clear that the operating point in all cases could be improved with a decrease in required overpotential for either electrode. In both cases about 200 mV is lost because of overpotential leading to an overall loss of close to 0.5 V. Eliminating this overpotential without altering the onset slopes of the photocurrent would result in an operating point current density of  $1.2 \text{ mA} \cdot \text{cm}^{-2}$  for the 100 nm  $\text{BiVO}_4$  tandem cell. However, accomplishing this is problematic for the  $\text{Cu}_2\text{O}$  (as the band bending and photovoltage of the layered photocathode system are determined by the buried junction of  $\text{Cu}_2\text{O}$  and the protecting overlayer). Any further increase in the photocurrent requires improvement of the onset slope (fill factor).

#### 4.4 Tandem Cell Characterization

Despite the large loss of potential current density resulting from the nonideal onset behavior of both electrodes, the nonzero operating points imply that a two-electrode tandem cell should be capable of unassisted solar water splitting.

To examine this possibility, we directly connected the photoanode and photocathode (without a potentiostat or reference electrode) in the same cell and electrolyte and measured the current through the external circuit with a multimeter as a function of time with and without the Co-Pi catalysts applied to the  $\text{BiVO}_4$  photoanode. The results of these two-electrode transient experiments are shown in figure 4.5.

In all cases the  $\text{BiVO}_4/\text{Cu}_2\text{O}$  tandem cell exhibited a transient current spike upon turning on the simulated solar illumination because of capacitive charging effects.<sup>22</sup> Without the Co-Pi catalyst this spike decayed in a few seconds to a steady-state photocurrent in the 10 s of microamp range as predicted by the intersection of the J-V curves in this case. In contrast, with the Co-Pi catalyst the transient current spike decays in a more complex fashion to a finally steady-state photocurrent.

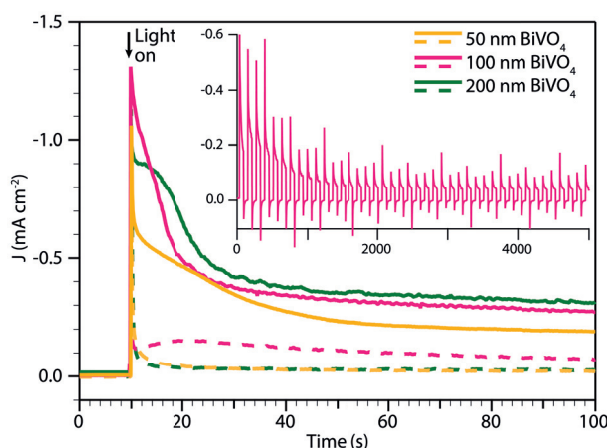


**Figure 4.5** – Two electrode  $\text{Cu}_2\text{O}/\text{BiVO}_4$  tandem cell transient current density curves with (solid lines) and without (dashed lines) the cobalt catalyst applied. Simulated solar illumination ( $100 \text{ mW} \cdot \text{cm}^{-2}$ ) was activated after 10 s in the dark. The inset shows an extended transient current density curve for the tandem cell constructed with the 100 nm  $\text{BiVO}_4$  photoanode under light-chopping conditions (60 s light on, 60 s light off).

While transient behavior was not reported previously on (photodeposited) Co-Pi on  $\text{BiVO}_4$  electrodes tested at  $+1.0 \text{ V}_{\text{RHE}}$ ,<sup>16</sup> an unsustainable catalytic wave is typically observed near the onset potential of Co-Pi modified  $\text{Fe}_2\text{O}_3$  and is attributed to a kinetic "bottleneck".<sup>21</sup>

After the decay of the catalytic wave the resulting photocurrent densities level off to some extent but continue to slowly decay. After 100 s of operation  $0.192$ ,  $0.274$ , and  $0.318 \text{ mA} \cdot \text{cm}^{-2}$  were observed for the 50, 100, and 200 nm thick  $\text{BiVO}_4/\text{Cu}_2\text{O}$  tandem cells, respectively, which are lower than the values predicted by the operating points and correspond to a STH conversion efficiency of less than 0.5 %. However, we note that the trend in the photocurrent magnitude is preserved with the thickest  $\text{BiVO}_4$  based tandem cell delivering the highest photocurrent. An extended transient measurement of the 100 nm thick  $\text{BiVO}_4/\text{Cu}_2\text{O}$  tandem cell under light-chopping conditions (figure 4.5, inset) reveals that after 5000 s a stabilized photocurrent of ca.  $50 \mu\text{A} \cdot \text{cm}^{-2}$  results. This observation implies that a significant loss or instability exists in the tandem cell.

One potential loss source not considered by the intersecting J-V curve analysis is the development of a pH gradient across the electrolyte, which causes an additional voltage loss,  $E_{\text{pH}}$ .<sup>23</sup> While this loss is important for water splitting in near-neutral pH, the time required to build up a 0.1 V loss due to pH gradient is expected to be on the order of hundreds of hours based on the photocurrent and the ionic strength of the buffered electrolyte used.<sup>24</sup> However, we note that an uneven current distribution resulting from the rough surfaces of the electrodes used in this work may cause the rapid buildup of resistance losses due to local pH gradients. The electrolyte resistance (also not considered in the 3-electrode J-V curve intersection) was also determined not to be an important loss channel given the characteristics of our testing cell.

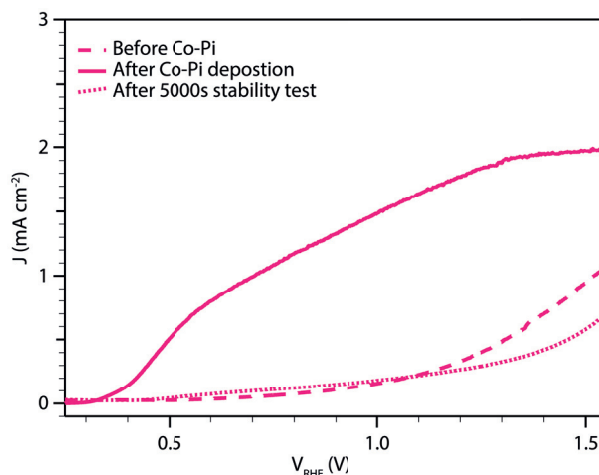


**Figure 4.6** – J-V performance of the 100 nm  $\text{BiVO}_4$  photoanode before the addition of the Co-Pi (bare  $\text{BiVO}_4$ , dashed line), immediately after the optimized photodeposition of the Co-Pi catalyst (solid line), and after the 5000 s light-chopping stability test of this electrode (dotted line).

However, we found that, upon rerunning the J-V analysis of the Co-Pi modified  $\text{BiVO}_4$  photoanodes after use in the tandem cell, the J-V behavior was identical to the precatalyst-modified electrode (see figure 4.6). This complete disappearance of the improvement given by Co-Pi overlayer is in contrast to multiple reports which show stability of the Co-Pi-modified  $\text{BiVO}_4$  photoanodes over several hours in similar electrolyte conditions (pH 6-8).<sup>1,16,18</sup> However, we note that in these stability tests the voltage applied to the  $\text{BiVO}_4$  photoanode was typically more than  $+1.0 V_{\text{RHE}}$ . It is therefore reasonable to propose that the low operating voltage of the  $\text{BiVO}_4/\text{Cu}_2\text{O}$  tandem cell (less than  $+0.5 V_{\text{RHE}}$ ) results in the dissolution of the Co-Pi overlayer.

Indeed, literature reports directly support this hypothesis. The poor stability of the Co-Pi layer is well-known on dark electrodes at low operating voltages as the catalyst "repair" mechanism (e.g., the oxidation and reposition of liberated  $\text{Co}^{2+}$ ) does not occur at a sufficient rate.<sup>24,25</sup> While dark electrolysis experiments have indicated no detectable dissolution of the catalyst at pH 6 with a water oxidation current density of  $1.0 \text{ mA} \cdot \text{cm}^{-2}$ , lowering the current density is known to accelerate catalyst dissolution.<sup>24</sup> In our case this effect could be accelerated by the buildup of local pH gradients discussed above.

Our attempts to detect the dissolved  $\text{Co}^{2+}$  in solution after tandem cell operation were complicated by the small amount of Co-Pi employed to reduce unproductive light absorption. This leaves open the possibility that the catalyst is merely deactivated but remains on the surface of the  $\text{BiVO}_4$  electrode. However, given the previous report of catalysts dissolution under low current density operation and the fact that the  $\text{BiVO}_4$  returns to its precatalyst activity after operation in the tandem cell (as opposed to being completely deactivated) suggests the former mechanism is occurring.

Regardless of the mechanism, the dissolution or deactivation of the Co-Pi layer could be ameliorated somewhat by increasing the pH of the electrolyte; however, the  $\text{Cu}_2\text{O}$  photocathode is known to give the best (most anodic) onset of photocurrent at pH 5 or less.<sup>7</sup> The trade-off between low pH (better suited for the photocathode onset potential) and high pH (better suited for Co-Pi catalyst stability) presents a fundamental challenge to the realization of a stable Co-Pi catalyzed  $\text{BiVO}_4/\text{Cu}_2\text{O}$  tandem cell. Future work applying alternative water oxidation catalysts that exhibit stable operation at low pH will potentially overcome this challenge.<sup>26,27</sup>

### 4.5 Conclusions

In this work we have investigated the optical and photoelectrochemical properties of the  $\text{BiVO}_4/\text{Cu}_2\text{O}$  photoanode/photocathode combination as a tandem cell for overall solar water splitting. This promising combination suggests maximum solar-to-hydrogen conversion efficiency of 8 % based on the known band gap energies and band-edge energy levels.

State-of-the-art Co-Pi catalyzed and tungsten-doped  $\text{BiVO}_4$  (200 nm) prepared by spray pyrolysis showed less than ideal optical transmission at sub-band wavelengths because of reflection and scattering. However, decreasing the thickness reduced this loss and a current-matched condition using a 100 nm  $\text{BiVO}_4$  was identified that limited the conversion efficiency to 4 %.

Despite the use of catalysts for water reduction and oxidation, the total remaining overpotential for photocurrent onset of ca. 0.5 V and the low fill-factor of the J-V curves reduced the maximum expected conversion efficiency to under 1 %.

Even with these losses we were able to demonstrate, for the first time, the successful unassisted operation of the  $\text{BiVO}_4/\text{Cu}_2\text{O}$  photoanode/photocathode combination as a tandem cell. Transient photocurrents decayed slowly over the course of minutes because of the dissolution of the Co-Pi catalyst, which was identified as a fundamental limitation of the  $\text{BiVO}_4/\text{Cu}_2\text{O}$  combination because of the electrolyte pH required to accommodate good photocurrent onset in both electrodes. Overcoming this aspect by employing water oxidation catalysts with increased stability at low pH, further improving the photocurrent onset behavior of both electrodes, increasing the IPCE of the  $\text{Cu}_2\text{O}$  at wavelengths between 500 and 600 nm, as well as reducing scattering by the  $\text{BiVO}_4$  have all been clearly identified as routes to improve this system toward the maximum possible STH conversion efficiency.

### References

- [1] Fatwa F. Abdi, Lihao Han, Arno H. M. Smets, Miro Zeman, Bernard Dam, and Roel van de Krol. "Efficient Solar Water Splitting by Enhanced Charge Separation in a Bismuth Vanadate-Silicon Tandem Photoelectrode". *Nature Communications* 4 (2013), p. 2195. DOI: 10.1038/ncomms3195.

- 
- [2] S. David Tilley, Marcel Schreier, João Azevedo, Morgan Stefik, and Michael Grätzel. "Ruthenium Oxide Hydrogen Evolution Catalysis on Composite Cuprous Oxide Water-Splitting Photocathodes". *Advanced Functional Materials* 24 (2014), pp. 303–311. DOI: 10.1002/adfm.201301106.
- [3] Pauline Bornoz, Fatwa F. Abdi, S. David Tilley, Bernard Dam, Roel van de Krol, Michael Grätzel, and Kevin Sivula. "A Bismuth Vanadate-Cuprous Oxide Tandem Cell for Overall Solar Water Splitting". *The Journal of Physical Chemistry C* 118 (2014), pp. 16959–16966. DOI: 10.1021/jp500441h.
- [4] Mathieu S. Prévot and Kevin Sivula. "Photoelectrochemical Tandem Cells for Solar Water Splitting". *The Journal of Physical Chemistry C* 117 (2013), pp. 17879–17893. DOI: 10.1021/jp405291g.
- [5] Gopal K. Mor, Oomman K. Varghese, Rudeger H. T. Wilke, Sanjeev Sharma, Karthik Shankar, Thomas J. Latempa, Kyoung-Shin Choi, and Craig A. Grimes. "p-type Cu-Ti-O Nanotube Arrays and Their Use in Self-biased Heterojunction Photoelectrochemical Diodes for Hydrogen Generation". *Nano Letters* 8 (2008), pp. 1906–1911. DOI: 10.1021/nl080572y.
- [6] Adriana Paracchino, Vincent Laporte, Kevin Sivula, Michael Grätzel, and Elijah Thimsen. "Highly Active Oxide Photocathode for Photoelectrochemical Water Reduction". *Nature materials* 10 (2011), pp. 456–461. DOI: 10.1038/nmat3017.
- [7] Adriana Paracchino, Nripan Mathews, Takashi Hisatomi, Morgan Stefik, S. David Tilley, and Michael Grätzel. "Ultrathin Films on Copper(I) Oxide Water Splitting Photocathodes: a Study on Performance and Stability". *Energy & Environmental Science* 5 (9 2012), pp. 8673–8681. DOI: 10.1039/C2EE22063F.
- [8] Fatwa F. Abdi and Roel van de Krol. "Nature and Light Dependence of Bulk Recombination in Co-Pi-Catalyzed BiVO<sub>4</sub> Photoanodes". *The Journal of Physical Chemistry C* 116 (2012), pp. 9398–9404. DOI: 10.1021/jp3007552.
- [9] Michael Grätzel. "Photoelectrochemical Cells". *Nature* 414 (2001), pp. 338–344. DOI: 10.1038/35104607.
- [10] Suk Joon Hong, Seungok Lee, Jum Suk Jang, and Jae Sung Lee. "Heterojunction BiVO<sub>4</sub>/WO<sub>3</sub> Electrodes for Enhanced Photoactivity of Water Oxidation". *Energy & Environmental Science* 4 (2011), pp. 1781–1787. DOI: 10.1039/C0EE00743A.
- [11] ASTM International. *Standard Tables for Reference Solar Spectral Irradiances: Direct Normal and Hemispherical on 37°CTilted Surface*. G 173-03. 2012.
- [12] Jeremie Brillet, Maurin Cornuz, Florian Le Formal, Jun-Ho Yum, Michael Grätzel, and Kevin Sivula. "Examining Architectures of Photoanode–photovoltaic Tandem Cells for Solar Water Splitting". *Journal of Materials Research* 25 (2010), pp. 17–24. DOI: 10.1557/JMR.2010.0009.

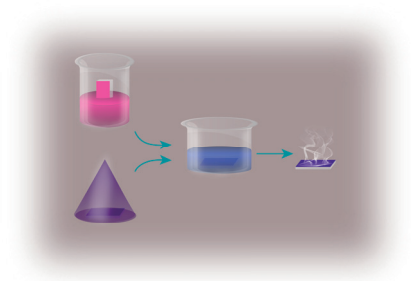
- [13] Takayuki Ito, Takahiro Kawashima, Hiroyuki Yamaguchi, Taizo Masumi, and Sadao Adachi. "Optical Properties of  $\text{Cu}_2\text{O}$  Studied by Spectroscopic Ellipsometry". *Journal of the Physical Society of Japan* 67 (1998), pp. 2125–2131. DOI: 10.1143/JPSJ.67.2125.
- [14] Tânia Lopes, Luísa Andrade, Helena Aguilar Ribeiro, and Adélio Mendes. "Characterization of Photoelectrochemical Cells for Water Splitting by Electrochemical Impedance Spectroscopy". *International Journal of Hydrogen Energy* 35 (2010), pp. 11601–11608. DOI: 10.1016/j.ijhydene.2010.04.001.
- [15] Wenjun Luo, Zaisan Yang, Zhaosheng Li, Jiyuan Zhang, Jianguo Liu, Zongyan Zhao, Zhiqiang Wang, Shicheng Yan, Tao Yu, and Zhigang Zou. "Solar Hydrogen Generation from Seawater with a Modified  $\text{BiVO}_4$  Photoanode". *Energy & Environmental Science* 4 (2011), pp. 4046–4051. DOI: 10.1039/C1EE01812D.
- [16] Diane K. Zhong, Sujung Choi, and Daniel R. Gamelin. "Near-Complete Suppression of Surface Recombination in Solar Photoelectrolysis by "Co-Pi" Catalyst-Modified  $\text{W:BiVO}_4$ ". *Journal of the American Chemical Society* 133 (2011), pp. 18370–18377. DOI: 10.1021/ja207348x.
- [17] Satyananda Kishore Pilli, Thomas E. Furtak, Logan D. Brown, Todd G. Deutsch, John A. Turner, and Andrew M. Herring. "Cobalt-phosphate (Co-Pi) Catalyst Modified Mo-doped  $\text{BiVO}_4$  Photoelectrodes for Solar Water Oxidation". *Energy & Environmental Science* 4 (2011), pp. 5028–5034. DOI: 10.1039/C1EE02444B.
- [18] Tae Hwa Jeon, Wonyong Choi, and Hyunwong Park. "Cobalt-Phosphate Complexes Catalyze the Photoelectrochemical Water Oxidation of  $\text{BiVO}_4$  Electrodes". *Physical Chemistry Chemical Physics* 13 (2011), pp. 21392–21401. DOI: 10.1039/C1CP23135A.
- [19] Diane K. Zhong, Maurin Cornuz, Kevin Sivula, Michael Grätzel, and Daniel R. Gamelin. "Photo-assisted Electrodeposition of Cobalt-Phosphate (Co-Pi) Catalyst on Hematite Photoanodes for Solar Water Oxidation". *Energy & Environmental Science* 4 (2011), pp. 1759–1764. DOI: 10.1039/c1ee01034d.
- [20] Diane K. Zhong, Jianwei Sun, Hiroki Inumaru, and Daniel R. Gamelin. "Solar Water Oxidation by Composite Catalyst/ $\alpha\text{-Fe}_2\text{O}_3$  Photoanodes". *Journal of the American Chemical Society* 131 (2009), pp. 6086–6087. DOI: 10.1021/ja9016478.
- [21] Diane K. Zhong and Daniel R. Gamelin. "Photoelectrochemical Water Oxidation by Cobalt Catalyst ("Co-Pi")/ $\alpha\text{-Fe}_2\text{O}_3$  Composite Photoanodes: Oxygen Evolution and Resolution of a Kinetic Bottleneck". *Journal of the American Chemical Society* 132 (2010), pp. 4202–4207. DOI: 10.1021/ja908730h.
- [22] Florian Le Formal, Kevin Sivula, and Michael Grätzel. "The Transient Photocurrent and Photovoltage Behavior of a Hematite Photoanode under Working Conditions and the Influence of Surface Treatments". *The Journal of Physical Chemistry C* 116 (2012), pp. 26707–26720. DOI: 10.1021/jp308591k.

- 
- [23] Emil A. Hernández-Pagán, Nella M. Vargas-Barbosa, TsingHai Wang, Yixin Zhao, Eugene S. Smotkin, and Thomas E. Mallouk. “Resistance and Polarization Losses in Aqueous Buffer–membrane Electrolytes for Water-splitting Photoelectrochemical Cells”. *Energy & Environmental Science* 5 (2012), pp. 7582–7589. DOI: 10.1039/C2EE03422K.
- [24] Yogesh Surendranath, Daniel A. Lutterman, Yi Liu, and Daniel G. Nocera. “Nucleation, Growth, and Repair of a Cobalt-based Oxygen Evolving Catalyst”. *Journal of the American Chemical Society* 134 (2012), pp. 6326–6336. DOI: 10.1021/ja3000084.
- [25] Daniel A. Lutterman, Yogesh Surendranath, and Daniel G. Nocera. “A Self-healing Oxygen-evolving Catalyst”. *Journal of the American Chemical Society* 131 (2009), pp. 3838–3839. DOI: 10.1021/ja900023k.
- [26] Frank E. Osterloh. “Inorganic Materials As Catalysts for Photochemical Splitting of Water”. *Chemistry of Materials* 20 (2007), pp. 35–54. DOI: 10.1021/cm7024203.
- [27] Alex Izgorodin, Orawan Winther-Jensen, and Douglas R. MacFarlane. “On the Stability of Water Oxidation Catalysts: Challenges and Prospects”. *Australian Journal of Chemistry* 65 (2012), pp. 638–642. DOI: 10.1071/CH12024.





## 5 Solution Processing of Poly-(benzimidazobenzophenanthroline) (BBL) Ladder Polymer



In the following three chapters, we will extensively study if a conjugated ladder type polymer, Poly(benzimidazobenzophenanthroline) (BBL), could be a suitable organic material for solar water splitting.

This first chapter will be devoted to the presentation of the BBL and description of the thin film preparation.

Parts of this chapter have been adapted from:

Pauline Borno, Mathieu S. Prévot, Xiaoyun Yu, Néstor Guijarro, and Kevin Sivula. “Direct Light-Driven Water Oxidation by a Ladder-Type Conjugated Polymer Photoanode”. *Journal of the American Chemical Society* 137 (2015), pp. 15338–15341. DOI: 10.1021/jacs.5b05724

## 5.1 Poly(benzimidazobenzophenanthroline) (BBL) Ladder Polymer

Poly(benzimidazobenzophenanthroline) (BBL) is a polymer composed of a naphthalenic and a benzenoid units condensed with an n-imino amide unit, see figure 5.1. This particular structure forms a highly conjugated planar backbone<sup>2,3</sup> specific of ladder type polymer. Its synthesis was developed in 1969 by Arnold and Van Deusen<sup>4</sup> with a polycondensation between a tetracarboxylic acid and a tetraaminobenzene, reaction shown in figure 5.1. Since then it has shown many good properties which is why it is now commercially available.

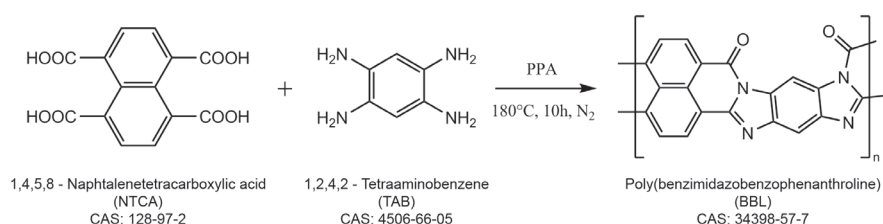


**Figure 5.1** – Synthesis of Poly(benzimidazobenzophenanthroline) (BBL) polymer by polycondensation with Polyphosphoric Acid (PPA).

Among these properties, BBL is known for exceptional stability.<sup>4</sup> It has a high thermal stability measured by Thermogravimetric analysis (TGA) and Differential Scanning Calorimetry (DSC) where the change of mass, in the case of TGA, or the heat release/absorption, in the case of DSC are recorded during the heating of a BBL sample, presented in figure 5.2. These measurements shows no phase transition detected until 450 °C\* and a decomposition reaction starting at 600 °C, i.e. a high temperature for an organic material. It has also a high chemical stability with a solubility only in strong protonic acid (as concentrated Methanesulfonic Acid (MSA) or Lewis acids).<sup>5</sup> Whereas this strong stability is a big advantage for water splitting application as it will be in contact with a solution and under strong oxidizing or reducing conditions, this characteristic will also limit its processability into thin films.

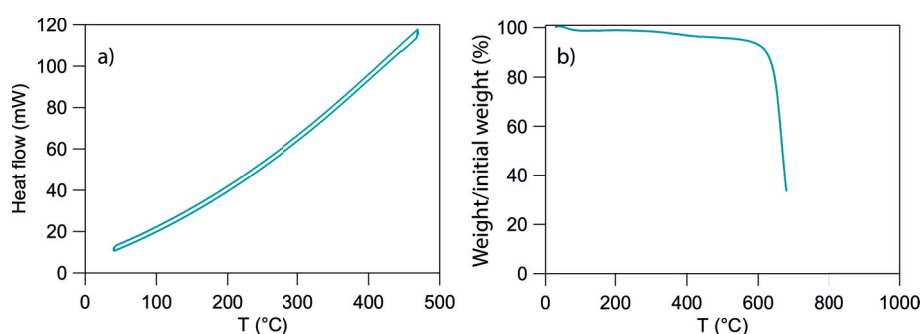


**Figure 5.2** – Thermal stability of BBL with the thermogram a) and the thermogravimetric analysis.

\* no higher temperatures were tested due to instrumental limitations.

Some molecular engineering was done to change its molecular structure and increase its solubility.<sup>6</sup> Wagner et al.<sup>7</sup> demonstrated the successful functionalization with a poly(ethylene oxide) side chain, making it water soluble which is not in our benefit. However it was shown that other routes like its precipitation in methanol/chloroform<sup>2</sup> or in a water<sup>8</sup> solution to form a dispersion are also possible to avoid solubility problems.

Its band structure was calculate by Hong et al.<sup>9</sup> with a band gap of 1.99 eV, the optical band gap is usually given around 1.8 eV.<sup>10</sup> Its HOMO level was measured from CV at 6.0 eV below  $E_{\text{vacuum}}^{\dagger 11}$  which makes it a good candidate for OER.

It has also a high electron mobility up to  $0.1 \text{ cm}^2 \cdot \text{V}^{-1} \cdot \text{s}^{-1}$ .<sup>10</sup> For this reason, BBL has been reported as an electron acceptor in OPV cells,<sup>12,13</sup> as a buffer layer for inorganic thin-film PV,<sup>11</sup> and for n-channel field-effect transistors.<sup>14,15</sup>

These favorable aspects encouraged us to consider BBL for PEC application.

## 5.2 Photoelectrode Fabrication

As previously explained, BBL is only soluble in MSA; an acidic, non-volatile with high boiling point ( $167^\circ\text{C}^{16}$ ) solvent. Due to these characteristics, thin film preparation with common methods such as spin coating becomes difficult because MSA does not evaporate easily. At the beginning of this work, different methods were tested in order to find the most an appropriate process. They are briefly described in the following paragraph and their results are summarized in figure 5.3:

**Drop casting:** consists of setting a drop of the solution onto the substrate and evaporating the solvent by heating. In the case of MSA, while it is heated, its viscosity decreases which decreases the wettability of the solution on the substrate (or increase its surface tension). Therefore the solution gathers as a drop during the evaporation process.

**Quench drying:** consists of setting a drop of the solution onto the substrate and evaporating the solvent under heat and vacuum. Compared to drop casting, the evaporation of MSA is faster and the drop phenomenon is not observed with concentrated solutions.






**Dip coating:** consists of dipping the substrate into the solution and withdrawing it at a fixed rate. The solvent evaporates once the solution forms a thin layer on the substrate during the withdrawal at the substrate/liquid/air interface. This is not the case with MSA, hence a precipitation/fixation step is needed.

**Spin coating:** consists of setting a drop of the solution and spinning the substrate. The film is formed when the solution spreads onto the substrate. In this case, the evaporation will take place during the spinning. Again, difficulties to evaporate MSA will also be encountered, hence a precipitation/fixation step is also needed.

---

<sup>†</sup> 1.5 V<sub>NHE</sub>

**Spray coating:** consists of spraying a solution on the heated substrate. Compressed air is used to create small drops of the solution that are targeted at the substrate placed on a hot plate to evaporate the solvent. This technique cannot be used with MSA due to its low volatility and toxicity.

	BBL in MSA			Dispersion in water	
	Drop casting	Quench drying	Dip coating	Spin coating	Spray coating
					
Homogeneity	✗	✗	✓	✓	✓
Scalability	✗	✗	✓	✗	✓
Thickness tunability	✗	✗	✗	✓	✓
Environmental		Acidic solution		Wasteful	

**Figure 5.3** – Summary of different methods to prepare thin film of BBL.

As shown in figure 5.3, two types of solution were used: a BBL solution in MSA and a dispersion of BBL precipitates in water. The dispersion technique avoids most pitfalls of MSA (volatility, wettability, acidity) nevertheless it also shows different drawbacks, namely the complication of creating a continuous film with BBL in its solid phase. A surfactant is also needed to help the stability of the dispersion and may remain inside the film.

In order to compare effects of the processing method on the optoelectronic properties of the film, two of these methods were chosen: the dip-coating and the spray-coating methods. Care was taken to select and develop a scalable and safe process with low waste of polymer and low energy and time consumption. The resulting properties of these films is the subject of a publication<sup>1</sup> and are summarized in chapter 6 page 79. They were prepared as described in the next section.

### 5.2.1 Dip Coating Procedure

Films were prepared as outlined in figure 5.4: a saturated solution was obtained by dissolution of BBL in Methanesulfonic Acid (MSA) (at 210 °C). After cooling to 20 °C, Fluorine-doped Tin Oxide (FTO) was dipped into this solution and withdrawn at a  $20 \text{ mm} \cdot \text{min}^{-1}$  rate. As the solvent does not evaporate, the "wet" BBL film needs to be precipitated by dipping it into pure water and further fixed by heat treatment at 150 °C in air. The films were then washed by soaking in ethanol for 1 hour, to remove residual MSA, and annealed again for 1 hour at 250 °C in air.

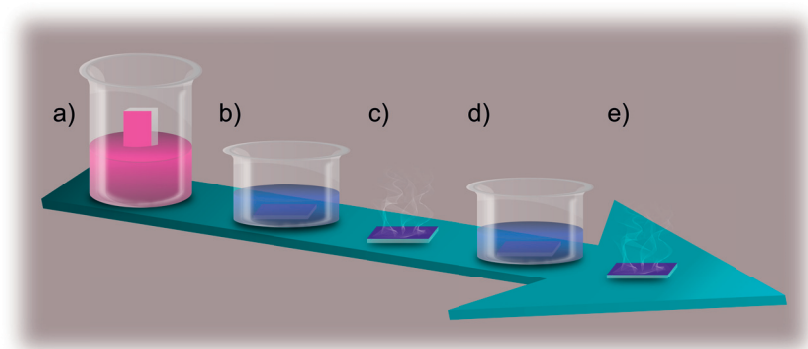


**Figure 5.4** – Schematic description of the dip coating procedure with a) dip coating in a BBL/MSA solution, b) precipitation in water, c) fixation at 150 °C 10 min, d) washing in ethanol 1 h and e) annealing at 250 °C 1 h.

With this technique the thickness of the resulting film can be controlled by varying the concentration of the BBL solution and the withdrawal rate, however the relatively low solubility of BBL in MSA (ca.  $1 \text{ mg} \cdot \text{mL}^{-1}$ ) limits the range of accessible film thickness (between 10 and 50 nm).

### 5.2.2 Spray Coating Procedure

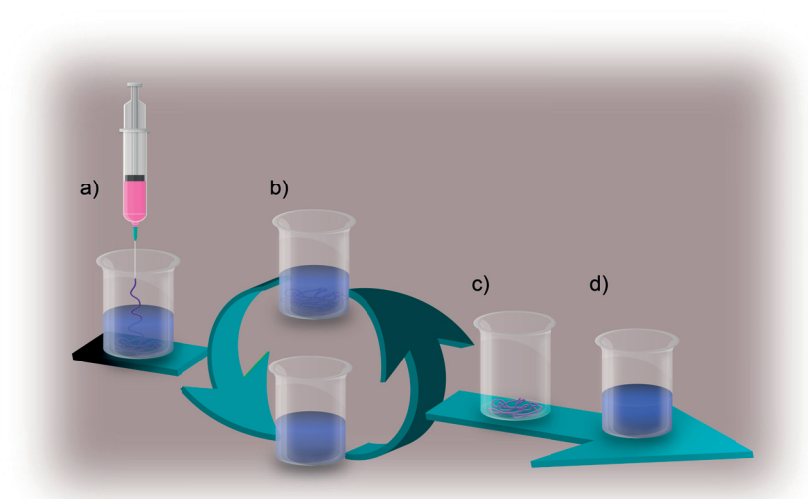


**Figure 5.5** – Schematic description of the dispersion preparation with a) wet spinning of BBL/MSA into 1 wt% Igepal® /water, b) washing with fresh water, c) dispersion in 0.15 wt.% Igepal® /water, d) breaking by sonication and filtration.

A dispersion of BBL was first prepared as outlined in figure 5.5 by adapting the work of Janietz and Sainova.<sup>8</sup> A solution of BBL in MSA is injected (through a ca.  $100 \mu\text{m}$  diameter pipette

## Chapter 5. BBL Thin Films Preparation

orifice) into a 1 wt% solution of Igepal® co-520 (a non-ionic surfactant) in water. This "wet spinning" method gives fibers of BBL of diameter of ca. 10  $\mu\text{m}$ , as shown in figure 5.6 a). The precipitate was then broken by bath sonication for 1 hour giving an acidic solution of BBL particles. BBL precipitate was washed several times with water by a centrifugation/dispersion in fresh water cycle until the supernatant was no longer acidic. The precipitate was finally dispersed in a 0.15 wt.% solution of Igepal® in water, homogenized by sonication for 1 hour at maximum power and filtered with a 5  $\mu\text{m}$  pore diameter syringe filter.

The dispersion consists of ca. 500 nm long fibers with ca. 20 nm diameter, TEM image shown in figure 5.6 b), and reaches a final concentration of 2  $\text{mg} \cdot \text{mL}^{-1}$  (0.15 wt.% Igepal® and 0.03 wt.% BBL). It is stable for several months at room temperature.

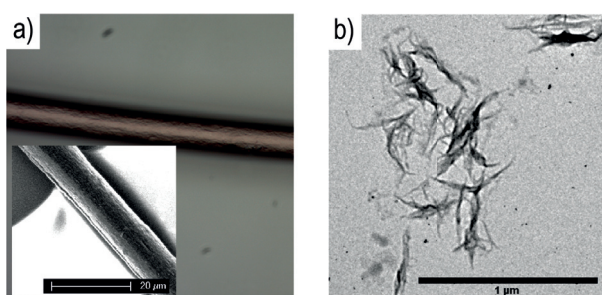


**Figure 5.6** – a) optical microscope SEM (inset) morphology of the wet-spun BBL fiber, and b) TEM image of the final BBL dispersion.

For film deposition, see figure 5.7, a substrate was placed onto a hot plate at 200 °C under a homemade external-mix two-fluid spray head. One layer of BBL was prepared by spraying 0.5 mL of the prepared BBL dispersion over 30 sec. After spraying, the film was immersed in a nitric acid bath (0.5 M) and left under stirring for 1 hour to remove the Igepal®.

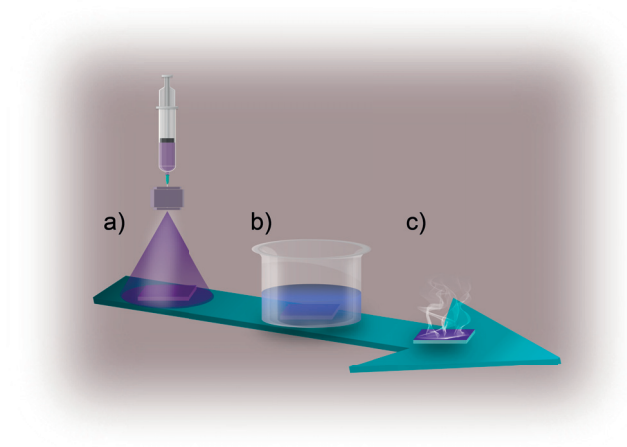


**Figure 5.7** – Schematic description of the spray deposition procedure with a) spray deposition of BBL dispersion, b) washing in 0.5 M HNO<sub>3</sub> 1 h and c) annealing at 250 °C 1 h.

The extent of the removal of the Igepal® was difficult to quantify given the relatively small amount present in the film and the large amount of washing solution employed. It is possible to determine the presence of a molecule with a Matrix-assisted Laser Desorption/Ionization Time-of-flight Mass Spectrometer (MALDI-TOF MS) analysis where a laser ionizes the molecule and detect its fragments with a mass spectrometer. This analysis confirms that the Igepal® is removed by the washing step, see figures 5.8 and 5.9, due to its presence in the washing solution. However, we cannot discount that some of the Igepal® remains in the film after the washing step.

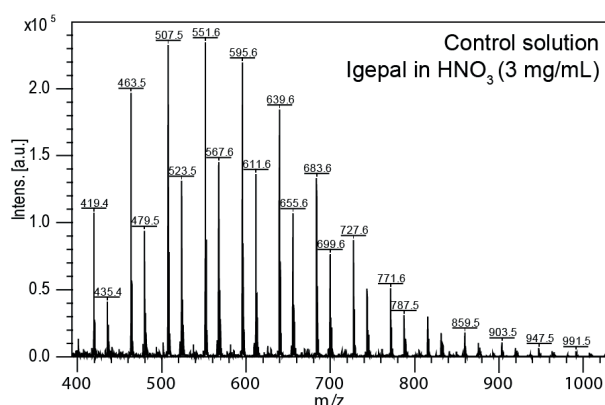


**Figure 5.8** – MALDI-TOF MS analysis of a control solution of Igepal® in nitric acid.

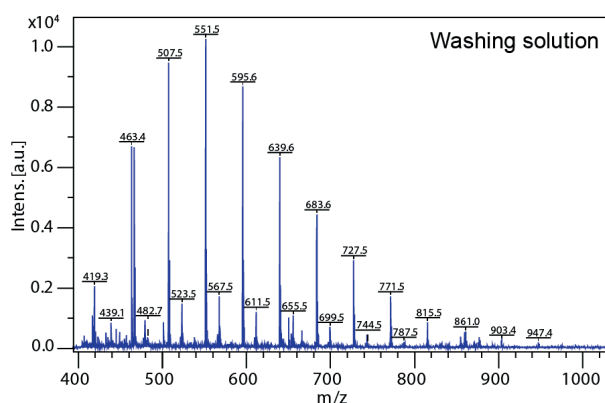


**Figure 5.9** – MALDI-TOF MS analysis of washing solution.

Nonetheless, after washing the film was annealed at 250 °C in air for 1 hour. Film thickness may be increased by iteration of the spray/wash/anneal cycle, and reduced by spraying lower amounts of the dispersion.

### 5.2.3 Overlayers Deposition

On selected films, a  $\text{TiO}_2$  overlayer (1 nm) was deposited by using a previously published procedure.<sup>17</sup>

A Nickel-Cobalt catalyst was then deposited by spin-coating a solution of 0.5 M  $\text{NiSO}_4 \cdot 6\text{H}_2\text{O}$  and 0.5 M  $\text{Co}(\text{NO}_3)_2 \cdot 6\text{H}_2\text{O}$  and drying at 250 °C for 10 min.

## 5.3 Optical Characterization

As explained previously, the main advantage of the spray coating method is its easy film thickness variation.

Thickness calibration was hence performed by spraying different amounts of dispersion on a glass substrate and measuring the resulting thickness by a profilometer, where a tip is used to measure the difference of height in a sample, results shown in figure 5.10. All thicknesses reported afterward were determined by this calibration.

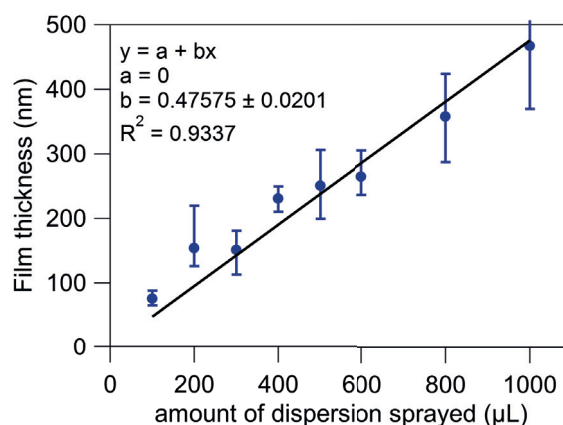


**Figure 5.10** – Calibration of the film thickness as a function of amount of dispersion sprayed.

Depending on the thickness of the film, or the amount of BBL in the film, the performances of the photoelectrode can be affected due to the different absorption properties. Absorbance of films was then measured as explained in section 2.1 page 24. Calibration of film thickness was finalized by adding absorbance information as seen in figure 5.11. In this way, thickness of a film can be determined either from the amount of dispersion used, if known, or from its absorbance.



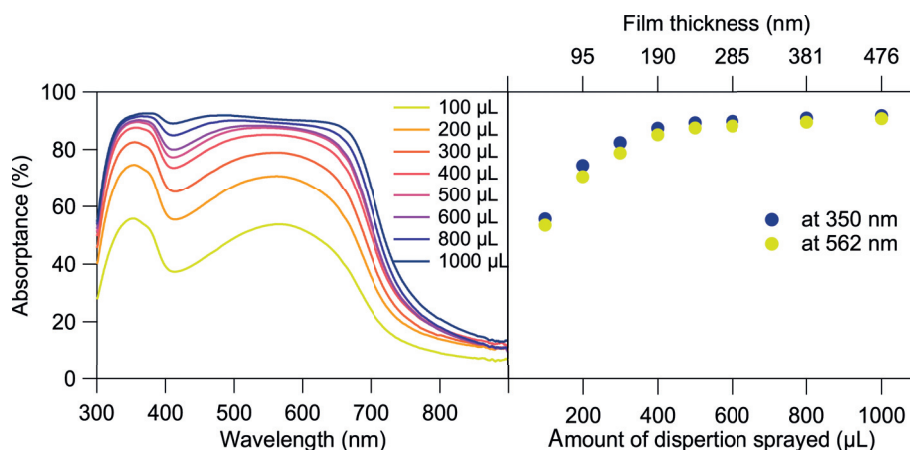


**Figure 5.11** – Absorbance of BBL films as a function of amount of dispersion sprayed correlated with film thickness calibration.

Absorption coefficient of BBL sprayed films made with different amount of dispersion can be seen in figure 5.12, matching previously reported values<sup>18</sup> with two maxima at 350 nm and 560 nm. A clear linear correspondence of the absorption coefficient with the thickness of the film can be seen, i.e. for thin films, the light needs to travel deeper so that the same amount of light is absorbed as in a thick film.

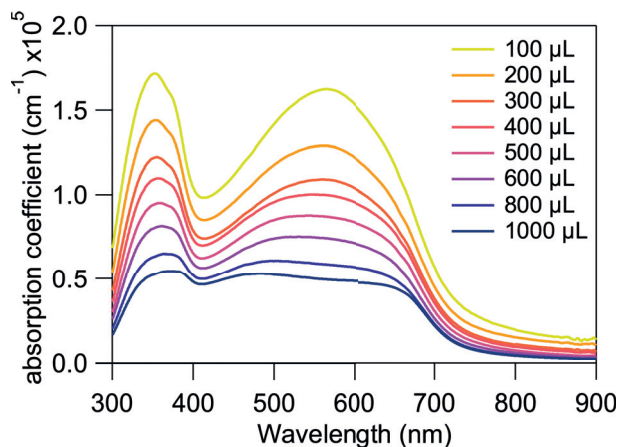


**Figure 5.12** – Absorption coefficient of BBL films as a function of amount of dispersion sprayed.

Tauc plot of  $(\alpha h\nu)^2$  versus  $h\nu$  of a BBL film of 48 nm was build and exhibits a direct band gap transition at 1.76 eV<sup>‡</sup>, close to reported values,<sup>10</sup> in figure 5.13. This result shows that only light with higher energy than 1.76 eV is absorbed by the film. This suggests that absorption of light from the BBL film would provide the sufficient energy for the OER.

<sup>‡</sup> same value for all thicknesses

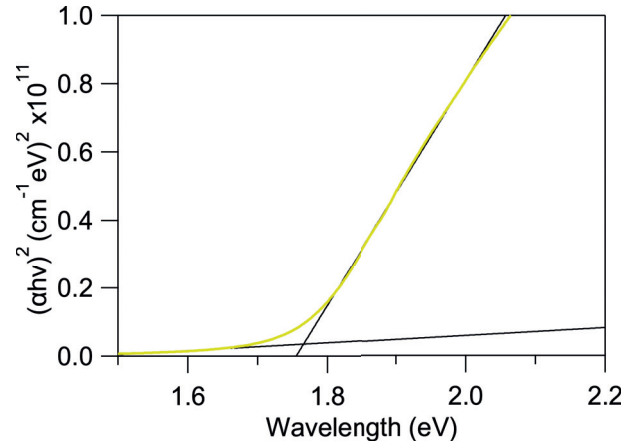


**Figure 5.13** – Tauc plot for a sprayed BBL film with 10  $\mu\text{L}$  dispersion. Intersection of linear regression of the baseline and linear regression of data increase gives a band gap value of 1.76 eV.

In order to determine the theoretical photocurrent density,  $J_{\text{BBL th}}$  in  $(\text{A} \cdot \text{m}^{-2})$  that we should measure from a BBL photoanode, considering unity, equation e.1 was used with  $\Phi_{\text{Xe lamp cal}}$  the photon density of Xenon arc lamp calibrated,  $A_{\%}(\lambda)$  the absorptance and  $e$  the elementary charge.

$$J_{\text{BBL th}} = \int_{300}^{900} (\Phi_{\text{Xe lamp cal}}(\lambda) \cdot A_{\%}(\lambda) \cdot e) d\lambda \quad (\text{e.1})$$

Absorptance of BBL films of different thickness was used and their results are summarized in figure 5.14.

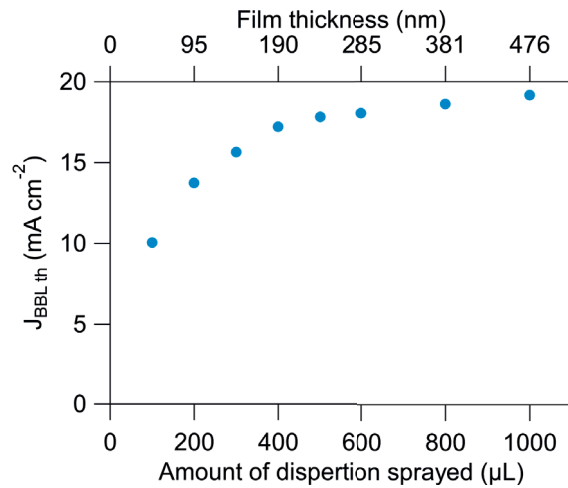


**Figure 5.14** – Theoretical photocurrent density of BBL film as a function of thickness.

This figure shows that a maximal photocurrent density close to  $20 \text{ mA} \cdot \text{cm}^{-2}$  could be expected

for 476 nm thickness BBL films.

## 5.4 Conclusions

We demonstrate that the solubility problems of an organic material can be overcome by using an adequate processing methods. Still with a solution-based process, thin films of BBL were produced. With the spray coating method, it was possible to prepare films with different thicknesses, necessary for the optimization of the photoelectrodes properties.

An appropriate optical band gap for OER of 1.76 eV was determined from light absorption properties of these films. Due to their broad absorption of light, a photocurrent of  $20 \text{ mA} \cdot \text{cm}^{-2}$  could be expected for 476 nm thick film, considering unity Incident Photon-to-current Efficiency (IPCE). This highlights the relative low loading of material necessary to obtain high absorption of light, advantage of organic material which could potentially decrease their production price.

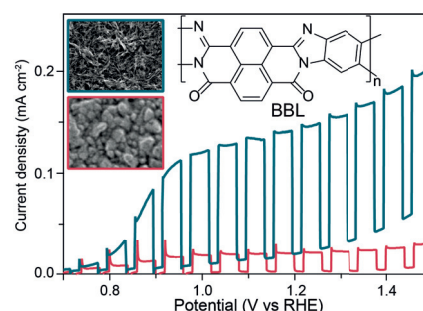
However, a lower IPCE is expected due to the possible non-formation of a space-charge layer at the SCLJ. This would lead to low exciton dissociation and hence high recombination rate. This effect will be discussed in the next chapter.

## References

- [2] Alejandro L. Briseno, Stefan C. B. Mannsfeld, Patrick J. Shamberger, Fumio S. Ohuchi, Zhenan Bao, Samson A. Jenekhe, and Younan Xia. "Self-Assembly, Molecular Packing, and Electron Transport in n-Type Polymer Semiconductor Nanobelts". *Chemistry of Materials* 20 (2008), pp. 4712–4719. DOI: 10.1021/cm8010265.
- [3] H. H. Song, A. V. Fratini, M. Chabiniy, G. E. Price, A. K. Agrawal, C.-S. Wang, J. Burkette, D. S. Dudis, and F. E. Arnold. "Crystal Structure and Thin Film Morphology of BBL Ladder Polymer". *Synthetic Metals* 69 (1995). Proceedings of the International Conference on Science and Technology of Synthetic Metals, pp. 533–535. DOI: 10.1016/0379-6779(94)02556-E.
- [4] Fred E. Arnold and R. L. Van Deusen. "Preparation and Properties of High Molecular Weight, Soluble Oxobenz[de]imidazobenzimidazoisquinoline Ladder Polymer". *Macromolecules* 2 (1969), pp. 497–502. DOI: 10.1021/ma60011a009.
- [5] Samson A. Jenekhe and Paul O. Johnson. "Complexation-Mediated Solubilization and Processing of Rigid-Chain and Ladder Polymers in Aprotic Organic Solvents". *Macromolecules* 23 (1990), pp. 4419–4429. DOI: 10.1021/ma00222a015.
- [6] Sami-Pekka Hirvonen and Heikki Tenhu. "Modification of Naphthalenic Unit in BBL Main Chain". *Synthetic Metals* 207 (2015), pp. 87–95. DOI: 10.1016/j.synthmet.2015.06.013.

- [7] Michal Wagner, Anna Österholm, Sami-Pekka Hirvonen, Heikki Tenhu, Ari Ivaska, and Carita Kvarnström. "Characterization of Water-Dispersible n-Type Poly(benzimidazobenzophenanthroline) Derivatives". *Macromolecular Chemistry and Physics* 212 (2011), pp. 1567–1574. DOI: 10.1002/macp.201100044.
- [8] Silvia Janietz and Dessislava Sainova. "Significant Improvement of the Processability of Ladder-Type Polymers by Using Aqueous Colloidal Dispersions". *Macromolecular Rapid Communications* 27 (2006), pp. 943–947. DOI: 10.1002/marc.200600045.
- [9] Sung Y. Hong, Miklos Kertesz, Yong S. Lee, and Oh Kil Kim. "Geometrical and Electronic Structures of a Benzimidazobenzophenanthroline-Type Ladder Polymer (BBL)". *Macromolecules* 25 (1992), pp. 5424–5429. DOI: 10.1021/ma00046a046.
- [10] Amit Babel and Samson A. Jenekhe. "High Electron Mobility in Ladder Polymer Field-Effect Transistors". *Journal of the American Chemical Society* 125 (2003), pp. 13656–13657. DOI: 10.1021/ja0371810.
- [11] Vignesh Gowrishankar, Christine K. Luscombe, Michael D. McGehee, and Jean M.J. Fréchet. "High-Efficiency, Cd-Free Copper-Indium-Gallium-Diselenide/Polymer Hybrid Solar Cells". *Solar Energy Materials and Solar Cells* 91 (2007), pp. 807–812. DOI: 10.1016/j.solmat.2007.01.012.
- [12] Maksudul M. Alam and Samson A. Jenekhe. "Efficient Solar Cells from Layered Nanostructures of Donor and Acceptor Conjugated Polymers". *Chemistry of Materials* 16 (2004), pp. 4647–4656. DOI: 10.1021/cm0497069.
- [13] Samson A. Jenekhe and Shujian Yi. "Efficient Photovoltaic Cells from Semiconducting Polymer Heterojunctions". *Applied Physics Letters* 77 (2000), pp. 2635–2637. DOI: 10.1063/1.1320022.
- [14] Amit Babel and Samson A. Jenekhe. "n-Channel Field-Effect Transistors from Blends of Conjugated Polymers". *The Journal of Physical Chemistry B* 106 (2002), pp. 6129–6132. DOI: 10.1021/jp020695l.
- [15] Amit Babel and Samson A. Jenekhe. "Electron Transport in Thin-Film Transistors from an n-Type Conjugated Polymer". *Advanced Materials* 14 (2002), pp. 371–374. DOI: 10.1002/1521-4095(20020304)14:5<371::AID-ADMA371>3.0.CO;2-5.
- [16] Acros Organics. *Methanesulfonic acid, Safety Data Sheet*. Tech. rep. Acros Organics, 2015.
- [17] S. David Tilley, Marcel Schreier, João Azevedo, Morgan Stefik, and Michael Grätzel. "Ruthenium Oxide Hydrogen Evolution Catalysis on Composite Cuprous Oxide Water-Splitting Photocathodes". *Advanced Functional Materials* 24 (2014), pp. 303–311. DOI: 10.1002/adfm.201301106.
- [18] John A. Osaheni, Samson A. Jenekhe, Andrew Burns, Gang Du, Jinsoo Joo, Zhaohui Wang, Arthur J. Epstein, and Chi Shun Wang. "Spectroscopic and Morphological Studies of Highly Conducting Ion-Implanted Rigid-Rod and Ladder Polymers". *Macromolecules* 25 (1992), pp. 5828–5835. DOI: 10.1021/ma00047a040.

## 6 Direct Light-Driven Water Oxidation by a Ladder-Type Conjugated Polymer Photoanode



Here we present promising performance and stability of the BBL as a photoanode in a direct Semiconductor-liquid Junction (SCLJ) configuration for solar water oxidation. Films were prepared as described in chapter 5 page 67.

This chapter has been adapted from:

Pauline Bornoz, Mathieu S. Prévot, Xiaoyun Yu, Néstor Guijarro, and Kevin Sivula. “Direct Light-Driven Water Oxidation by a Ladder-Type Conjugated Polymer Photoanode”. *Journal of the American Chemical Society* 137 (2015), pp. 15338–15341. DOI: 10.1021/jacs.5b05724

## 6.1 Morphology

To continue our investigation of BBL as a potential photoanode material, we first examined the effect of the thin-film morphology on the extraction of photogenerated charges. Indeed, the relatively short excited-state transport length expected in BBL<sup>2</sup> suggests a high surface area mesostructured SCLJ would be beneficial to charge extraction similar to a bulk heterojunction OPV. BBL thin-films were prepared via two different deposition techniques, described in chapter 5 page 67: dip coating from a BBL solution in Methanesulfonic Acid (MSA)<sup>3</sup> and spray deposition of an aqueous BBL nanofiber dispersion.<sup>4,5</sup>

Scanning Electron Microscopy (SEM), figure 6.1, reveals considerable morphological differences with respect to the deposition technique. While both films display a homogeneous coverage of the FTO, the dip-coated film (figure 6.1 a) and d)) shows a relatively smooth surface with feature size similar to the underlying FTO (100 – 500 nm). In contrast, the spray-coated film (figure 6.1 b) and e)) exhibits feature size as small as 20 nm and a higher roughness due to the interconnecting network formed from the nanofiber dispersion.

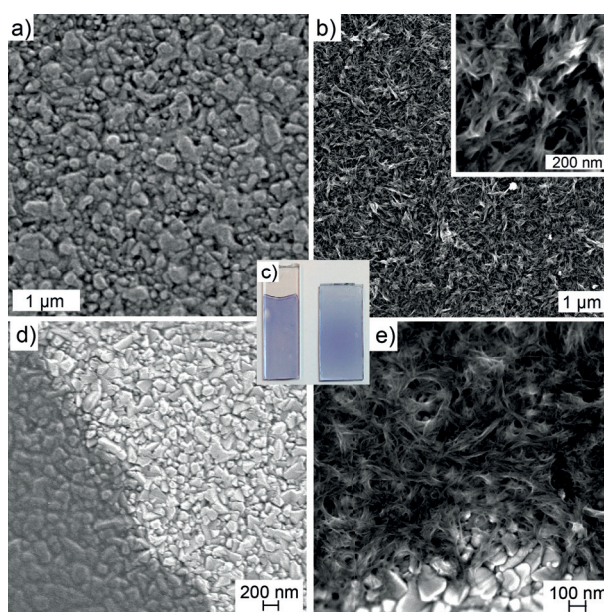


**Figure 6.1** – SEM top view of a) and d) an optimized dip-coated and b) and e) spray coated films with c) optical images of both electrodes.

## 6.2 Linear Sweep Voltammetry (LSV) in Sacrificial Electrolyte

To determine the effect of the morphology on the PEC performance we prepared films using both deposition methods to have similar light absorption (figure 6.13). The two similarly absorbing films were next examined by Linear Sweep Voltammetry (LSV) in a three-electrode PEC cell using a buffered aqueous electrolyte (pH 7) and a hole scavenger ( $\text{SO}_3^{2-}$ ), see table C.1 page 46, under intermittent simulated solar illumination ( $100 \text{ mW} \cdot \text{cm}^{-2}$ ). The oxidation of



## 6.2. Linear Sweep Voltammetry (LSV) in Sacrificial Electrolyte

$\text{SO}_3^{2-}$  is thermodynamically and kinetically more facile than the oxidation of water.<sup>6</sup> As such, measuring photocurrent for  $\text{SO}_3^{2-}$  oxidation enables the investigation of the PEC properties of BBL with minimum kinetic limitations.

The LSV data are presented in figure 6.2 with respect to the Reversible Hydrogen Electrode (RHE). Both BBL electrodes show an anodic photocurrent upon illumination (n-type behavior) and reproducibility through the scanned potential range.

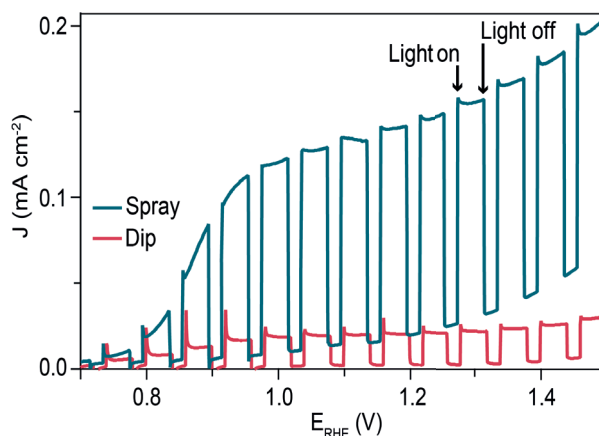


**Figure 6.2** – J-V curve of a thin sprayed film (blue line) and a dip-coated film (red line) in sacrificial electrolyte (0.5 M  $\text{Na}_2\text{SO}_3$ , pH 7) under chopped light substrate-side illumination (scan rate  $10 \text{ mA} \cdot \text{s}^{-1}$ ).

Moreover, the LSV behavior offers insight into charge transport and transfer. The dip-coated film exhibits transient spikes when illuminated in the photocurrent onset range (from  $+0.7$  to  $1.0 \text{ V}_{\text{RHE}}$ ), suggesting a limitation of charge transfer to the  $\text{SO}_3^{2-}$  (accumulation of holes at the SCLJ). In contrast, only small spikes are seen in the spray-coated film, and the photocurrent density in the plateau region (from  $+1.0$ – $1.3 \text{ V}_{\text{RHE}}$ ) is 6.5 times higher. Given the similar light absorption of the two electrodes, it is reasonable to conclude that greater photocurrent density of the spray-coated film results from the porous morphology, which facilitates harvesting of the photoexcited states due to their short transport distance.

Optimization of the spray-coating deposition method showed that films thicker than 40 nm gave higher photocurrent density,  $J_{\text{ph}}$ , (figure 6.3). Electrodes with a thickness of about 120 nm gave an average  $J_{\text{ph}}$  of  $0.23 \pm 0.02 \text{ mA} \cdot \text{cm}^{-2}$  at  $+1.23 \text{ V}_{\text{RHE}}$ , while thicker films gave lower values.

$J_{\text{ph}}$  was consistently  $\sim 30\%$  larger for substrate-side illumination (compare to electrolyte-side) indicating a limitation in majority carrier (electron) transport. This observation together with the effect of the nanostructure are consistent with free charge generation occurring exclusively in high proximity to the SCLJ, where excitons are split either by direct hole injection into the electrolyte or a space-charge electric field. The electron transport could be perhaps limited due to grain boundaries between the individual fibers.

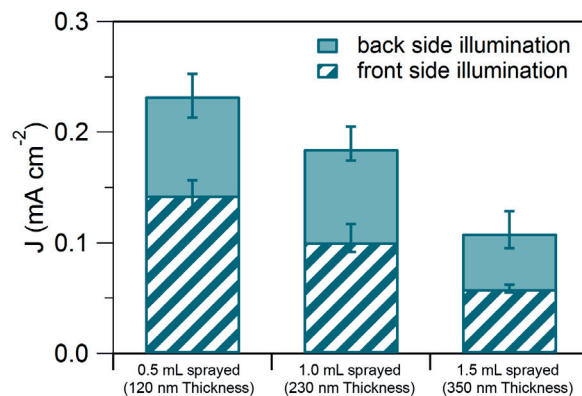


**Figure 6.3** – Comparison of back side (solid) and front side (striped) illumination photocurrent at 1.23  $V_{\text{RHE}}$  of a BBL spray coated film in a  $\text{Na}_2\text{SO}_3$  (pH 7) as a function of number of deposited BBL layers.

### 6.3 Mott-Schottky (M-S) Analysis

To next obtain information regarding the electronic structure of the SCLJ and determine the suitability of BBL to oxidize water, electrochemical impedance spectroscopy and Mott-Schottky (M-S) analysis were performed on spray-coated electrodes at various pH without sacrificial hole acceptors. We used thicker films (230 nm) to avoid direct substrate-electrolyte contact.

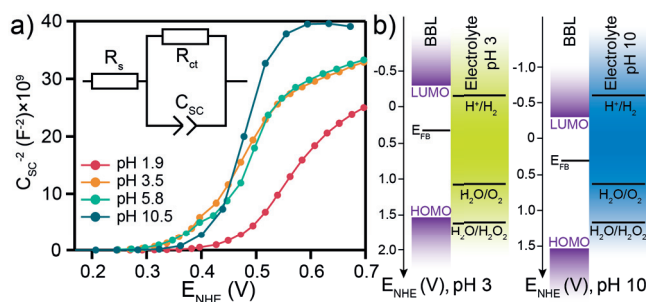


**Figure 6.4** – a) Mott-Schottky plot from a spray coated BBL film in aqueous electrolyte (buffered sulfate/phosphate) at various pH. A Randle equivalent circuit was used to fit the impedance data (inset). b) energy band diagram of BBL under flat-band conditions at pH 3 and 10.

Figure 6.4 a) shows the M-S plot obtained using the space charge capacitance,  $C_{\text{SC}}$ , extracted from the Nyquist plots (figure 6.14), which were fit with a simple Randle equivalent circuit (figure 6.4 a) inset). For each pH, the expected accumulation region, where  $C_{\text{SC}}^{-2}$  is small, is observed in figure 6.4 a) at potentials  $< \sim +0.23 V_{\text{NHE}}$ . At more positive voltages, an increase in  $C_{\text{SC}}^{-2}$  is observed consistent with a space-charge depletion region. Complete depletion of the semiconductor film leads to a leveling-off of  $C_{\text{SC}}^{-2}$  at higher applied potentials.



#### 6.4. Linear Sweep Voltammetry (LSV) in Non-Sacrificial Electrolyte

We note that application of the M-S model rigorously requires a planar electrode. The sublinear onset of the depletion region is reasonably due to a changing effective surface area as the small features of the electrodes are depleted.<sup>7</sup> Given the nanostructure, the flat-band potential,  $E_{fb}$ , will be overestimated by extrapolating the linear region of the plots, and the  $E_{fb}$  is better estimated by regression of the onset region of  $C_{SC}^{-2}$ .

Nevertheless, it is clear that in the pH range from 3.5 to 10.5,  $E_{fb}$  only varies slightly with pH. We estimate a value for  $E_{fb}$  of  $+0.31 \pm 0.03 V_{NHE}$ , which is consistent with the observed onset of photocurrent when using the sacrificial hole acceptor  $SO_3^{2-}$ . In contrast, at pH 1.9 a positive shift of  $E_{fb}$  to  $+0.40 V$  is observed.

While inorganic oxide semiconductors typically exhibit a Nernstian shift with pH due to the dynamic equilibrium of  $H^+$  and  $OH^-$  adsorption/desorption,<sup>8,9</sup> it is likely that few (if any) species adsorb at the BBL/electrolyte interface in the pH range from 3.5 to 10.5 leading to the constant  $E_{fb}$ . In contrast, the known acido-basic behavior of BBL with a  $pK_a$  of 2.2<sup>10,11</sup> could explain the shift of  $E_{fb}$  at pH 1.9.

The  $E_{fb}$  estimation together with the band gap and LUMO position<sup>12</sup> allow construction of an energy band diagram of BBL in water at flat-band conditions for different pH, see figure 6.4 b). At pH 3 the HOMO is well-positioned for the Oxygen Evolution Reaction (OER), and the driving force for the OER reasonably increases with pH given the constant  $E_{fb}$  of the BBL.

#### 6.4 Linear Sweep Voltammetry (LSV) in Non-Sacrificial Electrolyte

To evaluate the ability of the bare BBL to directly photo-oxidize water, we next measured 230 nm thick spray coated electrodes in aqueous electrolyte without a sacrificial hole scavenger at different pH.

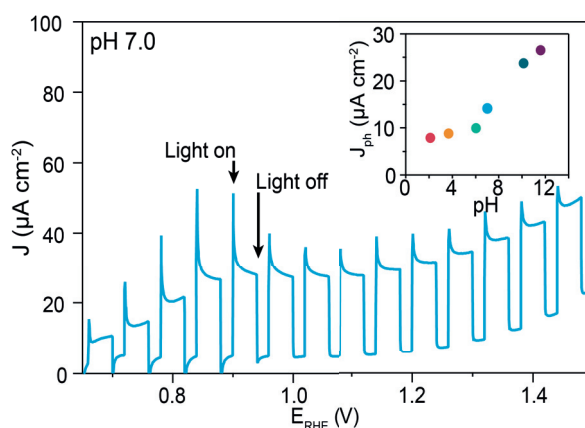


**Figure 6.5** – J-V (LSV,  $10 mV \cdot s^{-1}$ ) curve of a spray coated BBL film in aqueous sulfate/phosphate electrolyte (pH 7) under chopped illumination. The inset shows the evolution of the photocurrent density at  $1.23 V_{RHE}$  with the pH.

An example of a LSV at pH 7 is given in figure 6.5. Here the onset of photocurrent is similar to the sacrificial case, however the photocurrent density is considerably smaller and large transient spikes are observed, especially near the photocurrent onset potential. Remarkably, sustained photocurrent was observed as a plateau region of the LSV from  $\sim +0.9 - 1.4$  V. The sustained  $J_{ph}$  in the plateau region (after the decay of the transient, taken to be 15 s, see figure 6.15) under continuous 1 sun illumination ( $100 \text{ mA} \cdot \text{cm}^{-2}$ ) in different pH is given in the inset of figure 6.5. The magnitude of  $J_{ph}$  increases with pH consistent with the increasing driving force.

### 6.5 Determination of the Photooxidation Reaction

Importantly, the possibility that the photocurrent arises from oxidation of the BBL itself was eliminated through longer stability measurements, see figure 6.6.

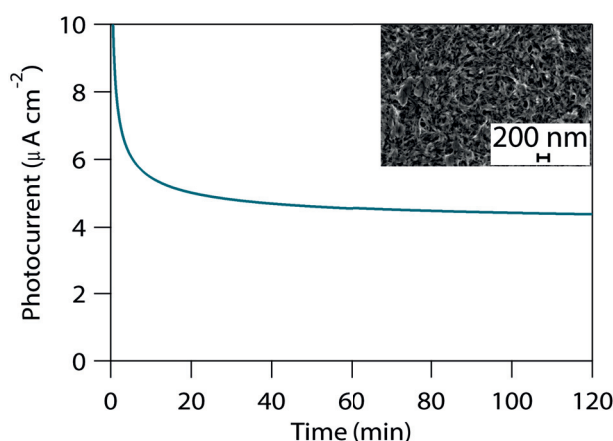


**Figure 6.6** – Photocurrent density (current density under illumination minus the current under dark) as a function of time of a BBL spray coated film at  $1.23 V_{RHE}$  in aqueous electrolyte ( $0.5 \text{ M Na}_2\text{SO}_4 + 0.09 \text{ M KH}_2\text{PO}_4 + 0.01 \text{ M K}_2\text{HPO}_4$ , pH 7) and SEM top view of the BBL spray deposited film after electrochemical testing (inset).

A 43 % decay of the photocurrent is observed over the first 10 min after which a steady-state photocurrent is obtained. During the measurement period, 31 mC passed through the exposed area of the photoanode, which is 12 times the charge needed to completely oxidize the BBL considering that  $126 \mu\text{g}$  of polymer was estimated to be in the exposed area. Moreover, SEM of the electrode after 3 hours total testing time shows no visible degradation, figure 6.6 b), and Raman spectra, figure 6.16, before and after testing show no difference.

The Incident Photon-to-current Efficiency (IPCE) (figure 6.7) verifies that the photocurrent in nonsacrificial electrolyte at pH 7 arises from light absorption by the BBL. Integrating the IPCE with the standard solar spectrum (AM 1.5G) gives a  $J_{ph}$  of  $167 \mu\text{A} \cdot \text{cm}^{-2}$ . However when a white light bias is used during the IPCE measurement an integrated  $J_{ph}$  of  $78 \mu\text{A} \cdot \text{cm}^{-2}$  is

found. This effect can be ascribed to increased geminate recombination in the film.<sup>13</sup>

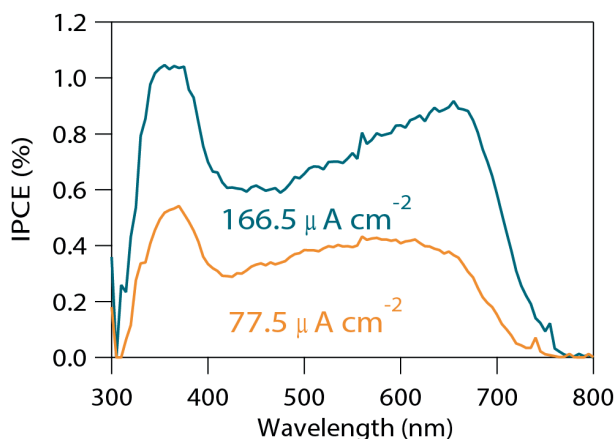


**Figure 6.7** – IPCE of a spray coated BBL film at 1.23 V<sub>RHE</sub> in aqueous electrolyte (0.5 M Na<sub>2</sub>SO<sub>4</sub> + 0.09 M KH<sub>2</sub>PO<sub>4</sub> + 0.01 M K<sub>2</sub>HPO<sub>4</sub>, pH 7) with (yellow line) and without (blue line) a white bias light of ca. 0.1 sun. Predicted values of the photocurrent density obtained by multiplying the IPCE with the standard AM 1.5G solar spectrum and integration are also shown.

Indeed, the reduced electric field (band flattening) that occurs at higher illumination intensity due to charge accumulation at the SCLJ increases the probability of charge recombination. Since we actually expect an accumulation of photo-generated holes at the SCLJ (as indicated by the transient spikes) to be favorable for water oxidation due to the requirement of 4 photo-generated holes to participate to produce one molecule of O<sub>2</sub>, this observation brings into question the nature of the sustained oxidation reaction occurring on the bare electrode.

In fact the observation of O<sub>2</sub> production by gas chromatography, using the procedure described by Prévot, Guijarro, and Sivula,<sup>14</sup> was unsuccessful despite the expected concentration being within GC detection limits. This suggests that molecular O<sub>2</sub> is not the product of the sustained photo-oxidation reaction.

Another possibility is that water oxidation occurs via a two-electron process producing H<sub>2</sub>O<sub>2</sub>. This oxidation is thermodynamically feasible ( $E = +1.8\text{ V}_{\text{RHE}}$ ),<sup>15</sup> as it corresponds roughly to the estimated HOMO level position under flat-band conditions at pH 6. Moreover ketonic functional groups on BBL could support the production of H<sub>2</sub>O<sub>2</sub> similar to observations on oxidized carbon nanotubes.<sup>16</sup> However, H<sub>2</sub>O<sub>2</sub> was not directly detectable in the electrolyte by the mean of KMnO<sub>4</sub> titration, likely because the produced H<sub>2</sub>O<sub>2</sub> is directly reduced at the anode to produce the hydroxyl radical (•OH).<sup>17</sup>

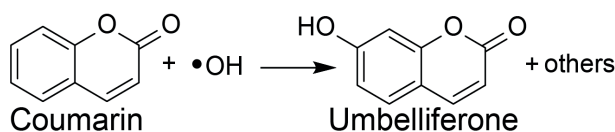


**Figure 6.8** – Fluorescence probe reaction used to detect hydroxyl radicals.

The occurrence of this pathway can be detected by using a fluorescence probe technique,<sup>17,18</sup> wherein coumarin reacts with hydroxyl radicals to produce a new compound (umbelliferone, see figure 6.8) quantifiable by photoluminescence spectroscopy.

To demonstrate the production of the hydroxyl radical by BBL, a solution of 0.1 mM coumarin in buffered electrolyte (figure 6.9). Amperometry measurement was performed in the three electrode cell configuration by applying 1.23 V<sub>RHE</sub> under simulated solar illumination for 1 and 2 hours. The electrolyte was directly collected and its photoluminescence was measured with excitation at 332 nm and emission scan speed of 100 nm · min<sup>-1</sup>. The average of 5 scans was taken for the results. Calibration can be seen in figure 6.17.

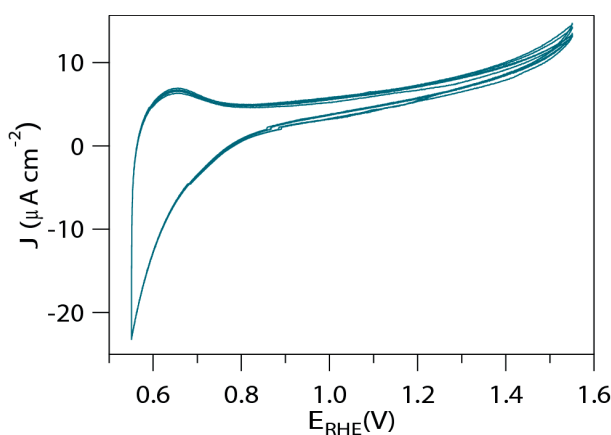


**Figure 6.9** – CV of a spray coated BBL film in aqueous electrolyte (0.5 M Na<sub>2</sub>SO<sub>4</sub> + 0.09 M KH<sub>2</sub>PO<sub>4</sub> + 0.01 M K<sub>2</sub>HPO<sub>4</sub>, pH 7) containing 4 mM of coumarin.

We note that the direct electrochemical oxidation of the coumarin by the BBL was not observed by CV measurement, see figure 6.9, and is anyway unlikely to lead to umbelliferone production as the direct electrochemical oxidation of coumarin has been reported to be irreversible and results in an insoluble deposit on glassy carbon electrodes.<sup>19</sup>

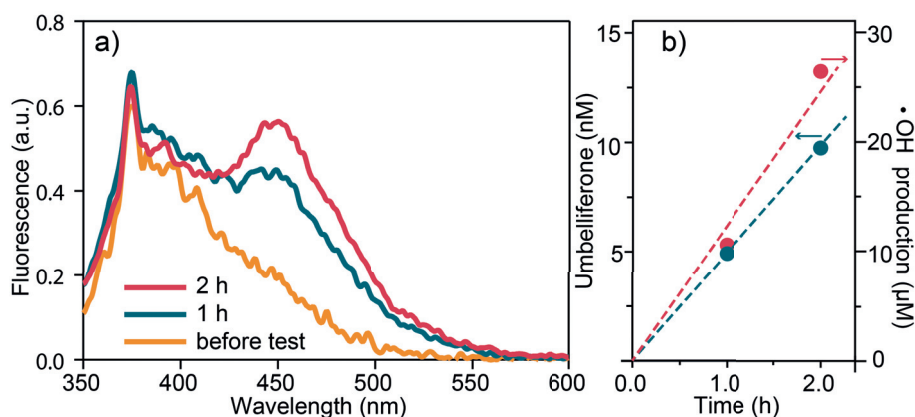


**Figure 6.10** – a) fluorescence spectra of buffered sulfate/phosphate aqueous electrolyte (pH 7) containing 0.1 mM coumarin (before test) and after the PEC experiment at  $1.23 V_{\text{RHE}}$  for 1 and 2 h and b) comparison of the hydroxyl radical concentration estimated by the fluorescence probe to the calculated concentration from the photocurrent density.

The photoluminescence spectra of the original electrolyte and after one or 2 h under photo-electrochemical operation with BBL are shown in figure 6.10 a), where peaks for coumarin at 374 nm and for umbelliferone in the electrolyte was estimated using a calibration curve (figure 6.17) without baseline correction, and is compared to the maximum amount of  $\bullet\text{OH}$  that could have been produced (based on the integrated  $J_{\text{ph}}$ , and assuming 100 % Faradaic efficiency in figure 6.10 b).

While the concentrations differ in magnitude significantly due to the low expected yield of the coumarin reaction<sup>17</sup> and other potential factors decreasing the umbelliferone production,<sup>20</sup> the rate of increase in the concentrations indicates a direct linear relation suggesting that the production of umbelliferone is correlated to the photocurrent and supporting the notion that the bare BBL produces the hydroxyl radical through photo-oxidation.

We note that in addition to the production of  $\bullet\text{OH}$  via  $\text{H}_2\text{O}_2$ , other routes are possible. The direct one-electron production of the hydroxyl radical from the hydroxyl anion may also be feasible at high pH as the standard redox potential for the  $^-\text{OH}/\bullet\text{OH}$  couple is reported at  $+1.8 V_{\text{NHE}}$  (which correspond to  $+2.6 V_{\text{RHE}}$ ).<sup>21,22</sup> In contrast, the direct one-electron oxidation of  $\text{H}_2\text{O}$  to form  $\bullet\text{OH}$  and  $\text{H}^+$  is not expected to be thermodynamically feasible ( $E = +2.9 V_{\text{RHE}}$ ) given the HOMO level of BBL at any obtainable pH.

Regardless of the origin of the  $\bullet\text{OH}$ , its production, instead of molecular  $\text{O}_2$  via the four-electron OER, is consistent with the lack of defined catalytic center on the bare BBL.

## 6.6 Oxygen Production

Given the demonstrated photoelectrochemical stability of the bare BBL photoanode and the thermodynamic suitability for water oxidation we next sought to show  $O_2$  production by applying an appropriate co-catalyst overlayer.

Attempts to directly attach an OER catalyst to the BBL did not result in sustained  $O_2$  production, likely due to poor semiconductor/catalyst attachment. However, when the BBL was pretreated with a sufficiently thin layer of  $TiO_2$  ( $\sim 1$  nm) to act as a tunnel junction, a suitable surface could be obtained (figure 6.11) that allowed successful attachment of a nickel-cobalt catalyst.<sup>23</sup>

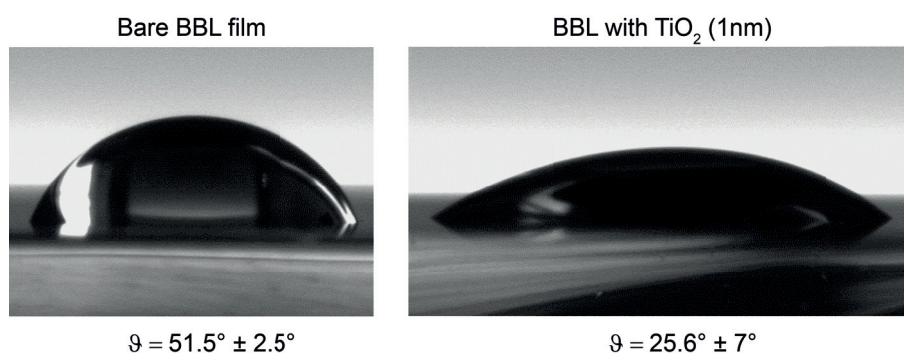


**Figure 6.11** – Average contact angle of a sessile water drop on a bare spray coated BBL film and on a BBL film coated with  $TiO_2$  (ca. 1 nm via ALD).

LSV data are shown in figure 6.12 for the film before and after the  $TiO_2$  and with the co-catalyst. Application of the  $TiO_2$  did not significantly change the observed  $J_{ph}$  ( $\sim 15 - 20 \mu A \cdot cm^{-2}$ ), however a slight increase (to  $\sim 30 \mu A \cdot cm^{-2}$ ) was observed upon the application of the co-catalyst layer. Photocurrent transient spikes remain at all conditions.

Nevertheless, gas chromatography confirmed molecular  $O_2$  production at a rate of  $20 \pm 2 \text{ nmol} \cdot \text{h}^{-1}$  during a constant-illumination chronoamperometry measurement when a steady-state  $J_{ph}$  of  $10.3 \pm 0.1 \mu A \cdot cm^{-2}$  was produced corresponding to a Faradaic efficiency of  $82 \pm 16 \%$  (similar to the value obtained with a related system<sup>24</sup>).

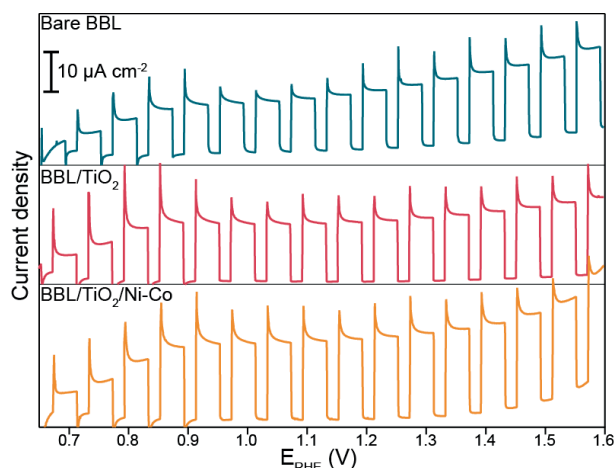


**Figure 6.12** – J-V of a spray coated film of BBL (230 nm thickness) in aqueous electrolyte (0.5 M  $\text{Na}_2\text{SO}_4$  + 0.09 M  $\text{KH}_2\text{PO}_4$  + 0.01 M  $\text{K}_2\text{HPO}_4$ , pH 7) under intermittent (simulated solar) illumination (substrate side illumination) before and after  $\text{TiO}_2$  deposition, and after the co-catalyst deposition.

Overall the similar onset behavior and  $J_{\text{ph}}$  observed with the overlayer present, compared to the bare film in sacrificial and nonsacrificial electrolytes, suggests that the charge separation in the semiconductor layer is kinetically limited by interface exciton dissociation<sup>25</sup> and thus ultimately controlled by the driving force as previously discussed.

The use of a solid-state semiconductor heterojunction or other overlayers specifically designed to enhance free charge generation is a reasonable strategy to increase the photocurrent in BBL electrodes, and efforts in this direction are underway in our laboratory.

## 6.7 Conclusion

In summary, our investigation of BBL as a photoanode for solar water oxidation reveals a strong dependence of the sacrificial photocurrent density on the morphology of the film consistent with a limitation in excited-state transport to the SCLJ.

Electrochemical impedance spectroscopy showed that the driving force for water oxidation could be tuned with electrolyte pH and suggested that water oxidation is thermodynamically feasible.

Furthermore, for the first time, a  $\pi$ -conjugated organic semiconductor demonstrated sustained direct solar water oxidation. The water oxidation photocurrent density was found to increase with increasing pH, and no evidence of semiconductor oxidation was found over testing time on the order of hours with bare BBL films.

$\text{H}_2\text{O}_2$  or hydroxyl radical production proceeds, instead of molecular  $\text{O}_2$  evolution, on bare BBL likely due to the lack of catalytic sites. Notably the produced  $\bullet\text{OH}$  could be employed to

degrade organic pollutants in wastewater.<sup>26</sup>

While molecular  $O_2$  evolution was measured upon functionalization with a Ni-Co catalyst, the smaller photocurrents observed for water oxidation, compared to the sacrificial case, suggest a limitation in charge separation, which is related to the driving force for charge injection into the electrolyte.

Overall this demonstration suggests that robust n-type conjugated organic semiconductors are suitable for direct PEC water oxidation and opens a new path for the rational design and optimization of photoanodes for solar water splitting.

### 6.8 Additional figures

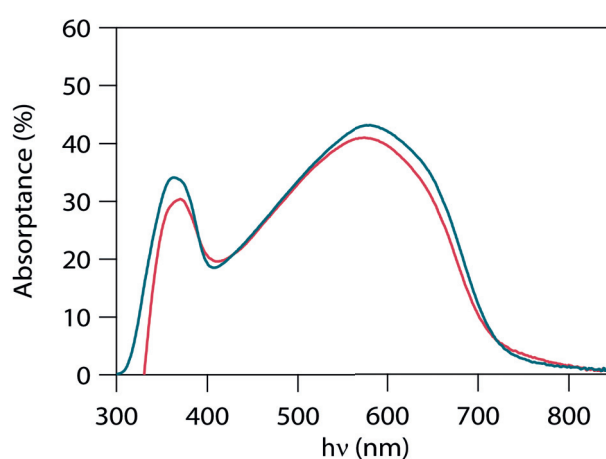


**Figure 6.13** – Absorbance spectra of a dip coated film (red line) and a spray-coated film (blue line) prepared with similar thickness.

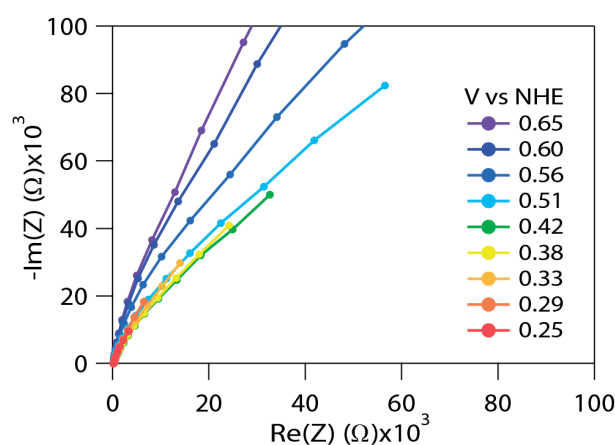


**Figure 6.14** – Nyquist plots (from 100 mHz to 200 kHz) of a spray-coated BBL electrode (in dark condition) in aqueous electrolyte ( $0.5\text{ M Na}_2\text{SO}_4 + 0.09\text{ M KH}_2\text{PO}_4 + 0.01\text{ M K}_2\text{HPO}_4$ , pH 7).



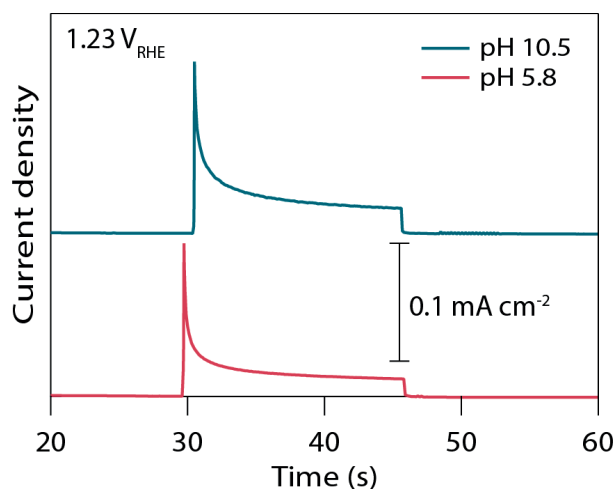


**Figure 6.15** – Photocurrent transient measurements of the spray coated BBL electrode at the indicated pH (aqueous 0.5 M Na<sub>2</sub>SO<sub>4</sub> + 0.09 M KH<sub>2</sub>PO<sub>4</sub> + 0.01 M K<sub>2</sub>HPO<sub>4</sub>, pH adjusted with 1 M NaOH or 1 M H<sub>2</sub>SO<sub>4</sub>) and applied potential. The steady-state photocurrent was determined as the dark current minus the photocurrent at the point where the illumination was terminated (46 sec).

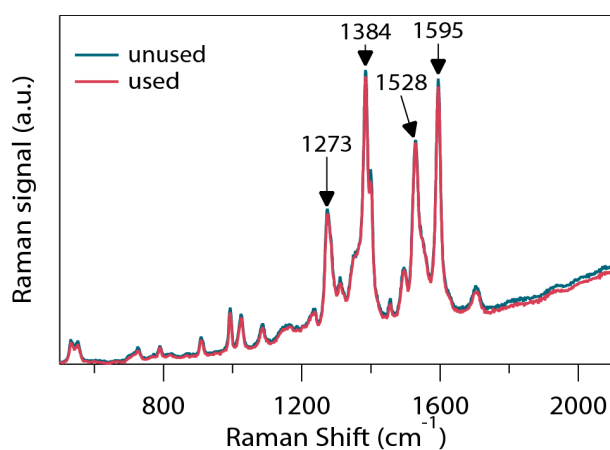


**Figure 6.16** – Raman spectra of a bare (without catalyst overlayers) BBL spray coated film before (blue) and after (red) electrochemical testing at 1.23 V<sub>RHE</sub> for 3 hours in aqueous electrolyte (0.5 M Na<sub>2</sub>SO<sub>4</sub> + 0.09 M KH<sub>2</sub>PO<sub>4</sub> + 0.01 M K<sub>2</sub>HPO<sub>4</sub>, pH 7) under 1 sun illumination.

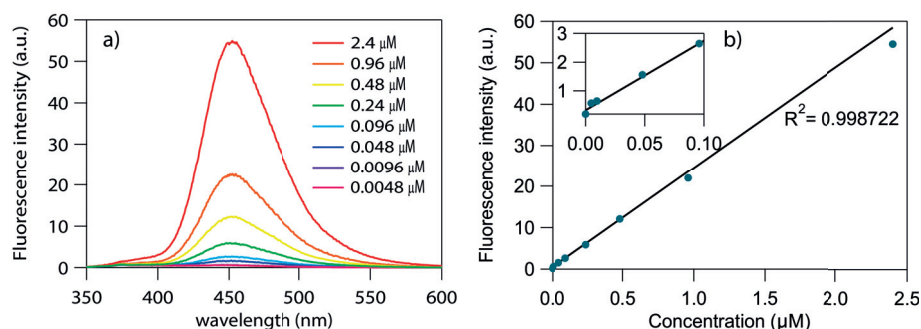


**Figure 6.17** – a) fluorescence spectrum of aqueous electrolyte (0.5 M  $\text{Na}_2\text{SO}_4$  + 0.09 M  $\text{KH}_2\text{PO}_4$  + 0.01 M  $\text{K}_2\text{HPO}_4$ , pH 7) containing different concentrations of umbelliferone, b) and calibration of umbelliferone fluorescence at 450 nm as a function of its concentration, and zoom for low concentrations (inset).

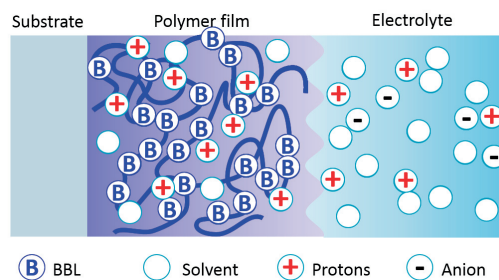
## References

- [2] Jason D. A. Lin, Oleksandr V. Mikhnenko, Jingrun Chen, Zarifi Masri, Arvydas Ruseckas, Alexander Mikhailovsky, Reilly P. Raab, Jianhua Liu, Paul W. M. Blom, Maria Antonietta Loi, Carlos J. Garcia-Cervera, Ifor D. W. Samuel, and Thuc-Quyen Nguyen. “Systematic Study of Exciton Diffusion Length in Organic Semiconductors by Six Experimental Methods”. *Materials Horizons* 1 (2 2014), pp. 280–285. DOI: 10.1039/C3MH00089C.
- [3] Samson A. Jenekhe and Paul O. Johnson. “Complexation-Mediated Solubilization and Processing of Rigid-Chain and Ladder Polymers in Aprotic Organic Solvents”. *Macromolecules* 23 (1990), pp. 4419–4429. DOI: 10.1021/ma00222a015.
- [4] Silvia Janietz and Dessislava Sainova. “Significant Improvement of the Processability of Ladder-Type Polymers by Using Aqueous Colloidal Dispersions”. *Macromolecular Rapid Communications* 27 (2006), pp. 943–947. DOI: 10.1002/marc.200600045.
- [5] Alejandro L. Briseno, Stefan C. B. Mannsfeld, Patrick J. Shamberger, Fumio S. Ohuchi, Zhenan Bao, Samson A. Jenekhe, and Younan Xia. “Self-Assembly, Molecular Packing, and Electron Transport in n-Type Polymer Semiconductor Nanobelts”. *Chemistry of Materials* 20 (2008), pp. 4712–4719. DOI: 10.1021/cm8010265.
- [6] David M. Stanbury. “Reduction Potentials Involving Inorganic Free Radicals in Aqueous Solution”. *Advances in Inorganic Chemistry*. Ed. by A.G. Sykes. Vol. 33. Advances in Inorganic Chemistry. Academic Press, 1989, p. 70. DOI: 10.1016/S0898-8838(08)60194-4.
- [7] Iván Mora-Seró, Francisco Fabregat-Santiago, Benjamin Denier, Juan Bisquert, Ramón Tena-Zaera, Jamil Elias, and Claude Lévy-Clément. “Determination of Carrier Density of ZnO Nanowires by Electrochemical Techniques”. *Applied Physics Letters* 89, 203117 (2006), p. 203117. DOI: 10.1063/1.2390667.

- 
- [8] Jeffrey M. Bolts and Mark S. Wrighton. "Correlation of Photocurrent-voltage Curves with Flat-band Potential for Stable Photoelectrodes for the Photoelectrolysis of Water". *The Journal of Physical Chemistry* 80 (1976), pp. 2641–2645. DOI: 10.1021/j100565a004.
- [9] M. A. Butler and D. S. Ginley. "Prediction of Flatband Potentials at Semiconductor-Electrolyte Interfaces from Atomic Electronegativities". *Journal of The Electrochemical Society* 125(2) (1978), pp. 228–232. DOI: 10.1149/1.2131419.
- [10] K. Wilbourn and Royce W. Murray. "The Electrochemical Doping Reactions of the Conducting Ladder Polymer Benzimidazobenzophenanthroline (BBL)". *Macromolecules* 21 (1988), pp. 89–96. DOI: 10.1021/ma00179a019.
- [11] K. Wilbourn and Royce W. Murray. "The D.C. Redox Versus Electronic Conductivity of the Ladder Polymer Poly(benzimidazobenzophenanthroline)". *The Journal of Physical Chemistry* 92 (1988), pp. 3642–3648. DOI: 10.1021/j100323a062.
- [12] Amit Babel and Samson A. Jenekhe. "High Electron Mobility in Ladder Polymer Field-Effect Transistors". *Journal of the American Chemical Society* 125 (2003), pp. 13656–13657. DOI: 10.1021/ja0371810.
- [13] Thomas J. K. Brenner, Yana Vaynzof, Zhe Li, Dinesh Kabra, Richard H. Friend, and Christopher R. McNeill. "White-light Bias External Quantum Efficiency Measurements of Standard and Inverted P3HT:PCBM Photovoltaic Cells". *Journal of Physics D: Applied Physics* 45 (2012), p. 415101. DOI: 10.1088/0022-3727/45/41/415101.
- [14] Mathieu S. Prévot, Néstor Guijarro, and Kevin Sivula. "Enhancing the Performance of a Robust Sol-Gel-Processed p-Type Delafossite  $\text{CuFeO}_2$  Photocathode for Solar Water Reduction". *ChemSusChem* 8 (2015), pp. 1359–1367. DOI: 10.1002/cssc.201403146.
- [15] Yuji Ando and Tadayoshi Tanaka. "Proposal for a New System for Simultaneous Production of Hydrogen and Hydrogen Peroxide by Water Electrolysis". *International Journal of Hydrogen Energy* 29 (2004), pp. 1349–1354. DOI: 10.1016/j.ijhydene.2004.02.001.
- [16] Xunyu Lu, Wai-Leung Yim, Bryan H. R. Suryanto, and Chuan Zhao. "Electrocatalytic Oxygen Evolution at Surface-Oxidized Multiwall Carbon Nanotubes". *Journal of the American Chemical Society* 137 (2015), pp. 2901–2907. DOI: 10.1021/ja509879r.
- [17] Nobuaki Ohguri, Atsuko Y. Nosaka, and Yoshio Nosaka. "Detection of OH Radicals Formed at PEFC Electrodes by Means of a Fluorescence Probe". *Electrochemical and Solid-State Letters* 12 (2009), B94–B96. DOI: 10.1149/1.3106184.
- [18] Jie Zhang and Yoshio Nosaka. "Quantitative Detection of OH Radicals for Investigating the Reaction Mechanism of Various Visible-Light  $\text{TiO}_2$  Photocatalysts in Aqueous Suspension". *The Journal of Physical Chemistry C* 117 (2013), pp. 1383–1391. DOI: 10.1021/jp3105166.
- [19] Quansheng Wu and Howard D. Dewald. "Voltammetry of Coumarins". *Electroanalysis* 13 (2001), pp. 45–48. DOI: 10.1002/1521-4109(200101)13:1<45::AID-ELAN45>3.0.CO;2-Y.

- [20] Yukihiro Nakabayashi and Yoshio Nosaka. "OH Radical Formation at Distinct Faces of Rutile  $\text{TiO}_2$  Crystal in the Procedure of Photoelectrochemical Water Oxidation". *The Journal of Physical Chemistry C* 117 (2013), pp. 23832–23839. DOI: 10.1021/jp408244h.
- [21] Donald T. Sawyer and Julian L. Roberts. "Hydroxide Ion: an Effective One-Electron Reducing Agent?" *Accounts of Chemical Research* 21 (1988), pp. 469–476. DOI: 10.1021/ar00156a006.
- [22] W. H. Koppenol and Joel F. Liebman. "The Oxidizing Nature of the Hydroxyl Radical. A Comparison with the Ferryl Ion ( $\text{FeO}_2$ )". *The Journal of Physical Chemistry* 88 (1984), pp. 99–101. DOI: 10.1021/j150645a024.
- [23] Lena Trotochaud, James K. Ranney, Kerisha N. Williams, and Shannon W. Boettcher. "Solution-Cast Metal Oxide Thin Film Electrocatalysts for Oxygen Evolution". *Journal of the American Chemical Society* 134 (2012), pp. 17253–17261. DOI: 10.1021/ja307507a.
- [24] Joel T. Kirner, Jordan J. Stracke, Brian A. Gregg, and Richard G. Finke. "Visible-Light-Assisted Photoelectrochemical Water Oxidation by Thin Films of a Phosphonate-Functionalized Perylene Diimide Plus CoOx Cocatalyst". *ACS Applied Materials & Interfaces* 6 (2014), pp. 13367–13377. DOI: 10.1021/am405598w.
- [25] Brian A. Gregg and Yeong Il Kim. "Redox Polymer Contacts to Molecular Semiconductor Films: Toward Kinetic Control of Interfacial Exciton Dissociation and Electron-Transfer Processes". *The Journal of Physical Chemistry* 98 (1994), pp. 2412–2417. DOI: 10.1021/j100060a031.
- [26] S. Malato, P. Fernández-Ibáñez, M. I. Maldonado, J. Blanco, and W. Gernjak. "Decontamination and Disinfection of Water by Solar Photocatalysis: Recent Overview and Trends". *Catalysis Today* 147 (2009), pp. 1–59. DOI: 10.1016/j.cattod.2009.06.018.

## 7 Characterization of Charge Transport Processes in BBL Photoanodes



Finally, BBL films prepared with the spray coating procedure described in chapter 5 page 67 and demonstrated to be a suitable photoanode material for solar water oxidation in chapter 6 page 79 are extensively characterized.

## 7.1 Motivation

Polymeric modified electrodes have been classified into two categories depending on their charge transport processes.<sup>1</sup> Redox polymers transport electrons by hopping, through switching of spatially localized redox center while electronic polymers have the possibility to delocalize electrons along their highly conjugated molecular structure and therefore transport electrons with a metallic-like or semiconducting behavior.

Due to its ladder conjugated backbone, BBL should, in principle, be able to allow electron delocalization. DFT calculation showed that upon light excitation, exciton can be delocalized over six monomer units<sup>2</sup> and current measurement detected a metallic (ohmic) behavior in dry state.<sup>3</sup> However in wet state, BBL has always been described as a redox conductor.<sup>3,4</sup>

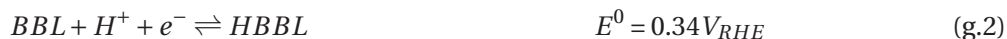
The demonstration in the previous chapters of a sustained photoelectrochemical oxidation reaction with BBL, in chapter 6 page 79, that was dependent on the pH and potential suggested that this polymer could switch between redox and semiconducting transport regimes. It led us to its complete characterization of charge transport in wet conditions (water splitting conditions). For that, Cyclic Voltammetry (CV), Electrochemical Quartz Crystal Microbalance (EQCM), Electrochemical Impedance Spectroscopy (EIS), conductivity and Linear Sweep Voltammetry (LSV) measurements were conducted in different electrolytes, see table C.1 and C.3 page 46.

BBL films used in this chapter were prepared by spray coating method as described in chapter 5 page 67. Two different thicknesses were used: a sample named 230 nm corresponding to one layer deposition (0.5 mL) and a sample named 470 nm corresponding to two layers deposition (1 mL).

## 7.2 Cyclic Voltammetry (CV)

To understand the behavior of BBL electrodes in direct contact with an electrolyte, CV was conducted in 1 M NaClO<sub>4</sub> aqueous electrolyte at various pH, see figure 7.1 a). Two reversible and reproducible reduction peaks are observed at 0.02 V<sub>NHE</sub> and -0.59 V<sub>NHE</sub> for all pH.

Wilbourn and Murray<sup>3,5</sup> already measured the CV of BBL in (Bu<sub>4</sub>N)<sub>2</sub>SO<sub>4</sub> aqueous electrolyte and proposed the following reactions:



While these reactions were observed up to pH 4, two other reversible reduction peaks were

also observed at pH 7 to 12 at  $-0.15 V_{\text{NHE}}$ , reduction g.4, and  $-0.6 V_{\text{NHE}}$ , reduction g.5, which were independent of pH.

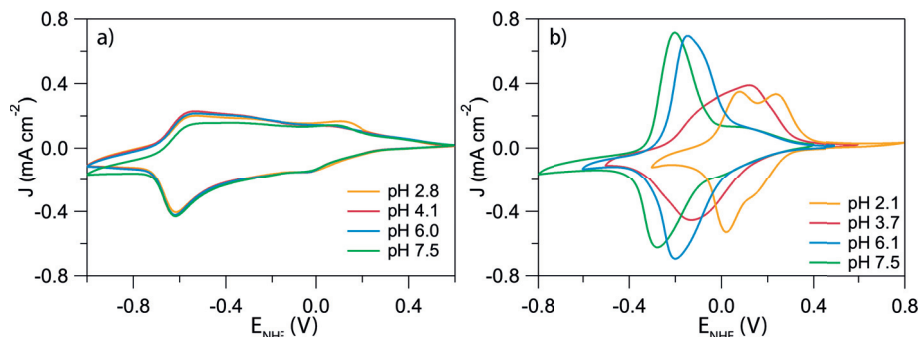


**Figure 7.1** – CV at  $5 \text{ mV} \cdot \text{s}^{-1}$  of a BBL spray coated photoanode of 230 nm in a)  $1 \text{ M NaClO}_4$  at pH 2.8 (yellow), 4.1 (red), 6.0 (blue) and 7.5 (green) and in b)  $0.5 \text{ M NaSO}_4 + 0.09 \text{ M KH}_2\text{PO}_4 + 0.01 \text{ M K}_2\text{HPO}_4$  at pH 2.1 (yellow), 3.7 (red), 6.1 (blue) and 7.0 (green)

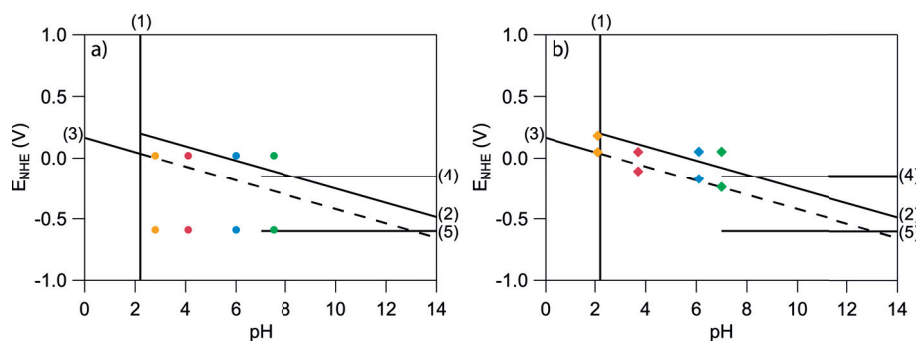


**Figure 7.2** – Pourbaix diagram representing reactions described by Wilbourn and Murray<sup>3,5</sup> and measured half-wave potential in a)  $1 \text{ M NaClO}_4$  and b)  $0.5 \text{ M NaSO}_4 + 0.09 \text{ M KH}_2\text{PO}_4 + 0.01 \text{ M K}_2\text{HPO}_4$ .

Comparing this previous data to our results, as reported in figure 7.2 a), we can exclude reduction g.2 and g.3 since their potential should depend on electrolyte pH. Considering some potential shift due to different testing conditions, we may be in the presence of reduction g.4 and g.5. These two reduction pathways were also measured in  $1 \text{ M Na}_2\text{SO}_4$ , see figure 7.14, and reported in acetonitrile.<sup>3,6</sup>

A similar analysis was conducted in  $1 \text{ M Na}_2\text{SO}_4$  with a phosphate buffer at various pH, see figure 7.1 b). Again two reversible and reproducible reduction peaks are observed at pH 2.1, 3.7, 6.1 and 7.0. Only two peaks at pH 2.1 and 3.7 follow reactions g.2 and g.3 potential as seen in figure 7.2 b). While at pH 6.1 and 7.0 the first peak is located at the same potential and the second lies on the reduction reaction described by g.3. We note that, for reaction g.3 to happen, the BBL should be in its protonated form which is possible only up to pH 4.

The effect of electrolyte is hence significant on the electrochemical behavior of BBL. In the pH range between 2.1 and 7.5, in one case the BBL can be reduced by two electron transfer reactions. Taking into account the pKa of 2.2, we may expect another reduction pathway at pH lower than 2.2\*. In the second case the BBL can be reduced first by a one electron transfer and secondly by a proton-couple electron transfer. This last reaction, following reaction g.3 can only be possible if the BBL is in a protonated form indicating another chemical species or protonation site than the one with a pKa of 2.2 (imine site<sup>5</sup>).

### 7.3 Electrochemical Quartz Crystal Microbalance (EQCM)

To verify the effect of electrolyte on the BBL electrode, EQCM measurement was conducted. EQCM was recorded during CV at  $5 \text{ mV} \cdot \text{s}^{-1}$  between 0 and  $1 \text{ V}_{\text{NHE}}$  on BBL sample of 230 nm and 470 nm thickness and on the bare gold sensor. An electrochemistry module was used containing a platinum counter electrode and an Ag/AgCl (KCl 3 M) reference electrode. For all cases, 3 cycles starting at  $0 \text{ V}_{\text{NHE}}$  were recorded, only two last are shown in graphics. Electrolyte used are listed in table C.3 page 46.

Between each measurement, BBL films were dipped into  $\text{HNO}_3$  0.5 M during 1 hour, washed with Milli-Q water and dried at  $250^\circ\text{C}$  10 minutes. Measurements were also recorded onto bare gold sensor. They were washed between measurements following the cleaning procedure for the gold sensor described section 2.7 page 28. Baseline correction was done on all curves.

In all cases, the gold sensor measurement corresponds to no mass change or small mass change compared to the 230 nm and 470 nm thick BBL samples. The mass change is also greater for the 470 nm sample compare to the 230 nm one. This indicates that mass changes recorded are only due to the BBL film.

In  $\text{NaClO}_4$  0.1 M electrolyte at pH 7.4, see figure 7.3, starting at  $0 \text{ V}_{\text{NHE}}$ , the BBL film first is oxidized leading to a small increase of mass followed by a more significant decrease of mass from  $0.05 \text{ V}_{\text{NHE}}$  to  $0.3 \text{ V}_{\text{NHE}}$ . Then the current stabilizes in a plateau where the mass decreases at a slower rate. During the reverse scan, the same plateau region with small change of mass appears until  $0.2 \text{ V}_{\text{NHE}}$  where the BBL starts to be reduced leading to mass increase. Since mass increase and decrease depends on the film potential, it can be associated with intercalation of ionic charges into the BBL film.

---

\* not tested



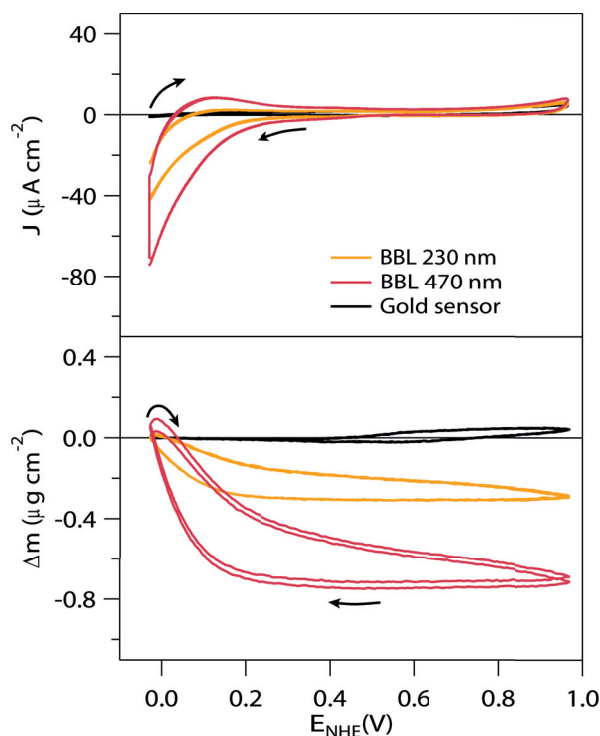


**Figure 7.3** – EQCM data of gold (black) and BBL spray coated photoanode of 230 nm (yellow) and 470 nm (red) thickness in  $\text{NaClO}_4$  0.1 M pH 7.4 aqueous electrolyte. Top graph shows the CV results, bottom graph shows the mass change calculated by the Sauerbrey equation.

Similar observations can be drawn in  $\text{NaClO}_4$  1 M pH 7.4 and  $\text{NaClO}_4$  1 M pH 2.9, see figure 7.15 verifying that the pH of the bulk electrolyte does not influence the redox reaction potential as observed in CV. With higher electrolyte concentration, larger mass loss/gain and current densities are observed.

In order to determine which ions enter the film, ions sizes in electrolyte was changed.<sup>7</sup> We used sodium tetrphenylborate ( $\text{NaTPB}$ ) and tetrabutylammonium chloride ( $\text{TBACl}$ ) to exclude anion intake in the first case and cation intake in the second one, see figure 7.4.  $\text{TBAClO}_4$  could not be used as it is not soluble in water but chloride ion is not oxidized under these conditions as seen in the CV.

In both cases the same behavior is observed as in  $\text{NaClO}_4$  electrolyte namely (i) a small increase followed by a mass loss during oxidation between  $0 V_{\text{NHE}}$  and  $0.3 V_{\text{NHE}}$  (ii) a plateau region between  $0.3 V_{\text{NHE}}$  and  $1 V_{\text{NHE}}$  and (iii) an increase of mass during reduction from  $0.2 V_{\text{NHE}}$  to  $0 V_{\text{NHE}}$ . Both amplitude of mass change and currents density are higher than in the 1 M  $\text{NaClO}_4$  pH 7 case. On the gold sensor, the  $\text{TPB}^-$  anion is oxidized at  $0.7 V_{\text{NHE}}$  but no mass change is observed at the same time. This oxidation wave is absent with the BBL film indicating a good coverage of the gold substrate by the film and no oxidation of the electrolyte on the BBL surface.

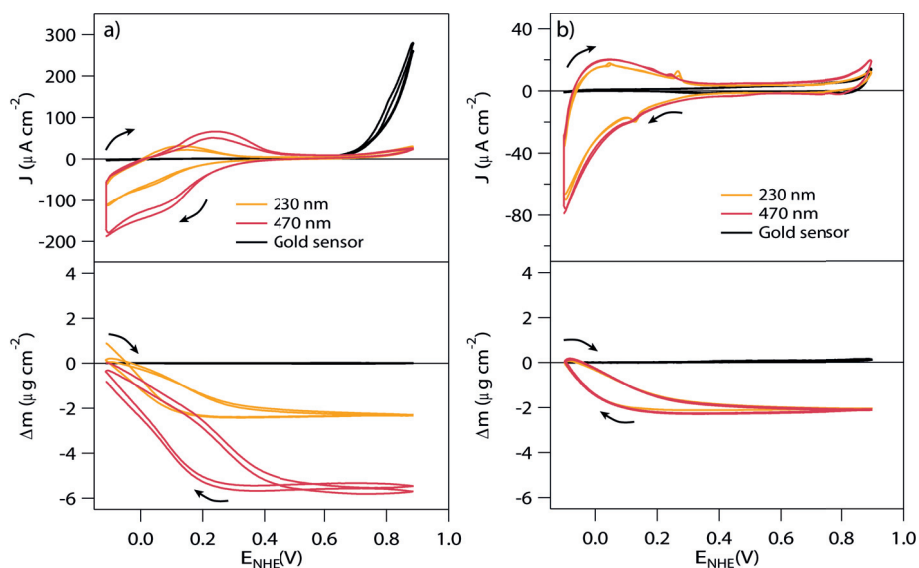


**Figure 7.4** – EQCM data of gold (black) and BBL spray coated photoanode of 230 nm (yellow) and 470 nm (red) thickness in a) NaTPB 0.1 M pH 8.6 and b) TBACl 0.1 M pH 8.6 aqueous electrolyte. Top graphs show the CV results, bottom graphs show the mass change calculated by the Sauerbrey equation.

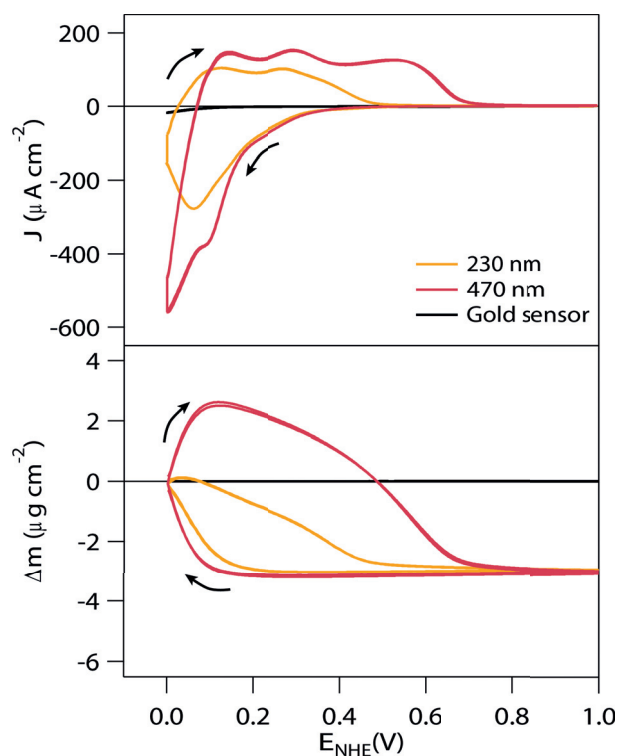


**Figure 7.5** – EQCM data of gold (black) and BBL spray coated photoanode of 230 nm (yellow) and 470 nm (red) thickness in  $HClO_4$  0.1 M pH 0 aqueous electrolyte. Top graph shows the CV results, bottom graph shows the mass change calculated by the Sauerbrey equation.

### 7.3. Electrochemical Quartz Crystal Microbalance (EQCM)

Finally we excluded the effect of sodium ion by using  $\text{HClO}_4$  electrolyte, in figure 7.5.

Again, similar observation can be seen as for the  $\text{NaClO}_4$  case. However, the oxidation peak is separated into three waves ( $0.14 V_{\text{NHE}}$ ,  $0.3 V_{\text{NHE}}$  and  $0.53 V_{\text{NHE}}$ ). It appears more clearly that only the first oxidation wave corresponds to mass increase while the two following correspond to mass loss. The reduction peak has a shoulder at  $0.095 V_{\text{NHE}}$  which corresponds to the mass increase.

During the redox switch of BBL film EQCM measurement shows cation expulsion during oxidation and cation insertion during reduction.<sup>8</sup> This cation insertion could also be coupled with solvent exchange.<sup>9</sup> By wisely choosing cation and anion size, it is possible to determine that neither the  $\text{ClO}_4^-$  anion nor the  $\text{Na}^+$  cation are responsible of the mass change as it occurs also when these ions are not present in the solution. Hence we conclude that ions in the solvent are responsible of the mass change and more specifically  $\text{H}^+$  cations. Measurement in acetonitrile solvent was then done in  $\text{NaClO}_4$  electrolyte, in figure 7.16, showing no reduction of the BBL film and no mass change.

Two contributions could explain the  $\text{H}^+$  insertion: the first one is a proton-couple reduction reaction which would increase the mass of BBL itself. The second one would be  $\text{H}^+$  migration inside the porosity of the film to compensate negative charging of the film which would change the total mass of the film,<sup>8</sup> being the BBL mass and the electrolyte mass contained in the porosity of the film. As the proton-couple reaction was already excluded from the CV analysis, only second case is plausible.

To understand the behavior of the BBL film in contact with the phosphate buffer, QCM measurement was done by replacing the electrolyte from a solution of 0.5 M  $\text{Na}_2\text{SO}_4$  pH 7.5 to 0.5 M  $\text{Na}_2\text{SO}_4$  pH 7.5 with phosphate buffer. The change of mass between two cases was recorded on a BBL film of 230 nm and on a gold sensor to remove the effect of the sensor, see figure 7.6.

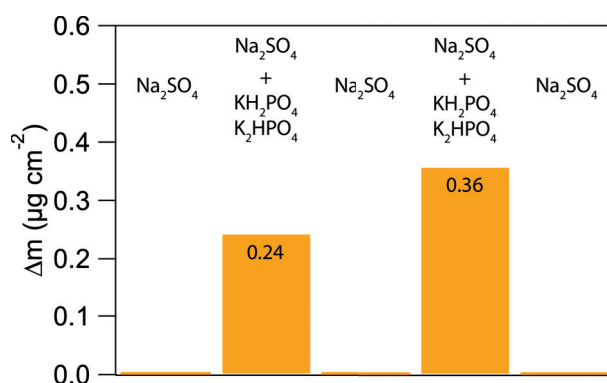


**Figure 7.6** – Results of QCM data obtained by flowing an electrolyte solution on a BBL film of 230 nm. Electrolyte solution was switched between a 0.5 M  $\text{Na}_2\text{SO}_4$  pH 7.5 and a 0.5 M  $\text{Na}_2\text{SO}_4$  + 0.09 M  $\text{KH}_2\text{PO}_4$  + 0.01 M  $\text{K}_2\text{HPO}_4$  pH 7.5 solution twice. Mass change was calculated by the Sauerbrey equation, results are corrected by the effect of the gold sensor.

An average mass increase of  $0.3 \mu\text{g} \cdot \text{cm}^{-2}$  is obtained due to the phosphate buffer which could indicate that phosphate ions adsorb on the BBL surface. Indeed the formation of a complex with  $\text{HPO}_4^{2-}/\text{H}_2\text{PO}_4^-$  could occur and was already observed and reported with polyphosphoric acid.<sup>10</sup> This would explain the protonated-like behavior of the BBL reduction measured in the CV

### 7.4 Electrochemical Impedance Spectroscopy (EIS)

To get a more comprehensive understanding of the effect of ions in the electrochemistry of BBL film, EIS was conducted on BBL electrodes in various electrolytes. Electrochemical Impedance Spectroscopy (EIS) was performed in the dark (or as precised) using a 10 mV amplitude perturbation between 4000 kHz and 30 mHz. Potential were varied between  $0 V_{\text{NHE}}$  and  $1 V_{\text{NHE}}$  always starting from  $1 V_{\text{NHE}}$  in the reduction direction. Electrolyte used are listed in tables C.1 and C.3 page 46, purging them by  $\text{O}_2$  or Ar, or changing their concentration was found to have no influence on the results.

In all cases, two processes are observed: a first one at high frequency (from 1 Hz to 100 kHz) and a second one at lower frequency (from 0.03 Hz to 1 Hz). Everything occurring at higher frequency than 100 kHz is due to counter electrode / electrolyte charge transfer and was included in the series resistance  $R_s$ . Both processes appear to be well separated, i.e. occurring at different frequencies, at low applied potential (from  $0 V_{\text{NHE}}$  to  $0.2 V_{\text{NHE}}$ ), superimposed between  $0.2 V_{\text{NHE}}$  to  $0.6 V_{\text{NHE}}$  and again separated at higher potential. To fit the data, ZView2 software was used with equivalent circuit in figure 7.7 a). A Constant Phase Element (CPE) was used instead of a capacitance element to take into account the non-ideal behavior of data. True capacitance  $C$  was calculated from the CPE element using equation g.6 with  $R$  the resistance,  $Q$  the CPE capacitance and  $n_{\text{CPE}}$  the CPE exponent.

$$C = \frac{(R \cdot Q)^{1/n_{\text{CPE}}}}{R} \quad (\text{g.6})$$

Fitting was realized ensuring that the CPE1/ $R_1$  semicircle would always correspond to the high frequency process and the CPE2/ $R_2$  semicircle to the low frequency process. In  $\text{Na}_2\text{SO}_4$  with phosphate buffer, the two processes were more difficult to distinguish therefore a simple Randle's circuit was used, figure 7.7 b). For the fitting, the CPE exponent was left free if found between 0.8 and 1 or fixed at 0.8 if lower.

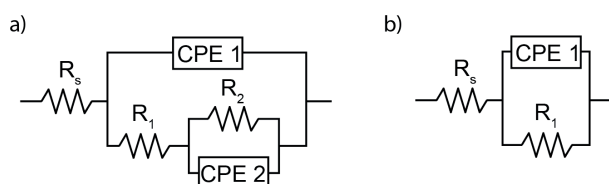


**Figure 7.7** – Equivalent circuits used to fit data in a)  $\text{NaClO}_4$  and b)  $\text{Na}_2\text{SO}_4$  with phosphate buffer.

#### 7.4. Electrochemical Impedance Spectroscopy (EIS)

No diffusion-like behavior, corresponding to a slope of  $-0.5$  in the  $|Z|$  vs freq. plot and a phase of  $-45^\circ$ , was observed in the data. An example of a bode plot is shown in figure 7.17 where the corresponding slopes in the  $|Z|$  vs freq. plot are  $-0.92$  and  $-0.86$  at  $0 V_{NHE}$  and  $0.9 V_{NHE}$  respectively.

In  $1 M NaClO_4$  pH 7, the process at high frequency corresponds to a capacitance around  $20 \mu F \cdot cm^{-2}$  which remains constant over the tested applied potential. The resistance in parallel with this capacitance varies from  $1 \Omega \cdot cm^{-2}$  at  $0 V_{NHE}$  to  $1 \times 10^5 \Omega \cdot cm^{-2}$  at  $0.4 V_{NHE}$  and then stays constant for more anodic potentials.

At low frequency, the process behaves differently: the capacitance is changing from  $20 mF \cdot cm^{-2}$  (out of the graph) at  $0 V_{NHE}$  to  $1 \times 10^{-5} mF \cdot cm^{-2}$  at  $0.6 V_{NHE}$  and stays constant until  $1 V_{NHE}$ . The resistance related to this process shows an overall increase from  $1 \times 10^5 \Omega \cdot cm^{-2}$  at  $0 V_{NHE}$  to  $1 \times 10^6 \Omega \cdot cm^{-2}$  at  $1 V_{NHE}$ .

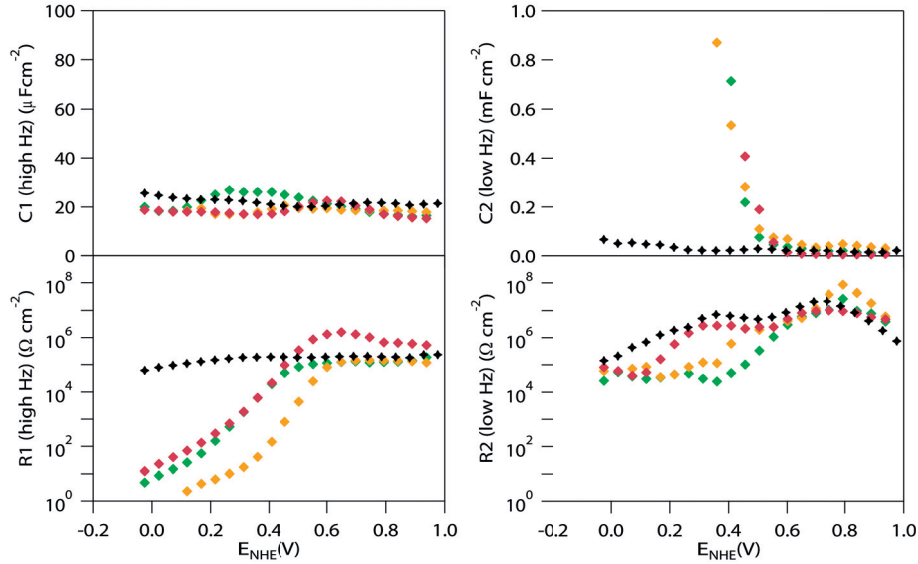


**Figure 7.8** – Results from the fitting of EIS data of FTO (black) and spray coated BBL photoanode of 110 nm (yellow), 230 nm (red) and 470 nm (green) thickness in  $NaClO_4$  1 M pH 7.4.

The first process can be attributed to polymer bulk electron transfer.<sup>11</sup> It is a fast charge transfer, happening at high frequency. Its capacitance and resistance change with applied potential correspond to a geometric capacitance and resistance of charge transport.

The capacitance in F should depend on the polymer dielectric constant and the S/l ratio with:

$$C_1 = \epsilon_r \cdot \epsilon_0 \cdot \frac{S}{l} \quad (g.7)$$

where  $\epsilon_r$  and  $\epsilon_0$  are the dielectric constant of the polymer and the vacuum permittivity respectively in  $F \cdot m^{-1}$ , S the surface contact in  $m^2$  and l the thickness of the film in m. None of these

elements are potential dependent which give rise to a constant capacitance.

The resistance in  $\Omega$  however depends on the film conductivity ( $\sigma$  in  $\text{S} \cdot \text{m}^{-1}$ ) with:

$$R_1 = \frac{d}{S \cdot \sigma} \quad (\text{g.8})$$

which can vary depending on the amount of oxidized and reduced species in the film (amount of doping). As seen in figure 7.8,  $R_1$  starts to decrease when the BBL film is reduced. Compared to the CV where the onset of reduction is positioned at  $0.26 \text{ V}_{\text{NHE}}$ , the resistance onset of  $R_1$  showing reduction of the film is in advance of 220 mV, see discussion later. The decrease of  $R_1$  during the reduction means that during n-doping, the conductivity of the BBL film increases.<sup>12</sup>

$R_1$  also depends on the  $l/S$  ratio therefore both capacitance and resistance of this process should scale with the thickness and the surface contact change. In order to determine this ratio, CV at different scan rates were conducted in phosphate buffered electrolyte, see figure 7.18, for film of 110 nm, 230 nm and 470 nm thickness.

In this case, the current amplitude is proportional to the scan rate (relation for an adsorbed species on a conductive electrode without diffusion<sup>13</sup>) hence  $Q$ , the total charge (or area under the curve in  $\text{mA} \cdot \text{V}$ ), is proportional to the scan rate as well. Knowing that:

$$Q = nFSI^* \quad (\text{g.9})$$

where  $n$  is the number of electron exchanged during the reaction,  $F$  is the Faradaic constant,  $S$  is the active surface contact,  $I^*$  is the concentration of adsorbed species on the electrode surface (in  $\text{mol} \cdot \text{cm}^{-2}$ ) that can undergo the redox reaction and  $Q$  taken as the average between the oxidation and reduction wave area,  $SI^*$  was determined by linear regression, see inset graph in figure 7.18 and table G.1.

Comparing this value for different film thicknesses it appears to be twice as high with 230 nm than 110 nm and also twice as high with 470 nm than 230 nm. This implies that a higher molar amount of BBL is in direct contact with the electrolyte when the thickness is increased. Comparing these values with the change in thickness  $d$  we can conclude that due to the porosity of the film, increasing the thickness of the film, increases also the number of BBL species in contact with the electrolyte in the same way (i.e.  $S/d$  is constant). This explains why  $C_1$  and  $R_1$  values don't vary with the film thickness.

The second process at lower frequency can be attributed to an ionic process. It is a slow process, happening at low frequency, and its capacitance and resistance behavior don't match with what is expected for a charge transfer process or trap state process.<sup>14</sup> The occurrence of this second process on the bare FTO substrate with the same  $C_2$  and  $R_2$  values suggests that the process could be the Helmholtz layer at the FTO/electrolyte or BBL/electrolyte interfaces.<sup>15</sup> On BBL electrodes,  $C_2$  shows a large building of charge with a change of 6 order of magnitude during the reduction. This increase starts at  $0.545 \text{ V}_{\text{NHE}}$  (65 mV ahead of  $R_1$ ) for all thicknesses

## 7.4. Electrochemical Impedance Spectroscopy (EIS)

and could correspond to the  $H^+$  intake recorded in EQCM at  $0.2 V_{NHE}$ .

The difference of potential of 380 mV between the two measurements could be explained by the two different time scales. In the EQCM measurement the scan rate of  $5 \text{ mV} \cdot \text{s}^{-1}$  corresponds to a non steady state case where solution in the Helmholtz layer is in low concentration compared to the bulk electrolyte due to the  $H^+$  insertion inside the film. Since potential is changing, the  $H^+$  concentration does not have the time to balance giving rise to a mass transfer limitation. However in EIS, each potential is maintained for 160 seconds during which  $H^+$  concentration has time to reach equilibrium between the Helmholtz layer and the bulk electrolyte. Therefore it is no longer in mass transfer limitation which explains why (i) the reduction of BBL occurs at a more anodic potential and (ii) no diffusion-like behavior is observed in the impedance data, see figure 7.17.

The R2 resistance seems to be stable and independent of the C2 capacitance, showing a stable and high resistance of charge transfer process in the Helmholtz layer.

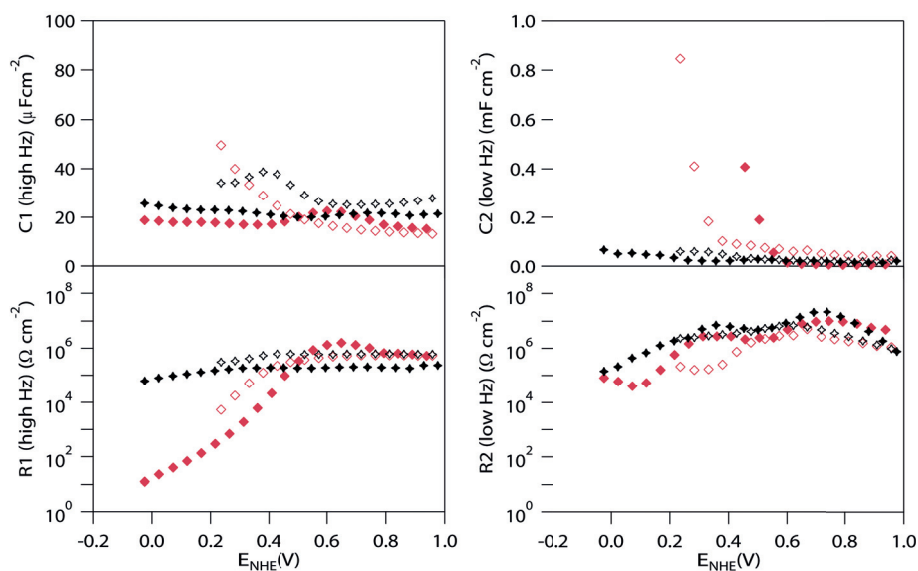


**Figure 7.9** – Results from the fitting of EIS data of FTO in pH 7 (full black) and pH 3 (empty black) electrolyte and spray coated BBL photoanode of 230 nm thickness in pH7 (full red) and pH 3 (empty red) electrolyte. Electrolyte:  $\text{NaClO}_4$  1 M.

EIS was also conducted in 1 M  $\text{NaClO}_4$  at pH 3 where the same behavior as in pH 7 can be seen, in figure 7.9. However we can notice an increase in the geometric capacitance (C1) during BBL reduction at  $0.5 V_{NHE}$  and a small shift in the increase of Helmholtz layer capacitance (C2). This shift cannot be attributed to the change of pH as it would be shifted to the anodic direction. This effect can be explained by the fact that this pH is close to the pKa of BBL therefore a small amount of  $\text{HBBL}^+$  species can be present which would increase the charge of the film (C1) and reduce at the same time the concentration of  $H^+$  at the surface of the film

(C2).

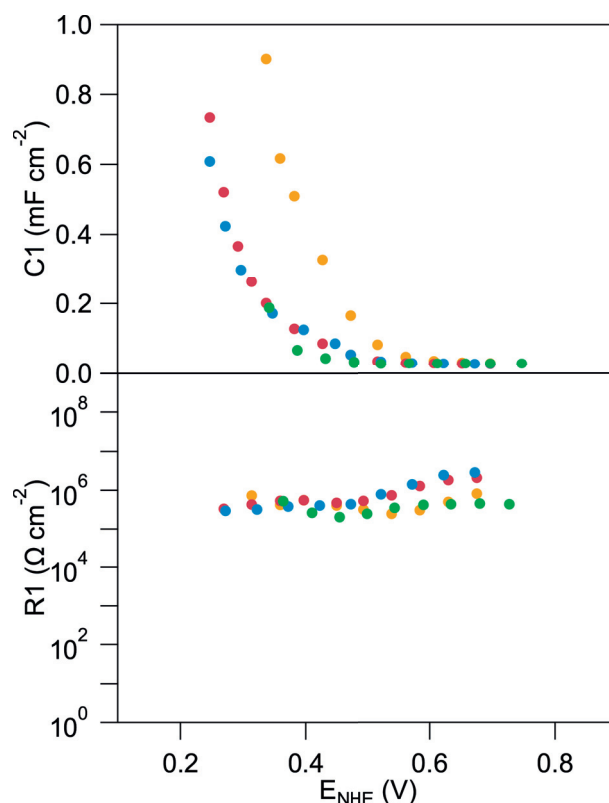


**Figure 7.10** – Results from the fitting of EIS data of a spray coated BBL photoanode of 230 nm thickness in 0.5 M NaSO<sub>4</sub> + 0.09 M KH<sub>2</sub>PO<sub>4</sub> + 0.01 M K<sub>2</sub>HPO<sub>4</sub> pH 2.0 (yellow), 3.7 (red), 6.1 (blue) and 7.0 (green).

EIS was conducted in 1 M Na<sub>2</sub>SO<sub>4</sub> with phosphate buffer electrolyte, in figure 7.10. In this case, both processes are more difficult to distinguish during the fitting therefore a simple Randle circuit was used. Then information about the BBL reduction (small resistance) is lost in the fitting. However the change in the capacitance can still be seen with an increase of capacitance during BBL reduction located at 0.31 V<sub>NHE</sub> for pH 3.7, 6.1 and 7.0. This process then corresponds to the first reduction peak in the CV. A shift is observed at pH 2.0 (to 0.48 V<sub>NHE</sub>) due to the presence of HBBL<sup>+</sup> species. Compared with the electrolyte without phosphate buffer, capacitance values are the same while resistance values are one order of magnitude higher. This could be either due to the fitting procedure or to a lower conductivity of the film.



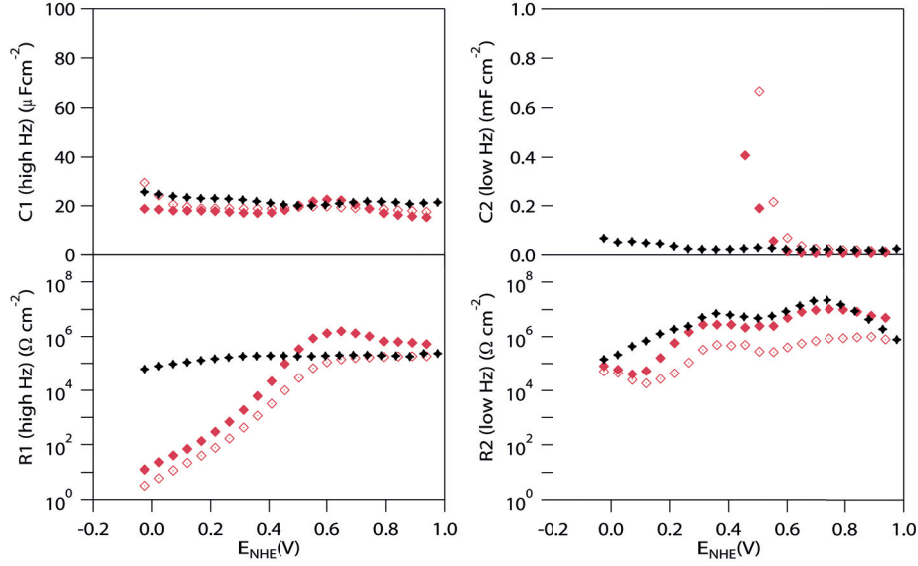


**Figure 7.11** – Results from the fitting of EIS data of FTO (black) and spray coated BBL photoanode of 230 nm thickness (red) in dark (full) and under 1 sun illumination (empty with dot) in  $NaClO_4$  1 M pH 7.4.

To further understand the limitations in BBL photoanodes, EIS was conducted in 1 M  $NaClO_4$  pH 7 under illumination from back side, in figure 7.11. Similar conclusions can be conducted as in dark with a notable decrease of resistance of one order of magnitude in both processes. The resistance of the second process attributed to the Helmholtz layer charge transfer resistance is also reduced because of the enhanced Faradaic reaction at the surface.<sup>15</sup>

## 7.5 Conductivity

Conductivity of a 230 nm thick BBL film was measured in a sandwich-type configuration. In this measurement, the BBL film is confined between a bottom electrode, the FTO substrate, and a porous top electrode, made of silver nanowires. The film is then immersed in the electrolyte and polarized at a potential (same for both electrodes) during 3 min. After this time, the top electrode is stepped cathodically by 5 mV and kept at this voltage during 2 min while the bottom one stays constant at the previous potential. Therefore there will be a difference of potential of 5 mV between the bottom and top electrodes and a current will flow. The conductivity is then calculated with equation g.10 where  $\sigma$  is the conductivity,  $\Delta I$  the difference of current measured at the top electrode before and after the voltage step,  $l$  the film thickness,  $\Delta V$  the difference of potential and  $A$  the geometric surface area.

$$\sigma = \frac{\Delta I \cdot l}{\Delta V \cdot A} \quad (g.10)$$

This measurement was conducted in two electrolytes; 0.1 M  $NaClO_4$  at pH 7.4 and 0.5 M  $NaSO_4$  + 0.09 M  $KH_2PO_4$  + 0.01 M  $K_2HPO_4$  at pH 7, in dark and under 1 sun illumination.

As seen in figure 7.12, in all cases the conductivity starts to increase at  $0.2 V_{\text{NHE}}$  in the reduction direction<sup>†</sup>. This corresponds well with the previous measurement with the starting of reduction at this potential. This increase of conductivity was explained by the presence of the protonated BBL species which is more conductive.<sup>3</sup> In our case, as already mentioned, at this pH the protonated BBL as unlikely to be present, at least in the  $\text{NaClO}_4$  electrolyte.

This effect could rather be explained by a change of conduction type; in the reduced case, the BBL is charged negatively which enhances the insertion of solvent and ions around the polymer. Then the charge conduction might be driven by electron hopping mechanism through spatially localized redox center.<sup>4,5</sup> In the oxidized case, the BBL cannot support any localized charge and all solvent and ions are removed from the film. Normally, this would switch the polymer to an insulator state. However, due to its ladder-type backbone, BBL behaves like a semiconductor and can still transport charges by delocalization of electrons as in its dry state.<sup>3</sup>

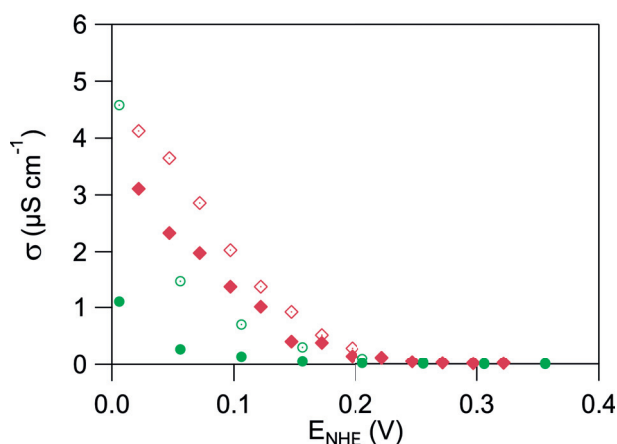


**Figure 7.12** – Conductivity of a BBL spray coated photoanode of 230 nm in 1 M  $\text{NaClO}_4$  pH 7.4 (red square) and in 0.5 M  $\text{Na}_2\text{SO}_4$  + 0.09 M  $\text{KH}_2\text{PO}_4$  + 0.01 M  $\text{K}_2\text{HPO}_4$  pH 7.0 (green circle) in dark (full) and under 1 sun illumination (empty with dot).

We can also note that the conductivity of the film is always higher under illumination and higher in the  $\text{NaClO}_4$  electrolyte which correlates with the reduced resistance measured in EIS.

### 7.6 Linear Sweep Voltammetry (LSV)

Finally the ability of our BBL photoanode to split water was compared in  $\text{NaClO}_4$  and  $\text{Na}_2\text{SO}_4$  with phosphate buffer electrolytes in LSV under chopped light, in figure 7.13.

<sup>†</sup> corresponding to the published results<sup>3</sup>

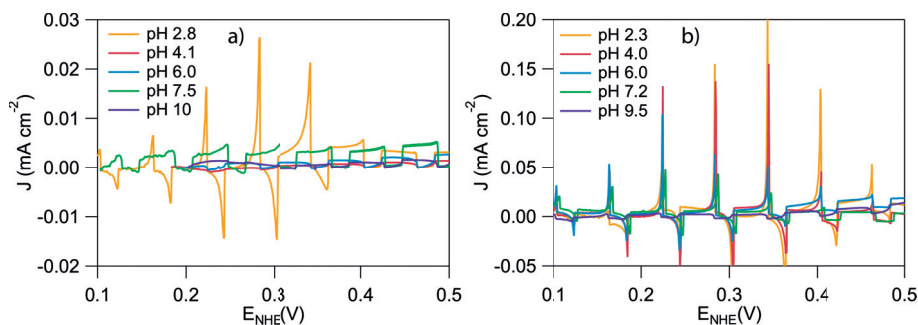


**Figure 7.13** – LSV of a BBL spray coated photoanode of 230 nm under chopped light (1 sun) in a) 1 M  $\text{NaClO}_4$  pH 2.8 (yellow), 4.1 (red), 6.0 (blue), 7.5 (green) and 10.0 (violet) and b) 1 M  $\text{Na}_2\text{SO}_4$  + 0.09 M  $\text{KH}_2\text{PO}_4$  + 0.01 M  $\text{K}_2\text{HPO}_4$  at pH 2.3 (yellow), 4.0 (red), 6.0 (blue) and 7.2 (green) and 9.5 (violet)

In  $\text{NaClO}_4$  electrolyte, transient photocurrent showing charging and discharging of the BBL/electrolyte interface during illumination<sup>15</sup> is observed only at low pH while it is present in all pH in the  $\text{Na}_2\text{SO}_4$  with phosphate buffer electrolyte. This could be associated to the presence of protonated BBL or the BBL/phosphate ions complex.

A poor efficiency, shown by a smaller steady state photocurrent, attributed to OER, is recorded in the  $\text{NaClO}_4$  electrolyte compared to the other one. This shows that the photocurrent more limited in the  $\text{NaClO}_4$  electrolyte. However this effect can not be due to the change of film conductivity as we have shown that it is higher in the  $\text{NaClO}_4$  electrolyte.

We propose that the formation of the complex with the phosphate ions could facilitated charge transport and transfer at the SCLJ. More experiments in sacrificial electrolyte are needed to determine the reason of this limitation.

## 7.7 Conclusions

We showed that charge transport through a spray coated BBL film behave differently depending on the electrolyte used. Compared to metal oxide photoelectrodes where charge transport abilities depends on the oxidation state of the material, in the polymeric case, the polymeric species, influenced by the electrolyte, are more determinant. Therefore a complete characterization of BBL species at the interface is beneficial for the understanding of photoanodes efficiency.

We demonstrated that, whether the film was protonated or not or interacting with the electrolyte by the formation of a complex, efficiency can be limited by different effects. In order to explain the photocurrent measured at potential where the BBL should be in its insulator state (oxidized form) we stated that charge transport through the film occurs by delocalization of charges. While in its reduced state, the BBL behaves as a redox polymer due to the possible film charging. This forms a region between  $0.2 V_{\text{NHE}}$  and  $0.5 V_{\text{NHE}}$  where the BBL change from

a redox polymer charge transport behavior to a delocalized charge transport behavior which gives rise to the onset of photocurrent.

## 7.8 Additional Figures

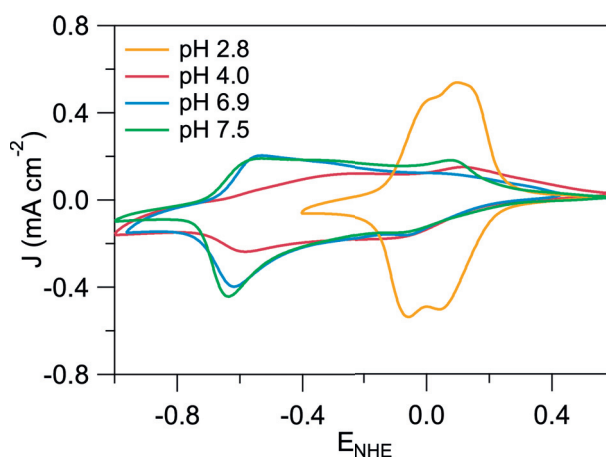


**Figure 7.14** – CV at  $5 \text{ mV} \cdot \text{s}^{-1}$  of a BBL spray coated photoanode of 230 nm in  $1 \text{ M Na}_2\text{SO}_4$  at pH 2.8 (yellow), 4.0 (red), 6.9 (blue) and 7.5 (green)

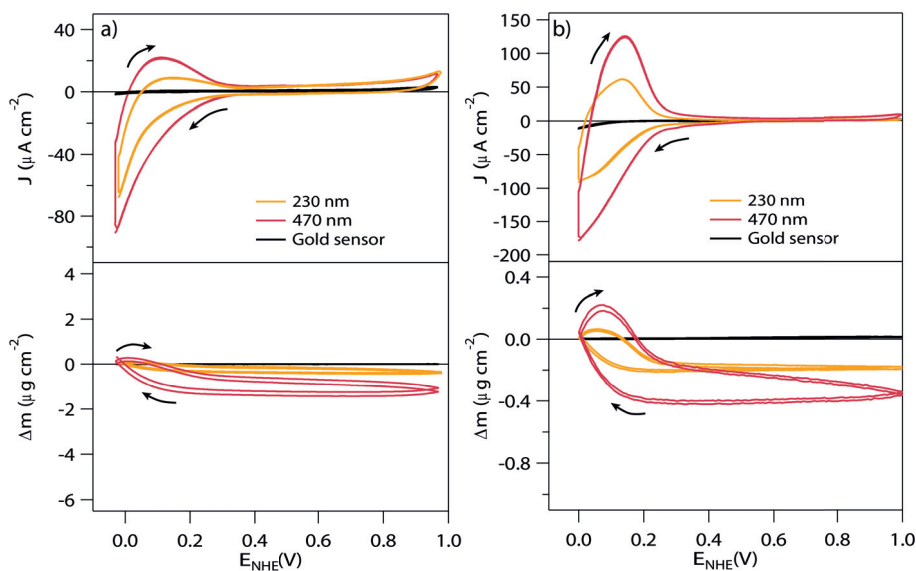


**Figure 7.15** – EQCM data of gold (black) and BBL spray coated photoanode of 230 nm (yellow) and 470 nm (red) thickness in  $\text{NaClO}_4$  1 M a) pH 7.4 and b) pH 2.9 aqueous electrolyte. Top graphs show the CV results, bottom graphs show the mass change calculated by the Sauerbrey equation.

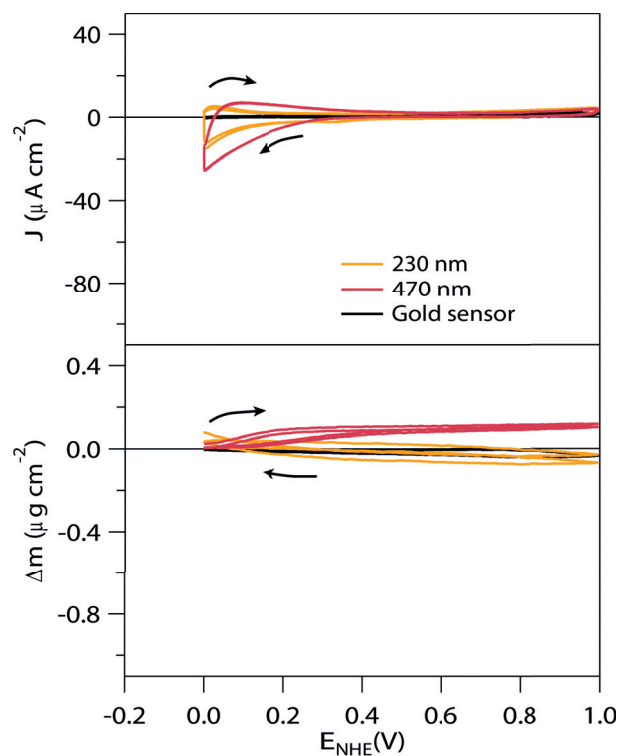


**Figure 7.16** – EQCM data of gold (black) and BBL spray coated photoanode of 230 nm (yellow) and 470 nm (red) thickness in  $\text{NaClO}_4$  0.1 M electrolyte in acetonitrile. Top graph shows the CV results, bottom graph shows the mass change calculated by the Sauerbrey equation.

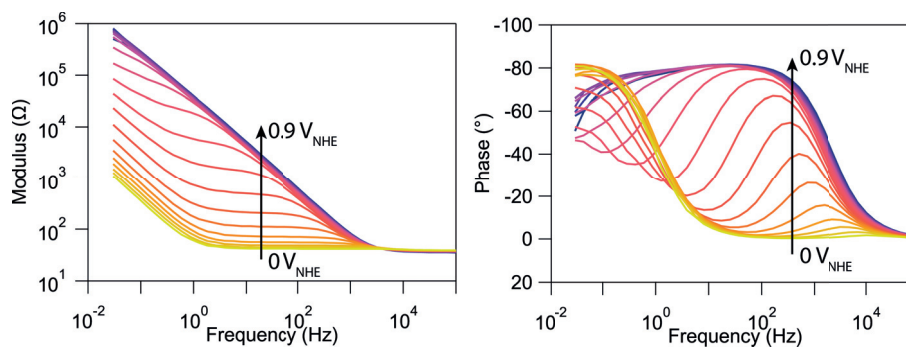


**Figure 7.17** – Bode plot of EIS data of a spray coated BBL photoanode of 230 nm in  $\text{NaClO}_4$  1 M pH 7.4

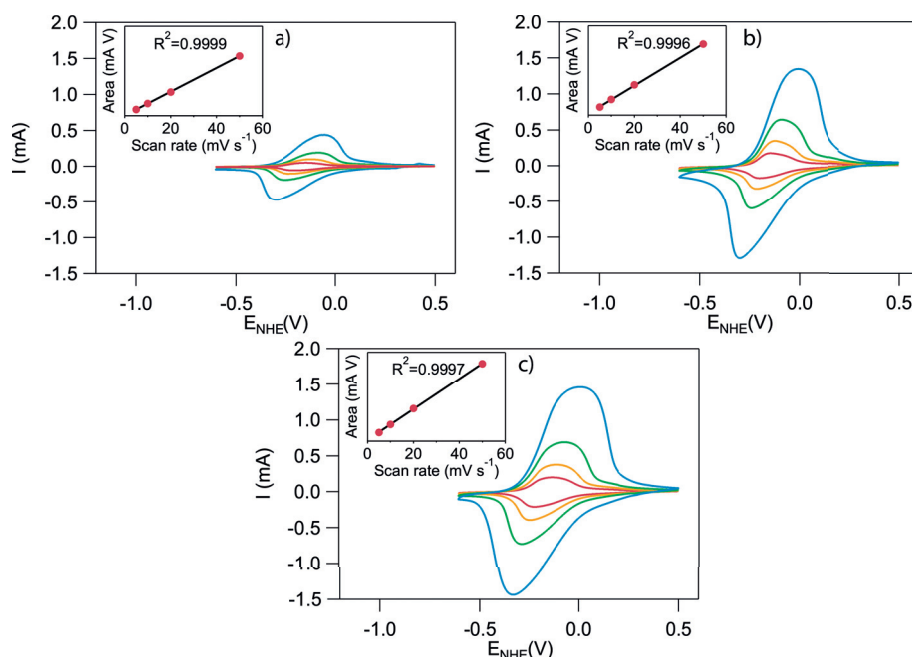


**Figure 7.18** – CV of a) 110 nm, b) 230 nm and c) 470 nm spray coated BBL photoanodes in 0.5 M NaSO<sub>4</sub> + 0.09 M KH<sub>2</sub>PO<sub>4</sub> + 0.01 M K<sub>2</sub>HPO<sub>4</sub> pH 6. Scan rate of 5 mV · s<sup>-1</sup> (yellow), 10 mV · s<sup>-1</sup> (red), 20 mV · s<sup>-1</sup> (green) and 50 mV · s<sup>-1</sup> (blue).

Thickness	Linear regression	R <sup>2</sup>	SI*
110 nm	y=0.0027x + 0.0003	0.9999	2.8 × 10 <sup>-8</sup> mol
230 nm	y=0.0078x + 0.0092	0.9996	8.0 × 10 <sup>-8</sup> mol
470 nm	y=0.0103x + 0.0087	0.9998	1.0 × 10 <sup>-7</sup> mol

**Table G.1** – Results of the linear regression for the determination of S/d ratio

## References

- [1] György Inzelt. *Conducting Polymers A New Era in Electrochemistry*. Springer-Verlag Berlin Heidelberg, 2012. ISBN: 978-3-642-27621-7. DOI: 10.1007/978-3-642-27621-7.
- [2] Suhao Wang, Hengda Sun, Ujwala Ail, Mikhail Vagin, Per O. Å. Persson, Jens W. Andreasen, Walter Thiel, Magnus Berggren, Xavier Crispin, Daniele Fazzi, and Simone Fabiano. “Thermoelectric Properties of Solution-Processed n-Doped Ladder-Type Conducting Polymers”. *Advanced Materials* 28 (2016), pp. 10764–10771. DOI: 10.1002/adma.201603731.
- [3] K. Wilbourn and Royce W. Murray. “The D.C. Redox Versus Electronic Conductivity of the Ladder Polymer Poly(benzimidazobenzophenanthroline)”. *The Journal of Physical Chemistry* 92 (1988), pp. 3642–3648. DOI: 10.1021/j100323a062.

- 
- [4] Sung Y. Hong, Miklos Kertesz, Yong S. Lee, and Oh Kil Kim. "Geometrical and Electronic Structures of a Benzimidazobenzophenanthroline-Type Ladder Polymer (BBL)". *Macromolecules* 25 (1992), pp. 5424–5429. DOI: 10.1021/ma00046a046.
- [5] K. Wilbourn and Royce W. Murray. "The Electrochemical Doping Reactions of the Conducting Ladder Polymer Benzimidazobenzophenanthroline (BBL)". *Macromolecules* 21 (1988), pp. 89–96. DOI: 10.1021/ma00179a019.
- [6] Teketel Yohannes, H. Neugebauer, S. A. Jenekhe, and N. S. Sariciftci. "Multiple Reduction States with Different Conductivities of Polybenzimidazobenzophenanthroline (BBL) Studied with Infrared Spectroelectrochemistry". *Synthetic Metals* 116 (2001), pp. 241–245. DOI: 10.1016/S0379-6779(00)00460-4.
- [7] Ursula Rammelt, Sven Bischoff, Mohamed El-Dessouki, Renate Schulze, Waldfried Plieth, and Lothar Dunsch. "Semiconducting Properties of Polypyrrole Films in Aqueous Solution". *Journal of Solid State Electrochemistry* 3 (1999), pp. 406–411. DOI: 10.1007/s100080050174.
- [8] W. Plieth, A. Bund, U. Rammelt, S. Neudeck, and LeMinh Duc. "The Role of Ion and Solvent Transport during the Redox Process of Conducting Polymers". *Electrochimica Acta* 51 (2006), pp. 2366–2372. DOI: 10.1016/j.electacta.2005.03.087.
- [9] Emese Kriván, Csaba Visy, and Jouko Kankare. "Key Role of the Desolvation in the Achievement of the Quasi-metallic State of Electronically Conducting Polymers". *Electrochimica Acta* 50 (2005), pp. 1247–1254. DOI: 10.1016/j.electacta.2004.07.050.
- [10] Hari Singh Nalwa. "Optical and X-ray Photoelectron Spectroscopic Studies of Electrically Conducting Benzimidazobenzophenanthroline Type Ladder Polymers". *Polymer* 32 (1991), pp. 802–807. DOI: 10.1016/0032-3861(91)90503-B.
- [11] B. W. Johnson, D. C. Read, P. Christensen, A. Hamnett, and R. D. Armstrong. "Impedance Characteristics of Conducting Polythiophene Films". *Journal of Electroanalytical Chemistry* 364 (1994), pp. 103–109. DOI: 10.1016/0022-0728(93)02923-6.
- [12] M. D. Levi, Y. Gofer, D. Aurbach, and A. Berlin. "EIS Evidence for Charge Trapping in N-doped Poly-3-(3,4,5-trifluorophenyl) Thiophene". *Electrochimica Acta* 49 (2004), pp. 433–444. DOI: 10.1016/j.electacta.2003.08.027.
- [13] Allen J. Bard and Larry R. Faulkner. *Electrochemical Methods: Fundamentals and Applications, 2nd Edition*. Wiley, 2001. URL: <http://eu.wiley.com/WileyCDA/WileyTitle/productCd-0471043729.html>.
- [14] Benjamin Klahr, Sixto Gimenez, Francisco Fabregat-Santiago, Thomas Hamann, and Juan Bisquert. "Water Oxidation at Hematite Photoelectrodes: The Role of Surface States". *Journal of the American Chemical Society* 134 (2012), pp. 4294–4302. DOI: 10.1021/ja210755h.
- [15] G. Tullii, A. Desii, C. Bossio, S. Bellani, M. Colombo, N. Martino, M. R. Antognazza, and G. Lanzani. "Bimodal Functioning of a Mesoporous, Light Sensitive Polymer/electrolyte Interface". *Organic Electronics* 46 (2017), pp. 88–98. DOI: 10.1016/j.orgel.2017.04.007.





## Conclusions **Part IV**



## 8 Final Comment and Outlook

Facing world energy problem is our generation challenge. Not only because of ending of fossil fuel reserves but also for economical, political and environmental reasons. Finding a technology that could provide sufficient energy for the entire world population would enhance the life quality of millions of people. For that the solar-to-fuel was demonstrated to be the potentially revolutionary technology, specially the solar hydrogen production. If this technology can be designed, solar hydrogen is envisioned to be a central element in an interconnected chemical network. In this original work, the feasibility of Photoelectrochemical (PEC) water splitting devices was demonstrated as well as presentation of a new promising material.

We started to demonstrate that an all oxide tandem solar cell is a viable target for an inexpensive device made of earth-abundant materials, namely  $\text{Cu}_2\text{O}$  and  $\text{BiVO}_4$ . Indeed their easy and scalable processing, like electrodeposition for  $\text{Cu}_2\text{O}$  or spray pyrolysis for  $\text{BiVO}_4$ , offer promising device price close to the targeted hydrogen production price of  $10 \text{ US\$ kg}^{-1}$  to compete with the Photovoltaic (PV)-electrolyzer configuration. These two materials were found to have matching optical and energetics properties, with their majority carrier energy well positioned for the Hydrogen Evolution Reaction (HER) and Oxygen Evolution Reaction (OER), and are thus suitable for a D4 wired configuration. Based on absorption properties of the two materials, this device should, in theory, be able to drive these two photo reactions with a 7.8 % Solar-to-Hydrogen (STH) efficiency. However, an efficiency of less than 0.5 % STH was obtained and explained by optical, Incident Photon-to-current Efficiency (IPCE), operational and stability losses.

Even state-of-the-art photoelectrodes are hence not yet optimized for full-device applications. The race toward the best performing photoelectrodes might consequently not be the right objective. This technology is then still far from a commercial application, even the best device configuration is still under questions as seen by the number of propositions.

One solution to resolve the inadequation of the two electrodes would be to use a material whose properties could be adapted to the second photoelectrode. In this work we proposed to use an organic material to benefit from their tunability and low prices. These were usually demonstrated for water splitting in a buried junction, i.e. protected from the electrolyte, as they suffer from poor stability. They are indeed easier to reduce or oxidize in PEC operation.

However we demonstrated that by the choice of an appropriate organic material that a photocurrent in a direct Semiconductor-liquid Junction (SCLJ) configuration can be extracted. We choose the Poly(benzimidazobenzophenanthroline) (BBL) polymer for its exceptional stability in water environment, high electron mobility and adequate band positions.

We overcome its poor solubility, which makes its thin film processing difficult, by using two different solution-based techniques which are low energy demanding, safe and easy to scale up. In particular the spray coating technique shows easier manipulation as well as producing better morphology for PEC operations. This technique shows the formation of rough and porous films which enhance the charge harvesting. These films were found to be stable, without photo-degradation, in PEC conditions and to produce  $\bullet\text{OH}$ . This was the first time that an organic material demonstrate a stable photocurrent for water photooxidation with a direct contact with the electrolyte.

A first Electrochemical Impedance Spectroscopy (EIS) analysis showed that the position of the charge extraction process, attributed first to a space-charge formation, was independent of electrolyte pH. We related the increase of photocurrent with increase of pH to this effect. Further characterization with Electrochemical Quartz Crystal Microbalance (EQCM) technique demonstrated that instead of a space charge formation at the SCLJ, this process corresponds rather to a charge building in the Helmholtz layer in response to the applied potential. We make the hypothesis that this process influence the charge transport process in the BBL film to change between a charge delocalization transport and a charge hopping transport. Therefore, the performance of the BBL photoanode can be optimized with the choice of electrolyte.

Finally the proof of concept was demonstrated with oxygen production using appropriate overlayer.

Despite the successful demonstration and the investigation of several aspects of processes governing the charge transport through this photoanode material, several challenges remain. Mainly, improvement of the overall efficiency would be necessary. Two main possibilities to enhance the performance can be suggested.

First to enhance the exciton splitting, hence to reduce the recombination rate, the formation

---

of a p-n junction appears to be the next necessary step. This can be realized with the formation of a layered, or a bulk heterojunction, film of BBL coupled with a p-type material. For that another stable material with appropriate energy band position is needed. A new polymeric molecule could also be designed containing a BBL backbone and a p-type pendant group. In both cases, the combination of a p-type material with BBL would form an electrical field at their interface which would separate excitons generated by light absorption.

The second possibility would be to favor the catalytic activity for the OER. Even if we demonstrated that a Nickel-Cobalt catalyst can be used to enhance the production of oxygen, a first overlayer of  $\text{TiO}_2$  was necessary to prepare the film surface. We tried during this work to directly attach multiple catalysts on the BBL film without any success. We believe that the polymer surface chemistry prevents the attachment of the catalyst resulting in a poor semiconductor/catalyst interface limiting the charge transfer. The next step would hence be to study this BBL-catalyst interface. We think that the direct functionalization of the film followed by a molecular catalyst attachment would help to gain understanding. In this configuration, a direct covalent bond would ensure the good catalyst attachment, and charge transport could be understood.

Finally we note that the production of oxygen in a PEC water splitting cell is not the key objective. This step is known to be the limiting one as a total of four electrons is needed for this reaction rather than two for the reduction site. However, hydrogen, evolving at the photocathode, is the desired chemical compound. To couple this photocathode, for hydrogen production, with a photoanode where an easier reaction is happening, through a one electron transfer for example, would also be a possibility. For instance, the production of hydroxyl radicals, detected in our case, can be used for the degradation of chemical compound. This would associate fuel production and waste treatment in a single cell.

I don't believe that a full organic device could achieve the performances necessary to be developed as the commercial application due to the multiple conditions to fulfill. However I do think that a device combining a metal oxide and an organic material can reach our "10:10:10" target. This project paves the way for more detailed investigations of the influencing factors and ultimately to higher performances with organic materials PEC cells.



# Acronyms

BBL	Poly(benzimidazobenzophenanthroline)
CA	Chronoamperometry
CPE	Constant Phase Element
CV	Cyclic Voltammetry
DSC	Differential Scanning Calorimetry
EIS	Electrochemical Impedance Spectroscopy
EQCM	Electrochemical Quartz Crystal Microbalance
FTO	Fluorine-doped Tin Oxide
HER	Hydrogen Evolution Reaction
HOMO	Highest Occupied Molecular Orbital
IPCE	Incident Photon-to-current Efficiency
J-V	Current density-Voltage
LSV	Linear Sweep Voltammetry
LUMO	Lowest Unoccupied Molecular Orbital
M-S	Mott-Schottky
MALDI-TOF MS	Matrix-assisted Laser Desorption/Ionization Time-of-flight Mass Spectrometer
MSA	Methanesulfonic Acid
NHE	Normal Hydrogen Electrode
OER	Oxygen Evolution Reaction
OPV	Organic Photovoltaic

## Acronyms

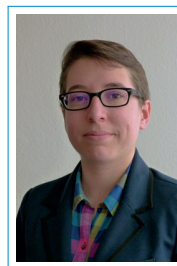
---

PDI	Perylene Diimides
PEC	Photoelectrochemical
PPA	Polyphosphoric Acid
PV	Photovoltaic
QCM	Quartz Crystal Microbalance
RHE	Reversible Hydrogen Electrode
SCLJ	Semiconductor-liquid Junction
SEM	Scanning Electron Microscopy
SFOE	Swiss Federal Office of Energy
SHE	Standard Hydrogen Electrode
STH	Solar-to-Hydrogen
TEM	Transmission Electron Microscopy
TGA	Thermogravimetric analysis
UV	Ultraviolet
UV-vis	Ultraviolet-visible Light



# Pauline BORNOZ

Avenue de la Gare 10  
1022 Chavannes-près-Renens  
☎ +41 (0)79 484 48 87  
pauline.bornoz@gmail.com  
Date de naissance: 14.07.1987  
Nationalité: Suisse



## Education

École polytechnique fédérale de Lausanne (EPFL)

<b>Doctoral Studies in Chemistry and Chemical Engineering Programme</b> <i>Group of Molecular Engineering of Optoelectronic Nanomaterials (LIMNO)</i>	<b>2013–2017</b>
<b>Master of Science MSc in Chemical Engineering and Biotechnology</b> <i>Master's project at université Pierre et Marie Curie (UPMC), Paris, France</i> <i>Group of physicochimie des électrolytes et nanosystèmes interfaciaux (PHENIX)</i>	<b>2010–2012</b>
<b>Bachelor of Science BSc in Chemistry and Chemical Engineering</b>	<b>2007–2010</b>

## Professional Experience and Projects

### Doctoral thesis.....

<b>Doctoral thesis supervised by Prof K. Sivula (LIMNO)</b> <i>Demonstration of a Photoanode for Direct Light-Driven Water Oxidation</i> – Preparation of photoelectrodes for solar hydrogen generation ; – electrochemical analysis. Key skills : autonomy, reactivity.	<b>08.2013–07.2017</b> <i>EPFL, Lausanne</i>
--	---

### Master's thesis, internship and project.....

<b>Research Internship supervised by Prof K. Sivula (LIMNO)</b> <i>Development of a Tandem Cell for Solar Water Splitting</i> – Design of experiments ; – electrochemical analysis. Key skills : autonomy, methodology.	<b>04.2013–08.2013</b> <i>EPFL, Lausanne</i>
<b>Internship supervised by Prof Ch. Comninellis</b> <i>Preparation and translation of lessons</i> – Preparation of electrochemical engineering lesson ; – translation of the Chemical Technology and Biology of Environment lesson. Key skills : pedagogy, communication.	<b>08.2012–03.2013</b> <i>EPFL, Lausanne</i>
<b>Master's thesis supervised by Mc. E. Mahé</b> <i>Characterization and Properties of Electrogenerated Hydroxyl Radicals</i> – Design of a new analytical technique for the detection and quantification of hydroxyl radicals ; – electrochemiluminescence analysis. Key skills : effectiveness, methodology.	<b>02.2012–08.2012</b> <i>UPMC, Paris</i>
<b>Master's internship supervised by M. Wohlers et C. Stadelmann</b> <i>Development and Optimization of waste treatment processes</i> – Study of centrifugation, filtration and combustion processes ; – results analysis, preparation of internal reports and procedures. Key skills : communication, flexibility.	<b>07.2011–01.2012</b> <i>Cridec SA, Éclépens</i>
<b>Master's project supervised by Prof P. Zaza</b> <i>Process Development of a Styrene Production Plant</i>	<b>02.2011–07.2011</b> <i>EPFL, Lausanne</i>

- Project study with Aspen plus software ;
  - design and optimization of a styrene production plant, economic and safety analysis.
- Key skills : decision-making and group work skills.

## Miscellaneous

---

### Teaching Assistant

**10.2012–07.2017**

*Teaching for bachelor and master's students*

*EPFL, Lausanne*

- Teaching ;
- correction of written exams and oral examination observer ;
- exercises support and supervision, laboratory work and projects.

Key skills : pedagogy, critical thinking.

### Warehouse

**09.2010–07.2011 (1d/week), 2005–2010 (Summers)**

*Order preparation, warehouse*

*Galexis SA, Écublens*

Key skills : efficiency, meticulousness.

## Language skills

---

French :	Written and oral	Mother tongue
English :	Written and oral	B2, fluent
German :	Written and oral	A2, notions

## Computer skills

---

Environnements :	PC, Mac :	ease
Standard software :	MS-Office :	mastery
Scientific software	Igor Pro, Matlab, ChemDraw, Aspen plus, LabView, solidwork :	good knowledge

## Certificats

---

### Assistantship price

**10.2016**

*Award for exceptional value in teaching*

*EPFL, Lausanne*

### Teaching Toolkit Workshop

**09.2014**

*Development of teaching skills*

*EPFL, Lausanne*

A one-day Workshop

### Aspen Plus : Process Modeling Training

**07.2013**

*Learning of the basic use of Aspen Plus software*

*AspenTech Ltd, United Kingdom*

One-week training

## Publications

---

P. Borno, M.S. Prévot, X. Yu, N. Guijarro, and K. Sivula. Direct Light-Driven Water Oxidation by a Ladder-Type Conjugated Polymer Photoanode. *Journal of the American Chemical Society*, 137(49) :15338–15341, 2015.

P. Borno, F.F. Abdi, S. D. Tilley, B. Dam, R. van de Krol, M. Grätzel, and K. Sivula. A Bismuth Vanadate-Cuprous Oxide Tandem Cell for Overall Solar Water Splitting. *The Journal of Physical Chemistry C*, 118 :16959–16966, 2014.

É. Mahé, P. Borno, E. Briot, J. Chevalet, Ch. Comninellis, and D. Devilliers. A Selective Chemiluminescence Detection Method for Reactive Oxygen Species Involved in Oxygen Reduction Reaction on Electrocatalytic Materials. *Electrochimica Acta*, 102 :259–273, 2013.

